Satellite Trails in H.E.S.S. Data

Master's Thesis in Physics

Presented by
Thomas Lang

7th September 2023

Erlangen Centre for Astroparticle Physics
Friedrich-Alexander-University Erlangen–Nuremberg

Supervisor: **Dr. Alison M.W. Mitchell**
Co-Supervisor: **Prof. Dr. Stefan Funk**

Contents

Chapter 1

Introduction

1.1 Development of Satellite Technology and the Emergence of Satellite Constellations

Satellite technology has come a long way since Sputnik I, the first artificial satellite in Earth's orbit launched by the Soviet Union on the 4th of October, 1957. The United States of America shortly thereafter followed with their Explorer 1 satellite on 1st of February 1958, starting the Space Race between the two nations during the height of the Cold War. Since then the utilization of satellites has radically changed numerous aspects of modern life. Our understanding of global weather has been revolutionized by the use of weather satellites, with TIROS (Television Infrared Observation Satellite): being the first successful one launched in 1960, providing the first weather images from space. In 1962 Telstar 1 enabled transatlantic transmission of television and telephone signals, marking the beginning of high speed global communication. Later in the 1960s satellites were developed to be placed at a geostationary orbit to provide continuous coverage over specific region. That orbit is at an altitude of 35786 km above the equator to match its orbital period to Earth's rotational period. Those orbits are ideal for communications and weather satellites, allowing live transmission of data. Modern navigation systems have been completely revolutionized by the Global Positioning System (GPS) satellites, the first of block of satellites being launched in the 1980s, enabling precise localization worldwide.

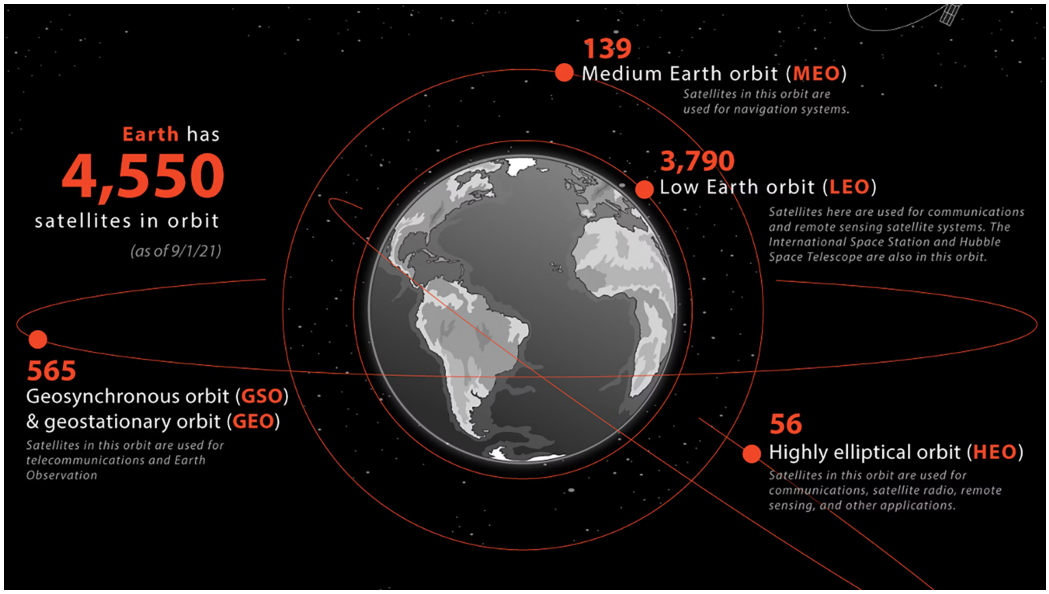

Figure 1.1: Distribution of satellites in orbit in January 2022, Figure from [1]

The scientific community has greatly benefited from the use of satellites. Various observational satellites study Earth's surface, oceans, climate and atmosphere. For astronomers one of the biggest reasons to build telescopes in space is to avoid the impact the atmosphere can have on observations, which also opens up new windows of available wavelengths.
In recent years, private companies like SpaceX and OneWeb aim to revolutionize the satellite usage, particularly at Low Earth Orbit (LEO) (altitudes below 2000 km), by providing high speed, low latency internet access. With 42000 and 7000 satellites planned and over 4200 and 620 of them launched respectively there has been a significant increase in the number of satellites around Earth. These mega-constellations, along with others such as E-Space and China's Guowang constellation the total number of planned satellites has surpassed $4 \cdot 10^5$ [2],[3].

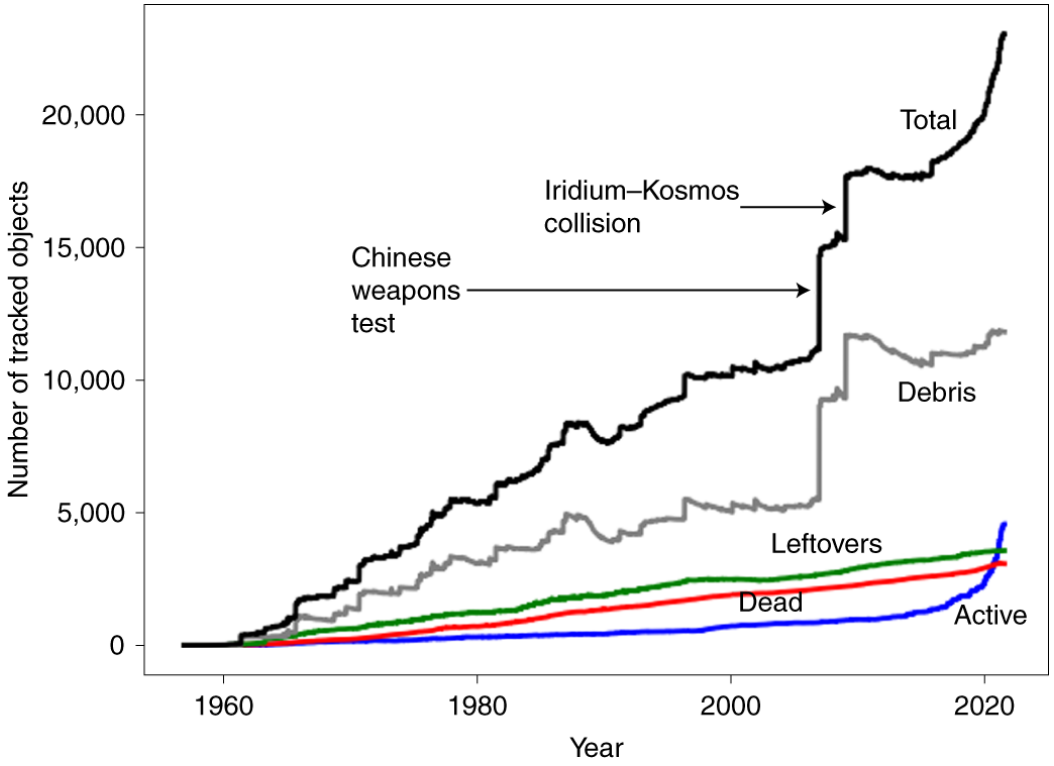

Figure 1.2: The amount of tracked arificial objects in Earth's orbit over time. With the exponential rise in active satellites such an increase can be expected for the other categories as well, Figure from [4]

These numbers have already raised several concerns about the space environment. Figure 1.2 shows the growth of satellites and other tracked objects, as well as the two events leading to a large increase of space debris [4]. In 2007 China conducted an anti-satellite missile test, in which a weather satellite was the target, which left around 3000 trackable and an estimated 150000 untrackable debris particles. In order for objects to be trackable they typically need to have a diameter of at least 5-10 cm. Accidental collisions of satellites can occur too, as the 2009 Iridium-Cosmos collision has shown. Here more than 2000 trackable debris particles were created. Considering that the number of active satellites has almost tripled in the last three years [2] another collision has become increasingly likely, let alone a collision with debris. Satellites and space stations like the ISS therefore need to perform evasive maneuvers more and more often to avoid collisions [5]. This could lead to a domino effect of destroyed satellites called Kessler Syndrome, rendering the LEO unusable for humanity.
Furthermore and more important in the context of this work the satellites can disturb ground-based astronomical observations. The International Astronomical Union (IAU) has already established the commission B7: "Protection of Existing and Potential Observatory Sites", which tries to reduce non-natural light sources on observation sites by working with officials on national and international scale.

1.2 Starlink

Since at the time of writing Starlink is the largest deployed megaconstellation [3] a brief discussion of the technical details of the satellites seems appropriate. Starlink is the satellite constellation operated by SpaceX, which aims to provide high speed internet access. Its satellites orbit Earth in a LEO at around 550 km. This low height means each satellite covers a relatively small surface area when compared to higher orbits such as GEOs, which in turn drastically raises the number of necessary satellites to offer a continuous internet connection. A geostationary orbit would not be ideal though for most modern applications such as video calls or online gaming, since they rely on low latency. Starlink claims to provide a latency of around 25 ms as compared to the $\sim$ 600 ms of a GEO satellite [6].
The first two prototype satellites called *Tintin A* and *B* were launched on the 22nd of February 2018 in a Falcon 9 rocket alongside the *Paz* satellite [7]. The test launch of 60 satellites of version v0.9 was conducted on 24th May 2019. They are powered by solar arrays and Hall-effect thrusters for orbital adjustments. All the test satellites have successfully deorbited already. Starting with the first operational satellites launched on 11th November 2019 inter-satellite communication was introduced and the Ka frequency band was added to the previously used Ku band [8]. Figure 1.3 shows the two configurations called "Shark Fin" and "Open Book". To minimize their brightness during orbit raise towards the intended orbital height the latter configuration is used while rotating the narrow edge towards Earth, while on-station the former is employed during sunrise and sunset.

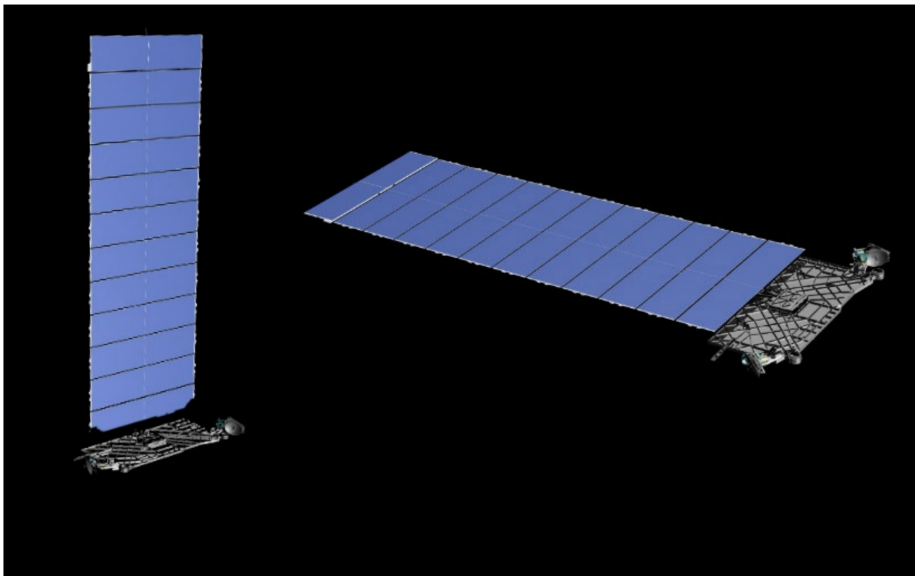

Figure 1.3: Cropped images from open book and Shark fin position, image taken from [9]

After astronomers still voiced their concerns about the satellites brightness experiments with dark coating (DarkSat) and visors (VisorSat were conducted. Ultimately SpaceX chose to implement on all v1.0 satellites from August 2020 onward as VisorSats due to thermal issues observed in DarkSat.
Those visors have been removed since the v1.5 of Starlink, first launch being the 30th of June 2021, since they would obstruct the new laser-based inter-satellite communication [10]. As a result these satellites have been observed to be brighter than VisorSat [11].
Addressing concerns of large amounts of space debris all v1.0 and onward satellites have been designed to be 100% demisable, even for early failures [12].

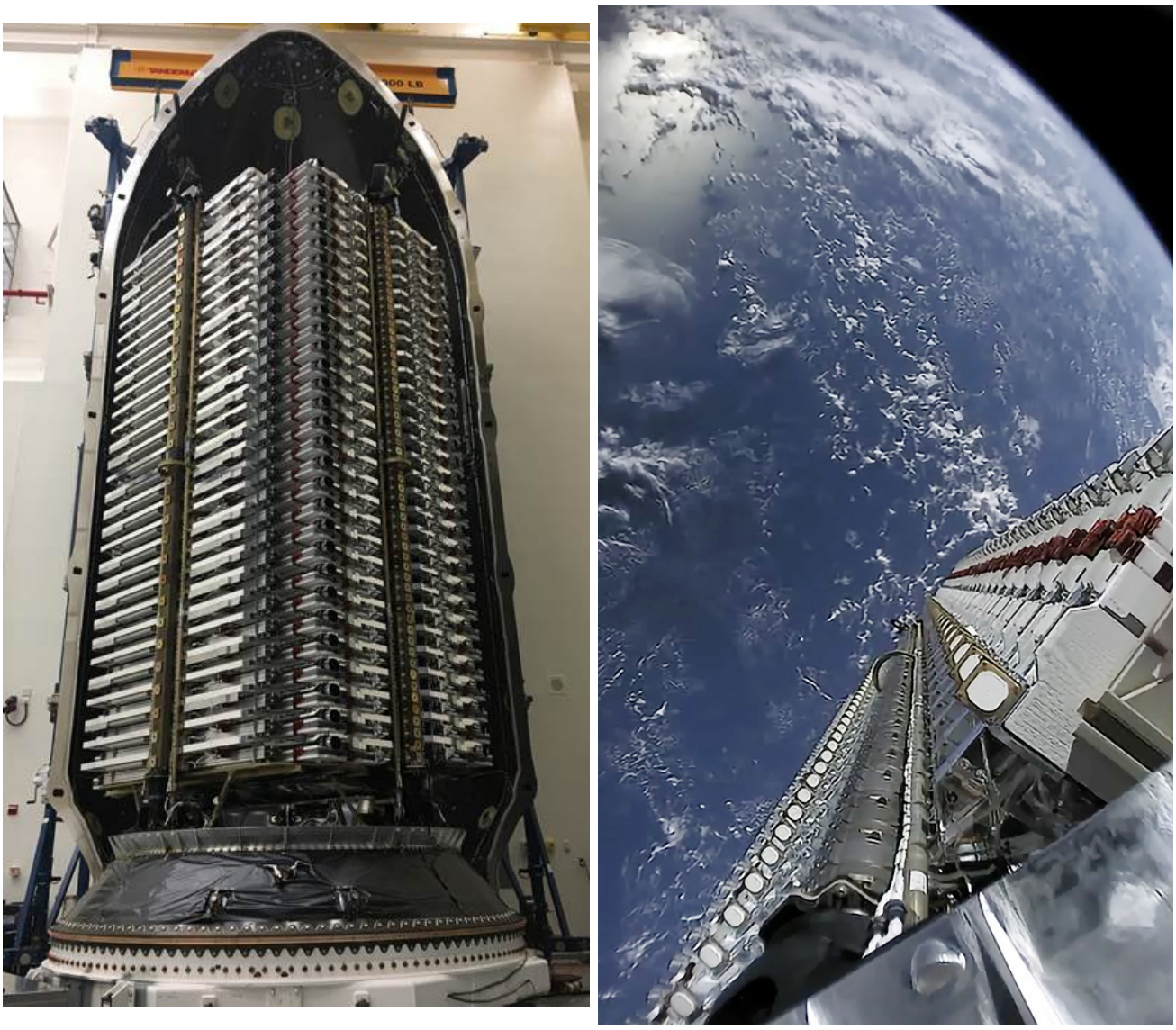

Figure 1.4: Left: Starlink satellites stacked inside a Falcon 9 Rocket on the ground, image from [13], right: Stack of 60 satellites, moments before deployment, image from [14]

Assuming an average of 50 Starlink satellites on a single Falcon 9 rocket the cost of launching a single satellites excluding development costs can be approximated to be 300000 $ [15]. At the time of writing Starlink offers internet access for costs ranging from 65 to 284 euros per month, depending on the subscription model with additional one-time cost for hardware ranging from 300 to almost 3000 euros [6].

1.3 Multi Wavelength Analysis Impacts

Numerous studies have investigated the impact of mega-constellations on ground-based astronomical observations in the radio and optical wavelength ranges. Due to their high reflectivity and relatively low distance, satellites (especially in LEO) appear as quick moving, bright dots. This is a problem for optical measurements, which often times have long integration times during a measurement, leaving trails when passing the field of view (FOV) of the telescope. Figure 1.5 shows such an image taken on the 25th of May 2019, one day after the first Starlink satellite train with 60 satellites was launched.
However, it is important to acknowledge that the density and brightness of those satellites will

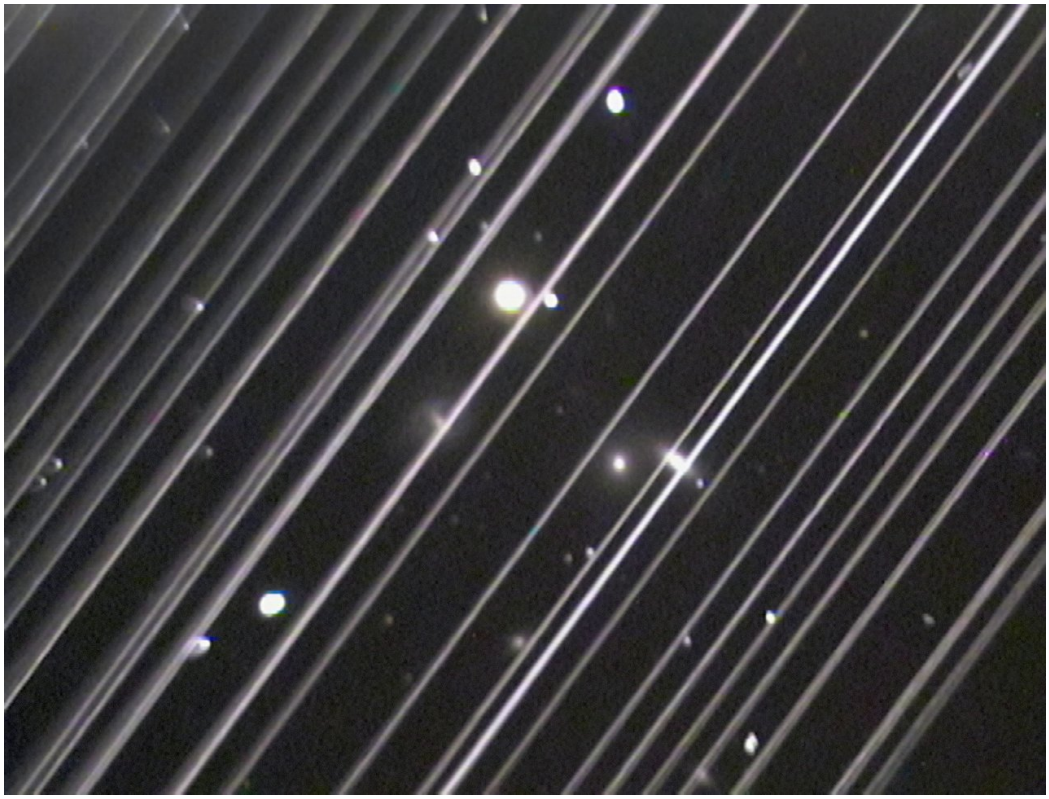

Figure 1.5: Image of the Lowell Observatory taken on 25 of May 2019, one day after the launch of the first train of 60 satellites by Starlink [16]

decrease as they ascend to their intended orbital altitude and the likelihood of these trains crossing the telescope's FOV is relatively low [17]. A recent analysis of the optical brightnesses of Starlink satellites was done by the Zwicky Transient Facility (ZTF), which also investigated Starlink satellites using visors, which were introduced after astronomers voiced their concerns with the reflectivity of the satellites [18]. It was found that the older, un-visored satellites at 550km have mean magnitudes ranging from 4.58-5.16 in the i,r and g bands, which decrease to 5.91-6.77 when visors are deployed.

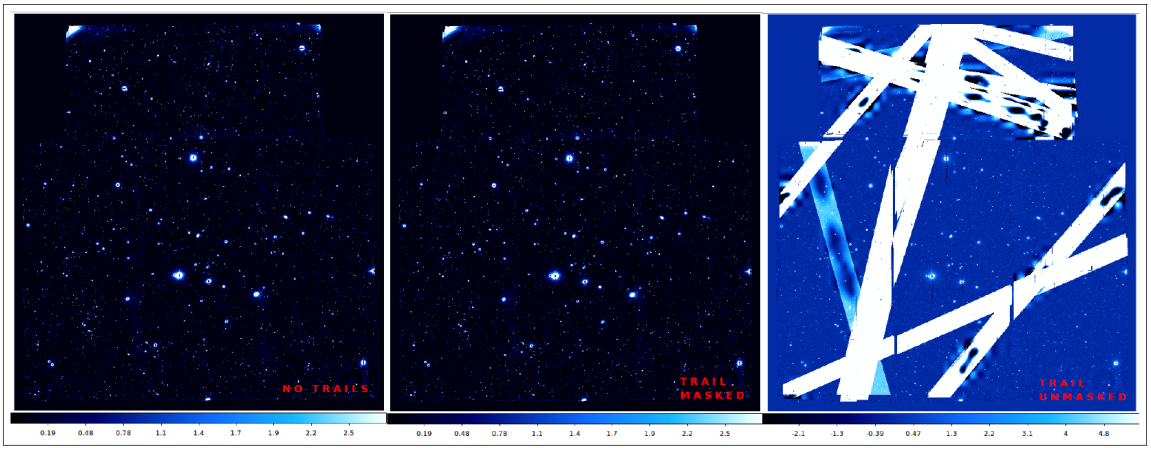

Figure 1.6: Masking of trails in the optical can mitigate the effect trails have on image taking for now, images from [19]

A straightforward way to avoid detecting satellites would be to to simply avoid taking observations in directions in which a transit of the camera's FOV is expected. In theory it should be possible to include this in the scheduling, since the positions of all satellites are obtainable for up to

weeks in the past and future around the current date. But this method becomes increasingly restrictive for an increase in field of view (FOV) of the telescope, duration of maintaining the same observational direction and an increase of the total number of satellites in orbit. In that case knowing the brightness of each satellite to decide, whether its apparent brightness is high enough to affect measurements, would be necessary. Further, so called Target of Opportunity (ToO) measurements, which are unpredictable, still have the possibility to be affected by trails. There are techniques used, that can remove trails from the images, as it is shown in Figure 1.6, (credit to Gallozzi et al. 2020 [19]), but considering the large increase of satellites launched every year, it is possible that those mitigation techniques might not be enough to fully prevent trails from appearing in the final images in the future.
Additionally, the downlink transmission of satellites can interfere with measurements taken by radio telescopes. Whereas in the optical bands trails can be removed relatively easily by masking them, the effect on radio images is much more complex and affects the entire map, which makes it challenging to identify and remove them. An analysis done by the team of the future Square Kilometer Array (SKA) based on the deployment of 6400 satellites revealed that astronomical observations of the impacted band 5b would take 70% longer [20]. The frequency range of the 5b band is 8300-15300,MHz, and it holds significance for the detection of organic molecules. Their findings also show that for constellations of up to 100000 satellites the entire band 5b could be rendered unusable, if no mitigation techniques are used. One such technique would be to avoid directing the satellite transmitters towards the dishes of SKA, a measure that can be easily implemented through a simple software modification, reducing the impact by a factor of at least 10.

1.4 Impact on Ground-Based γ-ray Astronomy

Compared to other wavelength ranges, there is limited documentation on the impact of satellites on telescopes operating in the very high energy range (>20 GeV). Notably one publication from Gallozzi et al.(2020) [19] has predicted the impact on different kind of telescopes for 50000 satellites in orbit. They find that for that number the different kind of IACT telescopes could on average expect 24 to 90 satellites crossing the FOV in a 20 minute exposure time. The current state-of-the-art methods for ground-based γ-ray astronomy in this energy range are the Imaging Atmosphere Cherenkov Telescope (IACT) method (see section 2) and the Water Cherenkov Detectors (WCDs). Since the latter type of detector is based on photons produced by the Cherenkov effect (see section 2.4) directly inside the tanks of sealed, ultra-pure water it is reasonable to assume the reflection of light off of a satellite will not affect those types of high-energy γ-ray detectors.
These instruments typically employ a signal processing integration time of approximately 10 nanoseconds [21], which is orders of magnitude smaller than the shortest viable integration time of optical or radio telescopes. The lack of significant studies on this topic may be attributed to the assumption that the effect of satellite trails is negligible. However, with the recent surge in satellite launches, this assumption is now being called into question. This thesis aims to investigate whether this assumption is and will be justified or not and to evaluate the potential impact on future observations with the next generation Cherenkov Telescope Array (CTA).

1.5 Targets of γ-ray Astronomy

A brief summary of the sources observed by γ-ray telescopes will be given here. By studying the γ-ray spectrum a better understanding of the underlying physical processes of the various astronomical objects can be obtained. Unlike the lower end of the electromagnetic spectrum

γ-rays can not be created by thermal radiation. They are the product of interactions or decays of highly energetic particles which gained their energy in large cosmic accelerators.
A prime example of one such accelerator is the shock front of a supernova travelling through the interstellar medium (ISM), called supernova remnant (SNR). Here a key mechanism to produce the energetic particles is called Fermi acceleration, in which the shock front interacts with the surrounding ISM Two types of Fermi acceleration exist: first and second order, the processes of which are not going to be discussed here, for a more detailed explanation see [22]. Less violent sources like stellar clusters can reach sufficiently strong shock fronts at the interaction region between the overlapping stellar winds with the ISM [23]. An additional mechanism can be seen in neutron stars, in particular in pulsars. Because of the strong, fast rotating magnetic fields the surrounding particles are accelerated to relativistic energies creating a so called pulsar wind, which interacts with the ISM, resulting in a pulsar wind nebula (PWN) [24].
In compact binary systems, i.e. two stars with one of them being a neutron star or black hole, the compact object can feed off the other star by forming an accretion disc, in which particles are accelerated by various means [25]. During the process the neutron star or black hole can emit relativistic particles by pulsar wind and jets respectively. Apart from a few systems, which have very large companion stars with a high mass flux, most compact binary systems do not reach energies high enough to be detected by ground based VHE γ-ray telescopes [25]. Supermassive black holes at the centre of galaxies can form accretion disks as well, and hence can produce huge relativistic jets of hot gas perpendicular to the disc. These black holes are then called active galactic nuclei (AGN) and are visible at the VHE range if the orientation of the jets aligns closely with our line of sight. In such cases the AGN is called a blazar, a term composed from the two categories BL Lac objects and flat-spectrum radio quasars (FSRQ), with the latter of the two being more luminous and exhibiting stronger spectral lines [26].
The most luminous events in the observable universe are gamma ray bursts (GRBs), which are created by supernovae or binary neutron star mergers. They are categorized into short ($<2\,$s) and long ($>2\,$s) lasting GRBs. An anti-correlation can be found between the hardness of the GRB spectrum and its duration [27], hence these transient events are extremely hard to point towards to in time. Nevertheless, iIn 2019 emission in the 0.2-1 TeV range from a GRB and the following afterglow could be detected for the first time by the MAGIC and H.E.S.S. telescopes [28].

Chapter 2

Imaging Atmosphere Cherenkov Telescopes (IACTs)

IACTs are ground based detectors designed for detecting γ-ray photons in the very-high energy range above 20 GeV. Currently there are four IACTs in operation: the Major Atmospheric Gamma Imaging Cherenkov Telescopes (MAGIC), the First G-APD Cherenkov Telescope (FACT) located on La Palma, the Very Energetic Radiation Imaging Telescope Array System (VERITAS) in Arizona and the High Energy Stereoscopic System (H.E.S.S.) located in the Khomas Highland in Namibia. IACTs detect γ-rays and Cosmic rays (CRs) indirectly by measuring the Cherenkov radiation emitted by secondary particles created in the interaction of the primary particle with the atmosphere.
The data analysed in this work has been produced by the H.E.S.S. telescope. A similar analysis is warranted for the other telescopes as well.

2.1 High Energy Stereoscopic System (H.E.S.S.)

Figure 2.1: H.E.S.S. telescope array in the Khomas Highland in Namibia, image from [29]

The High Energy Stereoscopic System is comprised of 5 IACTs. Its remote location in the low humidity Khomas Highland in Göllschau, Namibia 1800 m above sea level, makes it for now the only operating IACT on the southern hemisphere, making it an ideal observatory to study the galactic plane. It has been able to catalogue 78 VHE γ-ray sources the H.E.S.S. galactic plane survey (HGPS), the observed region is shown in Figure 2.2, 31 of those could be identified as

pulsar wind nebulae, supernova remnants (SNRs), composite SNR, or gamma-ray binaries [30]. The initial four telescopes CT1-4 of Phase I of the project officially were inaugurated in 2004 [31], and are placed on the corners of a 120 m by 120 m square. Each telescope is identical in design, with mirror diameters of 12 m, covering an area of 108 m^2. The reflected light is focused onto the camera with 960 pixels made of photomultiplier tubes (PMTs), with a pixel size of 0.16° each, combining to a total field of view of 5°. Taking into account the quantum efficiency of the PMTs, and the reflectivity of the mirrors in the Cherenkov spectrum, a lower energy threshold for the γ-rays of ∼100 GeV is achieved.
Phase II began with first light in 2012 on the fifth telescope called CT5, which was placed in the centre of of CT1-4 [32].. Being the largest IACTs to this day with a 28 m mirror diameter corresponding to an area of 614 m^2, the energy threshold was lowered to ∼30 GeV. The camera had a FOV of 3.2° and consisted of 2048 pixels covering 0.067° each [31].
H.E.S.S. like all other IACTs takes its measurements in sets of runs, with an ideal run usually taking 28 min of data. This duration is chosen to provide enough event statistics while maintaining similar measurement conditions throughout the run.

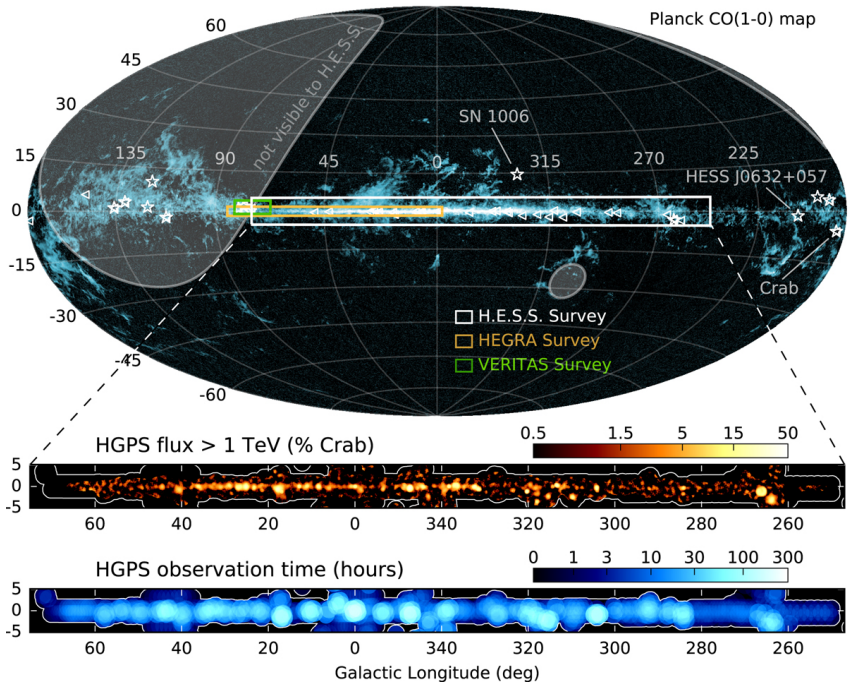

Figure 2.2: All-sky image showing the regions observable by H.E.S.S. and the region of the H.E.S.S. galactic plane survey (HGPS), which analysed 2700 h of data taken from 2004 to 2013, finding 16 new VHE sources. Lower panels show a zoom in on the region of the HGPS, image from [30].

2.1.1 Stereoscopic method

As its name suggests H.E.S.S. uses its multiple telescopes to employ the stereoscopic imaging method. Measuring the same event from different positions has several advantages over using only a single telescope. Figure 2.3 shows how by detecting the same event from different angles the intersection of the major axes (see section 2.8) can be used to reconstruct the direction of the primary particle with a higher accuracy, increasing the angular resolution to being better than 0.1° per event [33]. Also an energy resolution of 10-15% per event can be achieved by determining the weighted average of the energy estimates of each single telescope [33]. Furthermore the height of the shower maximum can be determined by creating a three dimensional shower reconstruction [33].

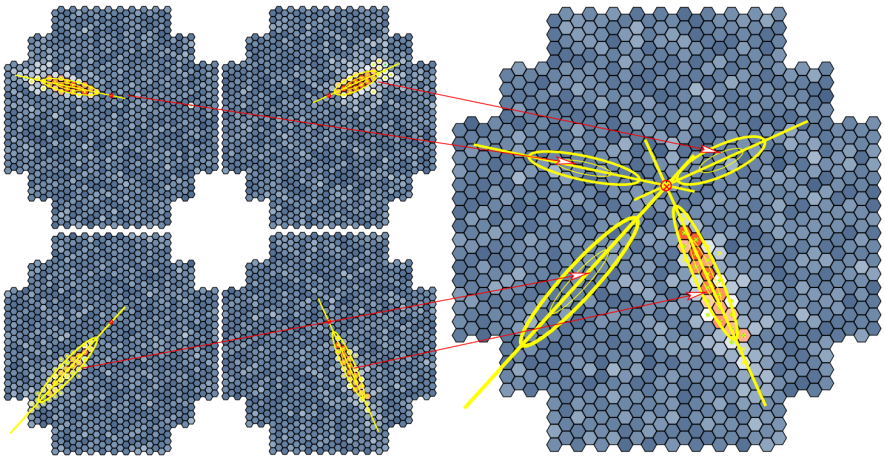

Figure 2.3: Using the stereoscopic observation technique shower images of one event are projected into a single camera plane to determine the direction of the source. Figure from [33]

Properly rejecting muon events as background is especially challenging for a single telescope for events close to the lower energy threshold, as they can resemble γ-ray events. However due to the spacing of the telescopes a muon will almost always only affect a single telescope. Therefore utilizing a stereo trigger rejects almost the entire muon background [33].

2.1.2 HESS1 Camera Upgrade (HESS1U)

Addressing age-related failures of the electronics and the high dead time of $\sim 450\,\mu s$, all components except for the PMTs and the single photoelectron calibration unit of the cameras of CT1-4 were replaced by a new camera design build around the NECTAr analog chip with a dead time of $\sim 5.5\,\mu s$ [34]. The upgrades were first tested for CT1 beginning in July of 2015 and after successful implementation were finished for all CT1-4 telescopes in September of 2016. Subsequently they are referred to as HESS IU. The use of the NECTAr chip provided a testing ground for its use in the MST and LST at CTA. Using a computer on each of the 62 devices in the camera allowed for an improved slow control of the camera, a software based security and data buffering of up to ten minutes. Two analog front-end boards amplifying and digitizing the signal of 8 PMTs were connected to a slow control board forming a modular unit called "drawer", with 60 drawers in total per camera. As a result testing various optimizations to potentially improve the telescopes sensitivity became possible.

2.1.3 FlashCam

FlashCam is the first IACT camera with a fully digital camera trigger and readout electronics, enabling a continuous signal digitization for event rates of up to 30 kHz with zero dead time [35]. It was originally designed as a camera with a FOV of 7.7° for the Medium-Sized Telescope (MST) of the Cherenkov Telescope Array (CTA) (see section 2.2), which is still in the development stage [21]. The first full-size prototype in operation was installed in a MST prototype in Berlin in 2017, in image of that prototype is seen in Figure 2.4.
It was decided to replace the camera of CT5 in 2019 with one based on the Flashcam design, fitted for the already present mirrors. CT5-FlashCam at H.E.S.S. has a FOV of 3.4°, and is made up of 1758 PMTs that individually cover a FOV of 0.08°. The PMTs are arranged in the Photon Detecor Plane (PDP) with a spacing of 50 mm to form a hexagonal shape with a total area of $3.81\,m^2$ [36]. The PDP is comprised of 147 modules, which each containing the high voltage supplys and pre-amplifiers for 12 PMTs. As a consequence six of the 1764 available channels are

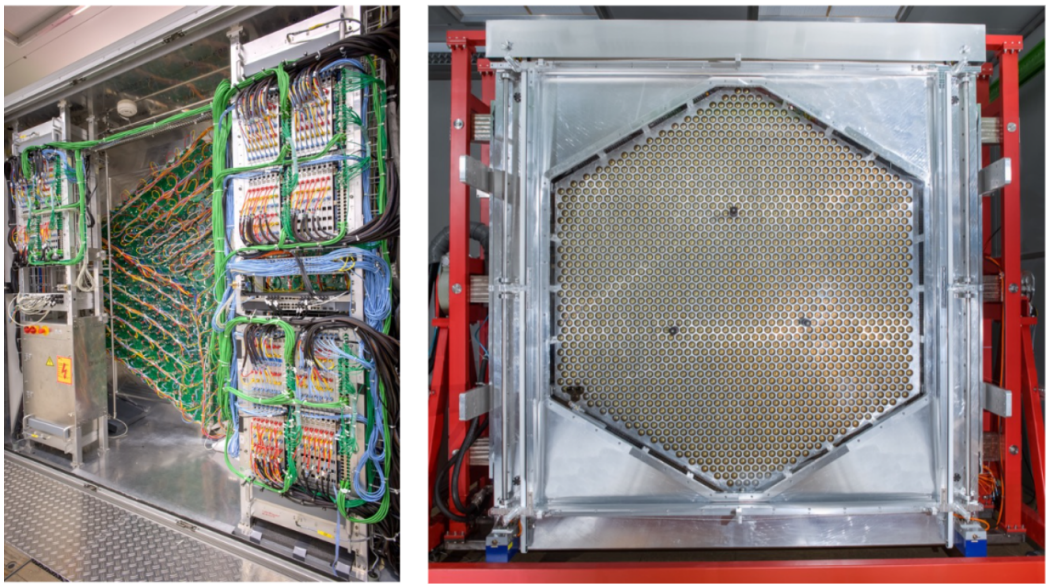

Figure 2.4: Prototype of FlashCam type camera in Berlin, image from [21]

always going to be dead.
The pre-amplifier is designed to linearly amplify up to 250 p.e., and enter a quasi-logarithmic behaviour above, extending the signal range up to $\sim$ 3000 p.e [36]. This allows the use of just a single amplifier and readout channel per pixel. The amplified PMT signals are directly transmitted to the readout electronics without any filtering of the direct current (DC) component, making FlashCam "DC-coupled".
Together with the upgraded quantum efficiencies of the new PMTs and dynamically adjustable integration times as low as 9 ns (previously fixed 16 ns) an improvement of the signal-to-noise ratio (SNR) by a factor of 1.6 is achieved.

2.2 Cherenkov Telescope Array (CTA)

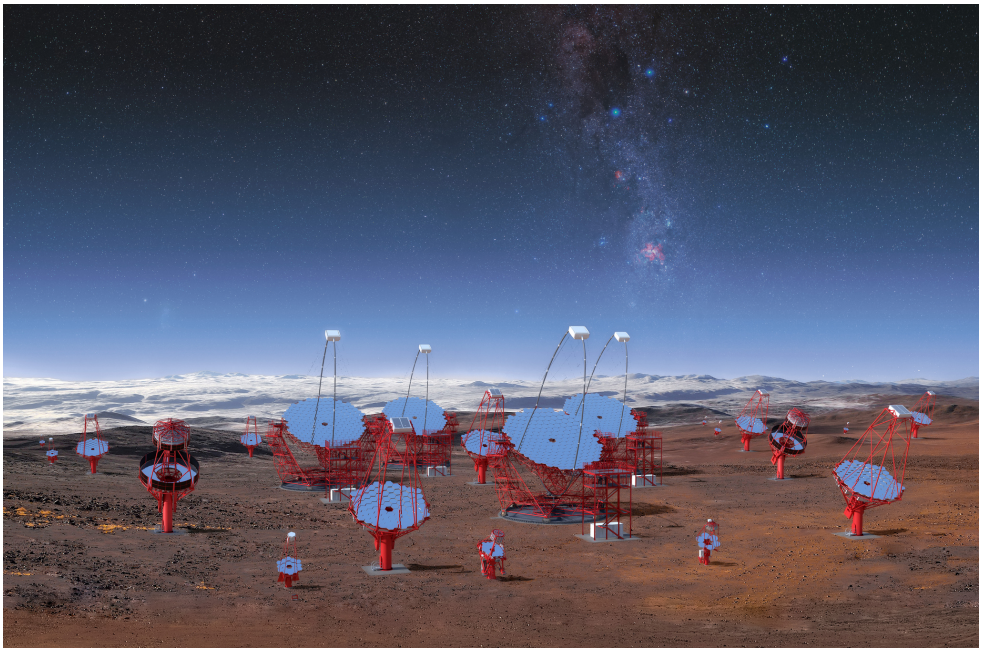

Figure 2.5: Artistic impression of the southern array of the future CTAO, Image by G.P. Diaz [37]

The next generation IACT Cherenkov Telescope Array (CTA) is made possible by a collaborative, international endeavor and is comprised of two observations sites, providing coverage of both the southern and northern skies. The northern one is located at the Roque de los Muchachos observatory in La Palma, Spain, while the southern site is in the Chilean Atacama Desert. At the highest energies the angular resolution of CTA will be close to 1 arc-minute [25], well below any other VHE detector. As Figure 2.6 shows an increase in sensitivity by an order of magnitude is expected over the measurement range of 20 GeV to 300 TeV.

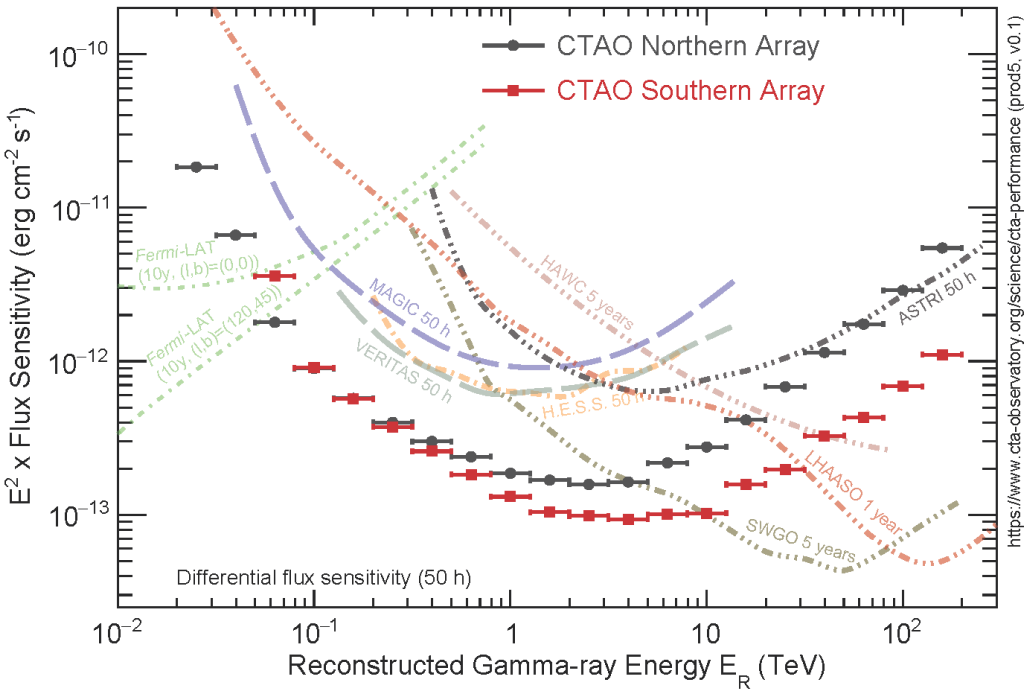

Figure 2.6: Expected sensitivity performance of CTA in the alpha configuration in comparison to other γ-ray observatories, Figure from [38]

The total number of planned telescopes on both sites combined in the current alpha configuration is 64 and they are divided up into three telescope classes, the small- medium- and large-sized telescopes (SST, MST, LST)[39]. In order to detect particles up to ∼300 TeV a large area at the south site will be covered by 37 units of the 4.3 m, mirror diameter SSTs. Its camera has a FOV of 10.5° and its 2048 pixels utilize Silicon photomultipliers (SiPMs) instead of PMTs. The MST telescope with a mirror diameter of 11.5 m has two working camera concepts, namely NectarCam (used in La Palma) and FlashCam (used in Chile), with a FOV of 7.7° and 7.5° respectively. Currently the MST is the only telescope type planned to be used at both CTA sites, with nine at La Palma and 14 in Chile. The low energy range will be covered by four 23 m diameter LSTs at the northern site, with the first one already built. However the alpha configuration allows for the addition of four LSTs at the southern site in a future array. The LST Collaboration has recently published their first scientific results based on 49 h of measurements of the LST-1 in a paper [39], [40].

Among the key science projects for the CTAO are surveys of the Galactic Plane, the LMC and the first extragalactic survey with an IACT [25]. These will be possible due to the improvements in angular resolution and sensitivity, but also the larger FOV of the individual telescopes. Furthermore CTA will be able to operate in a "divergent mode", which can only be done due to the large number of telescopes. Depending on the distance to the centre of the array a telescope will point at slightly different positions in the sky, effectively increasing the FOV of the entire observatory at the cost of some sensitivity [41].

2.3 Extensive Air Shower (EAS)

Highly energetic γ-rays and CRs interact with earth's atmosphere at an altitude of $\sim 20,\mathrm{km}$ [42], therefore they can not be detected directly on Earth's surface. In doing so they create secondary particles, which in turn can interact with other particles in the atmosphere, leading to a cascade of particles called Extensive Air Shower (EAS). These are categorised into electromagnetic and hadronic showers, the former is caused by incident leptons and photons, the latter by hadrons such as protons and other heavier nuclei.

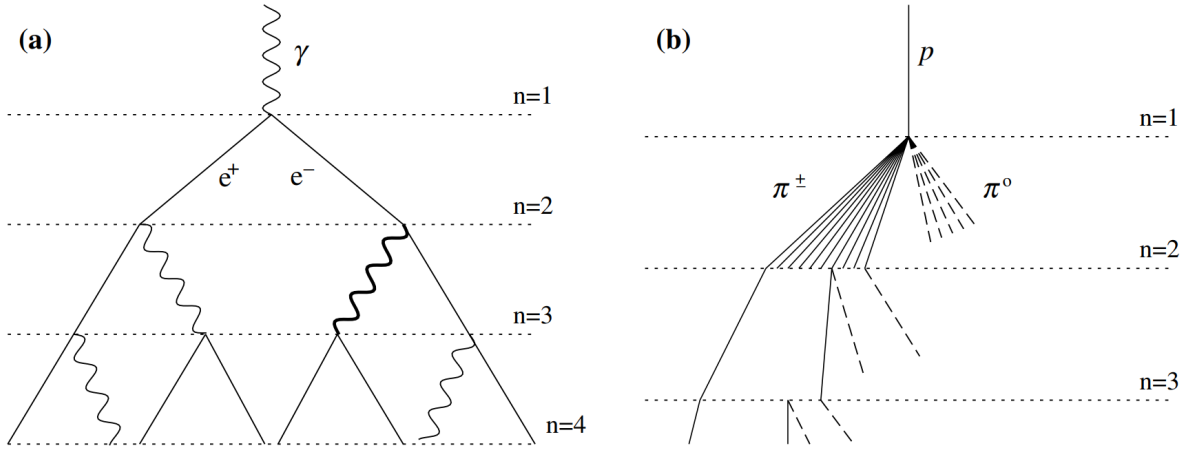

Figure 2.7: Schematic of the difference of electromagnetic (a) and hadronic (b) cascades. Neutral Pions in the hadronic shower decay mostly into two photons, creating electromagnetic sub-showers, Figure from [43]

According to the Heitler model [43] the two dominating energy loss interaction processes in electromagnetic EAS are pair-production and Bremsstrahlung. The former occurs when an incident γ-photon interacts with the Coulomb field of a nucleus to create a particle-anti-particle pair, which in most cases are an electron and a positron. The charged particles are decelerated by electric fields and emit photons via Bremsstrahlung. These two processes repeat as long as the energy of the particles permits it, leading to a cascade of particles. An illustration of the beginning of this cascade is shown in Figure 2.7 (a), each step occurring on average after one splitting length, defined as $d = \lambda_\mathrm{r} \ln 2$, with the radiation length λ_r in the medium, which in the atmosphere is $\lambda_\mathrm{r} = 36.6\,\mathrm{g\,cm^{-2}}$[44].
The shower continues until radiative losses are lower than collisional energy losses, which in air occur at particle energies of $\xi_c^e \sim 85\,\mathrm{MeV}$. At this depth X_max the shower has its maximum size N_max. By determining the number of splitting lengths n_c the maximum depth can be calculated to be $X_\mathrm{max} = n_\mathrm{c}\lambda_\mathrm{r} \ln 2 = \lambda_\mathrm{r} \ln\left(E_0/\xi_c^e\right)$. For an incident photon with $E_0 = 1\,\mathrm{TeV}$ this results in a value of $X_\mathrm{max} \approx 340\mathrm{g/cm^{-2}}$, corresponding to an altitude of $h_\mathrm{max} \approx 10\,\mathrm{km}$ above sea level.
Outnumbering γ-rays by a factor of $\sim 10^4$ [45] are Cosmic rays, which are overwhelmingly dominated by protons. Those particles interact with the atmospheric nuclei inelastically, creating hadronic EAS in which the strong force dominates, with pions as the most probable products. Due to the possibility of more than two products at each vertex these EAS are usually much more laterally spread and can also contain electromagnetic sub showers caused by the decay of π^0 mesons.

2.4 Cherenkov Radiation

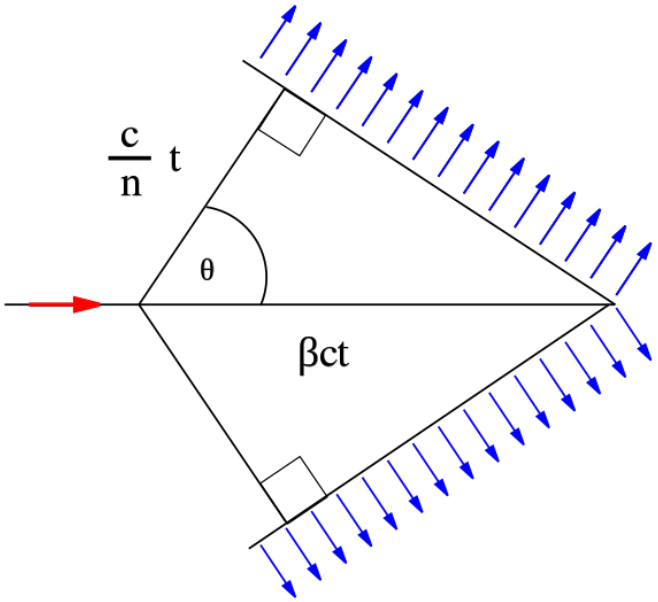

Figure 2.8: Illustration of the geometry of Cherenkov cone. Note that this is a simplification for the case that n is independent of λ, Figure from [46]

The particles created in an EAS have such a high energy that they travel at speeds close to the speed of light in vacuum c. Most importantly for IACTs their velocity can be higher than the phase speed of light in the atmosphere, that is $v > c/n$, with n being the refractive index of the atmosphere. In that case they will emit so-called Cherenkov radiation.
Since the atmosphere is a dielectic medium, charged particles travelling through it will polarize the surrounding medium, which emit electromagnetic waves when they return to their ground state. These spherical waves will have a phase velocity of c/n. If the original charged particle now has a velocity $v > c/n$ the spherical waves interfere constructively at an emission angle $\cos(\theta) = c/nv$, the emission geometry of the resulting Cherenkov cone can be seen in Figure 2.8.

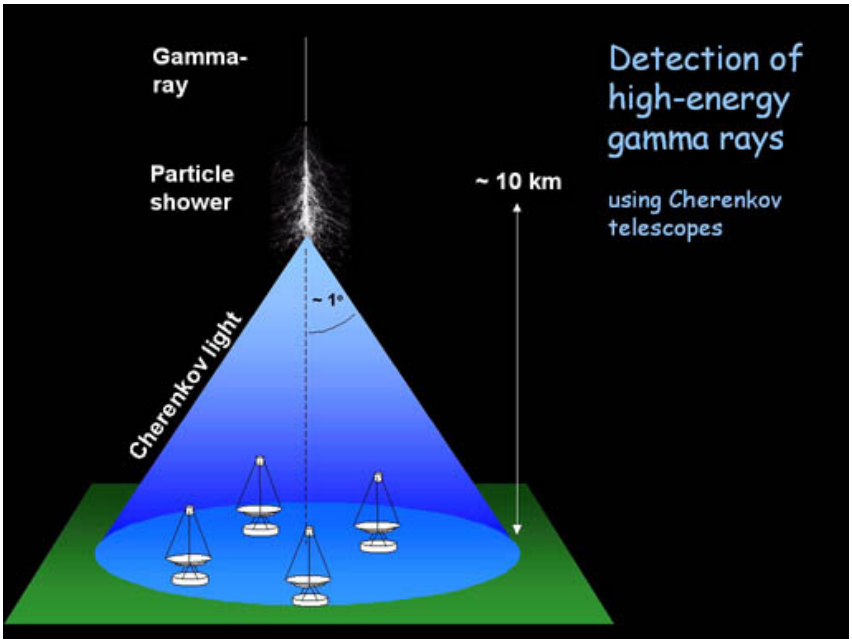

Figure 2.9: Artistic representation of the Cherenkov cone produced over H.E.S.S. I, Figure from [47]

With typical values for the atmospheric refractive index n and $\beta \approx 1$ the emission angle is around 1°. Using the previously mentioned shower maximum height the cone will have a diameter of $\approx 250 - 300\,\mathrm{m}$ at altitudes at which IACTs operate, determining their optimal spacing. The effect was described theoretically by the Nobel prize winning Frank-Tamm equation (formulated in 1937, awarded in 1958 together with Cherenkov)

$$\frac{\partial E^2}{\partial x \partial \omega} = \frac{q^2}{4\pi}\,\mu(\omega)\omega\,\left(1 - \frac{1}{\beta^2 n^2(\omega)}\right) \tag{2.1}$$

with the charge of the incident particle q the permeability of the medium $\mu(\omega)$ and using $\sin^2(\theta(\omega)) = 1 - \frac{1}{\beta^2 n^2(\omega)}$. The energy loss per unit length is then obtained by an integral over the frequency.

$$\frac{dE}{dx} = \int_{v > \frac{c}{n(\omega)}}^{\infty} \frac{q^2}{4\pi}\,\mu(\omega)\omega \sin^2(\theta(\omega))d\omega \tag{2.2}$$

Note that only frequencies are considered for which the relation $v > \frac{c}{n(\omega)}$ still holds.
The number of emitted photons per unit length in a wavelength range can then be deduced to be

$$\frac{\partial N}{\partial x} = 2\pi\alpha\,\frac{1}{\beta^2 n(\omega)^2}\left(\frac{1}{\lambda_{\min}} - \frac{1}{\lambda_{\max}}\right) \tag{2.3}$$

with α being the fine structure constant. At altitudes of around 8 km, $\beta \approx 1$ and a wavelength range of $\lambda_{\min} = 300\,\mathrm{nm}$ to $\lambda_{\max} = 600\,\mathrm{nm}$ this will equate to ~ 15 photons per meter traveled [48]. This relatively low number makes it imperative to distinguish them from the so called Night Sky Background (NSB, see section 2.5). Fortunately the spectrum of the Cherenkov radiation has its peak in the ultra-violet, letting the light appear as a bright blue for the human eye, a spectral region which is comparatively not strongly impacted by NSB, as the two spectra in Figure 2.10 show. The photo detectors of the IACTs are therefore optimized to have their highest quantum efficiency at those wavelengths.

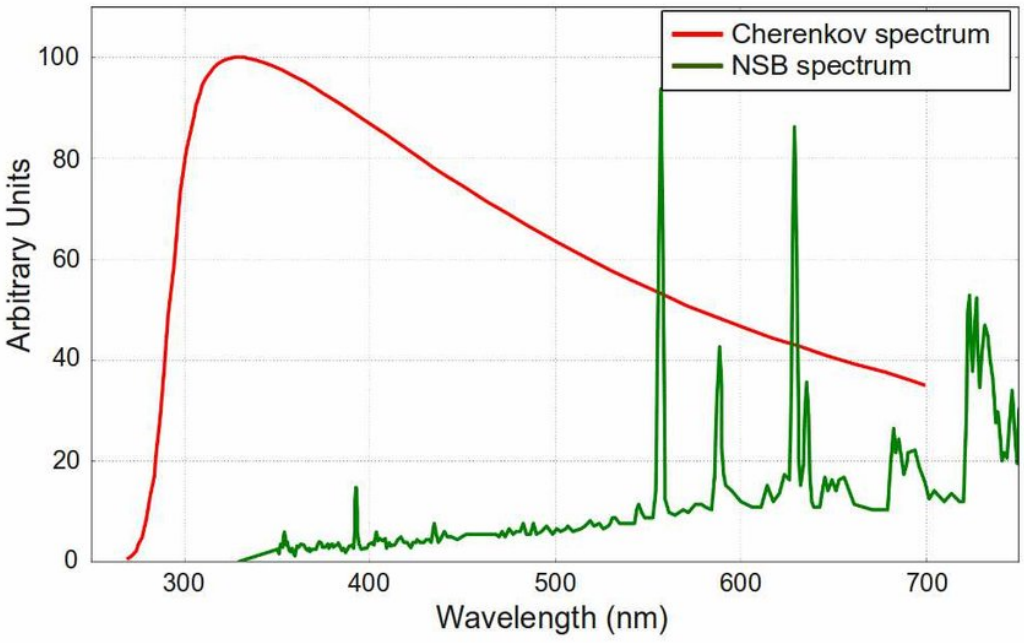

Figure 2.10: Comparison of the spectra of the Night Sky Background (NSB) at 2200 meter altitude in La Palma, Spain and Cherenkov radiation, Figure from [49]

2.5 Night Sky Background (NSB)

NSB is comprised of every light source that is not coming from the Cherenkov radiation detected by H.E.S.S. This includes starlight, moonlight, meteorites and atmospheric air glow, but also artificial sources like light pollution, aircraft and satellites [50]. Understanding the baseline brightness is crucial for attributing measured photons correctly, allowing measurements at a higher baselines.
The easiest way to obtain a typical NSB spectrum is simply to measure it directly at the observation site. This has been demonstrated for the La Palma site by Benn and Ellison (1998) [51], measuring the NSB spectrum of moonless nights visible in Figure 2.10, utilizing the on site, 4.2 m optical William Hershel Telescope (WHT). The main contributors to the measured NSB in directions between stars at the observation site in La Palma are, in decreasing brightness, the airglow, zodiacal light, starlight and light pollution. Airglow is caused by light emission of atomic and molecular interactions in the atmosphere of particles that are excited or ionized by UV light or CRs. Zodiacal light is the scattering of sunlight on interplanetary dust and is therefore mainly visible in the ecliptic plane. The starlight considered here consists of the integrated starlight of faint stars together with extragalactic sources and light scattered by interstellar dust, producing a glow in the galactic plane. The main contributor to light pollution was taken to be scattered street lamp light consisting of sodium and mercury emission lines, which increases in brightness for higher zenith angles in directions pointing towards cities.
A study comparing the NSB rates at the La Palma and the H.E.S.S. sites has shown photon fluxes near zenith for dark regions of $2.6 \cdot 10^{12}/\mathrm{sr\,s\,m^2}$ and $2.6 \cdot 10^{12}/\mathrm{sr\,s\,m^2}$, respectively [52]. No zenith dependency could be found in this analysis for the Namibian data set, as opposed to the one taken at La Palma. However an optical telescope of the caliber of the WHT is simply not available at the H.E.S.S. site, making long-term monitoring not feasible, necessitating a model of the NSB and its components.

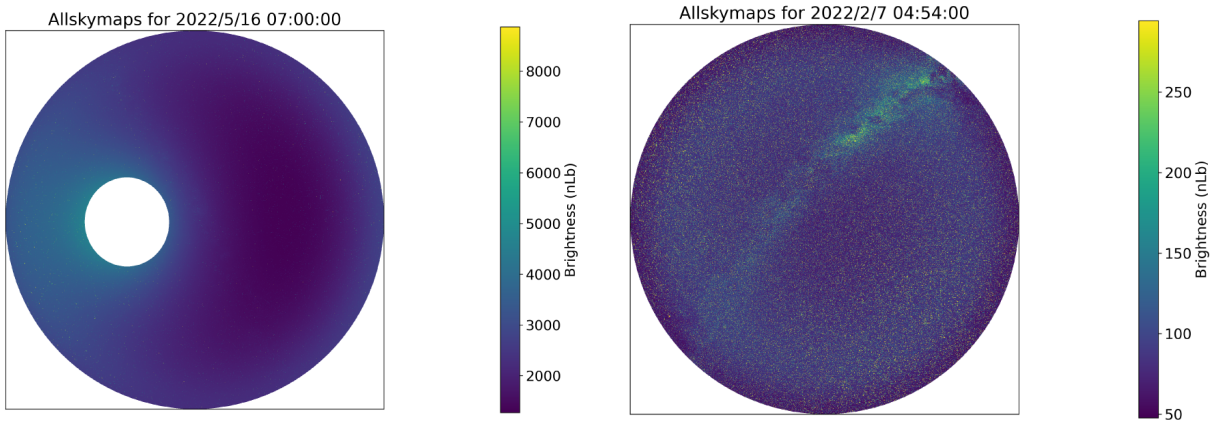

Figure 2.11: All-sky simulations of the NSB for full moon (left) and no moon (right) as observed from the CTA south site for the same region of the night sky. Scattered moonlight outshines all but the brightest stars, Figures from [50]

With the moon being the brightest object in the night sky, its brightness and in turn scattered light are the greatest potential contributors to NSB. One model by Krisciunas and Schaefer (1991) [53] takes the Moon's phase, the zenith angles of the Moon and the sky position, as well as their angular separation, and the atmospheric extinction coefficient to produce predictions of the moon's brightness within 8% to 23% accuracy. Here the amount of first order scattered moonlight that reaches the observer is due to Rayleigh scattering and Mie scattering, also called aerosol particle scattering. The former is can be determined apart from a proportionality constant, but the latter is much more complicated due to the varying distribution of the composition and sizes

of aerosols at different altitudes. Therefore the semi-analytical approach uses an approximation, leading to the model being valid only for angular separations of the target and the moon larger than 10°.
Together with all-sky starlight measurements obtained by the satellite telescope *Gaia* a model simulating the NSB conditions can be derived, that excludes the other contributions mentioned above [50]. Recently it has been demonstrated that utilizing a lower PMT gain while maintaining the pixel trigger threshold in units of p.e. of the H.E.S.S. CT1-4 cameras measurements is possible for both dark-time and partial moonlight observations, while simultaneously reducing PMT ageing [54].

2.6 NSB Measurement

The previously mentioned components of the NSB are usually not constant over a typical run duration. Therefore it is necessary to know the actual NSB rate in each pixel at the time of an event to be able optimize the image cleaning and to match the observations to simulations. There are in principle two methods available to estimate the NSB brightness of CT1-4 and the old CT5 camera and a third one for FlashCam.
The first method utilizes the width in the pedestal distribution [55]. The main purpose of the pedestal is the separation of signal produced by Cherenkov light from any NSB or noise in each pixel. By determining an ADC value equating to the detection of zero Cherenkov photons this pedestal position can be subtracted from all measurements to isolate the signal value. The mean of the distribution of pedestal values will give the pedestal position. Measuring the dark pedestal by closing the camera lid gives a thin Gaussian distribution with the pedestal position as its mean. This width is impacted only by electronic noise and the PMT dark current, making the pedestal temperature dependent. Since the temperature changes of a pixel are around 1°C during a run, the pedestals of each individual pixel need to be redetermined approximately every minute to maintain the precision [55].

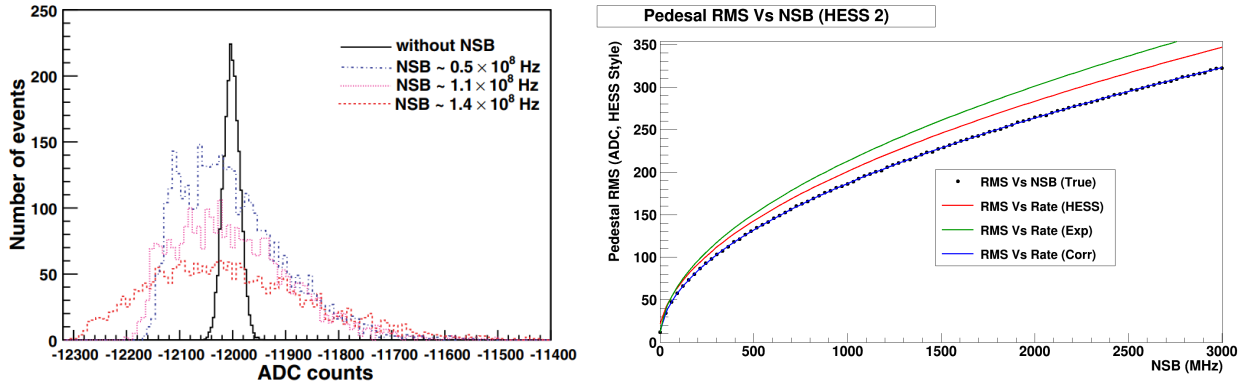

(a) (b)

Figure 2.12: (a): Effect of NSB on the mean and width of the pedestal distributions. (b): Dependece of the pedestal width on the NSB rate, here displayed for the HESS2 camera, Figures from [55]

Figure 2.12 (a) shows the histogram for the dark pedestal, as well as the impact of low to intermediate rates of NSB on the pedestal distribution. Due to the PMTs capacitive coupling to the sampler their signal does not immediately return to the baseline after a pulse. PMT pulses consist of the main pulse and a subsequent negative undershoot before the return to the baseline. The duration of this undershoot is several µs, since the PMTs are in capacitive coupling to the sampler, creating an overlap of many PMT pulse undershoots and a negative shift of the baseline. For NSB rates this is visible in the pedestal distribution, as it is composed of the negatively

shifted baseline distribution of the dark pedestal and a wider single-photoelectron peak. With an increase in rate the distribution changes towards a Gaussian distribution. Apart from some corrections, the root mean square of the NSB will then determine the width of the distribution, as can be seen in Figure 2.12 (b). The NSB can therefore be extracted from the pedestal width by inverting this relationship.
The pedestal position of a pixel is determined by measuring the ADC value during triggered events, provided the pixel contains no Cherenkov light. A pixel is assumed to be possibly contaminated with Cherenkov light if its signal is above a certain threshold or if one of its neighbours is above a threshold. Once every pixel's ADC count was measured a sufficiently high number of times the mean of the distribution of each pixel is taken at the same time. This means that the pedestal is measured in irregular intervals over several seconds. Most satellites pass the FOV of a pixel in less then a second, making the impact their brightness has on the NSB extremely low.

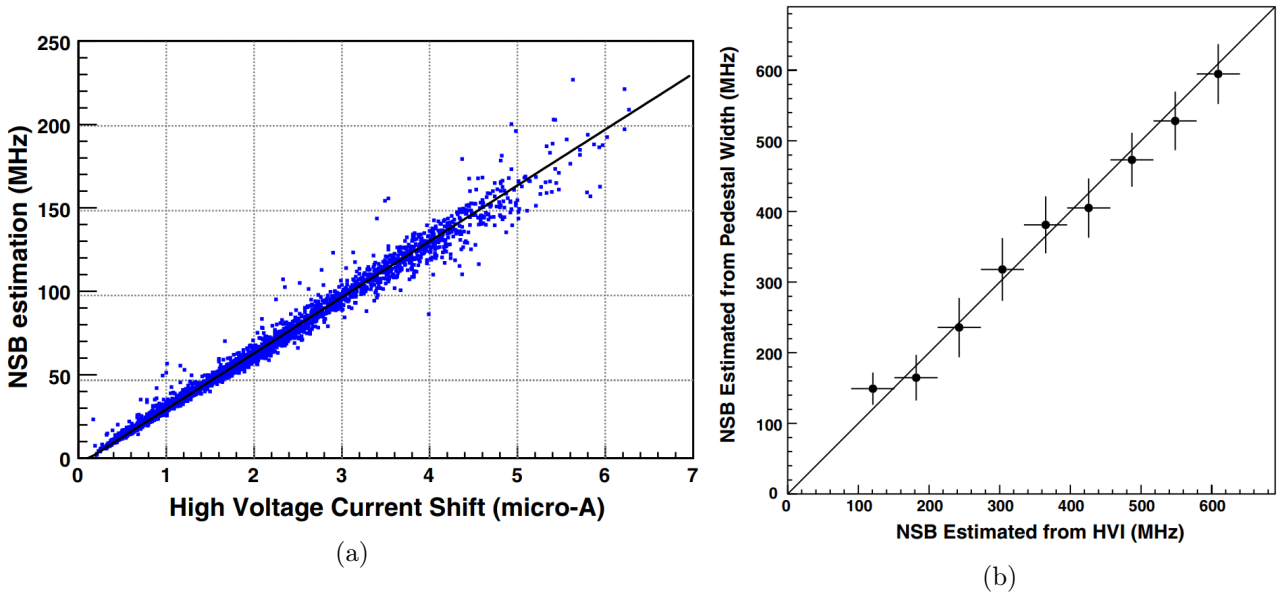

(a) (b)

Figure 2.13: (a)Actual illumination of every pixel of one camera of HESS1 as a function of ΔHVI, (b) A correlation for both estimation methods can be determined for up to moderate levels of NSB rates, Figures from [55].

The second method is to utilize the PMT current drawn from its high voltage power (HVI) supply to infer a NSB rate [55]. The main reason to use this current over the anode current (DCI) that measures the pixel brightness is its negligibly small temperature dependency. The HVI increases linearly with the DCI and has a baseline dark current, the latter is obtained by performing measurements with closed camera lids. A simple linear equation for the NSB rate depending on the difference ΔHVI of the HVI to its dark baseline level can be derived [55]. Figure 2.13 displays this function, as well as the pixel measurements during a test setup, where the NSB rate was known. In principle this approach should be possible for all telescopes, however the current offsets are not stored in the H.E.S.S. database, making this method not functional.
The third method is only possible for FlashCam, since it is the only camera that is DC-coupled . This means that the baseline pedestal value, that is stored for every pixel and event anyway, can be used to determine the NSB rate using a calibration function [35]. To save on disk space, but to have readily available NSB rates per pixel at a given time they are averaged over a 0.1 s time period. This method can resolve the movement of satellites and even meteorites. However this limits the novel satellite detection algorithm that is presented in this work to work only for CT5 measurements taken from October 2019 onward.

2.6.1 NSB Maps

By converting the pixel positions in galactic coordinates using the timing and direction of observation a NSB rate map can be generated for every telescope and run. As an example the left image in Figure 2.14 displays the NSB map of the observed region during the run number 180154, with the corresponding root mean square (RMS) of the measurement on the right. Figures 2.15 and 2.16 display the galactic plane as measured by CT1 and the Large Magellanic Cloud (LMC) by CT5, respectively, each created by merging maps of multiple runs.

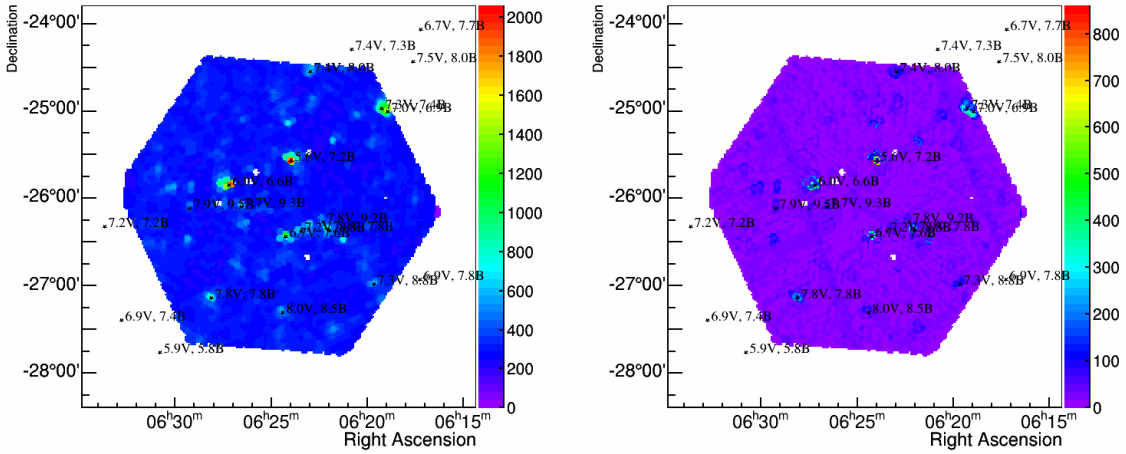

Figure 2.14: NSB map and RMS CT5 from run number 180154, Figures from the H.E.S.S. internal web summary [56]

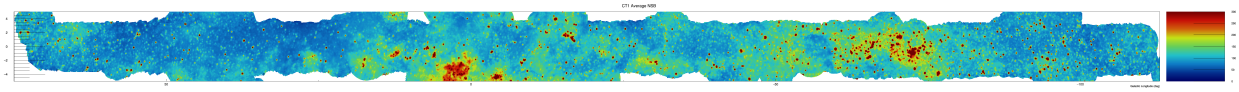

Figure 2.15: Real measurements taken by CT1: optical survey maps of the galactic plane, Figure from internal H.E.S.S. confluence [57]

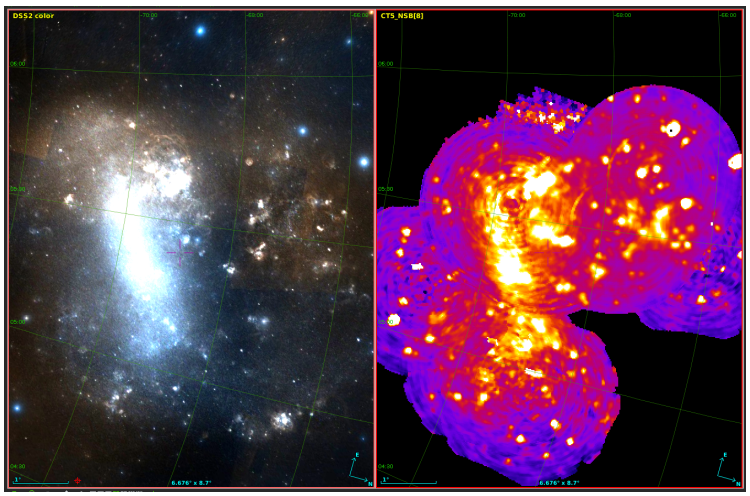

Figure 2.16: Comparisons of the optical and high energy emissions of LMC, left image by the Digitized Sky Survey 2 (DSS2), right NSB measurements by CT5, images obtained from H.E.S.S. confluence [57]

2.7 Image Cleaning

Prior to any image analysis it is important to perform some sort of image cleaning. The goal is to remove as much NSB as possible, which should include satellite trails. One method employed by the MAGIC collaboration uses the correlation in time and space of Cherenkov photons arriving at the camera to remove the uncorrelated NSB signal [58], however this has not been considered as viable for H.E.S.S.
The standard cleaning was historically performed by only considering pixels above a "bright" signal to noise ratio (SNR) threshold and adjacent pixels above a "boundary" SNR threshold, every other pixel is set to be empty [59]. This so-called "tailcut" cleaning is still used for the current standard template based analysis (see section 2.8) [60]. However, for low energy events this method could potenially affect the determination of Hillas parameters, especially the length and orientation angle α. Firstly, because of the generally lower number of pixels passing the threshold cuts, stray pixels with randomly high SNR could influence the Hillas reconstruction more strongly. Secondly, a large number of pixels of low signal containing Cherenkov photons could not reach the required thresholds to be included in the event reconstruction. An example of this effect can be seen on the left picture in Figure 2.17.

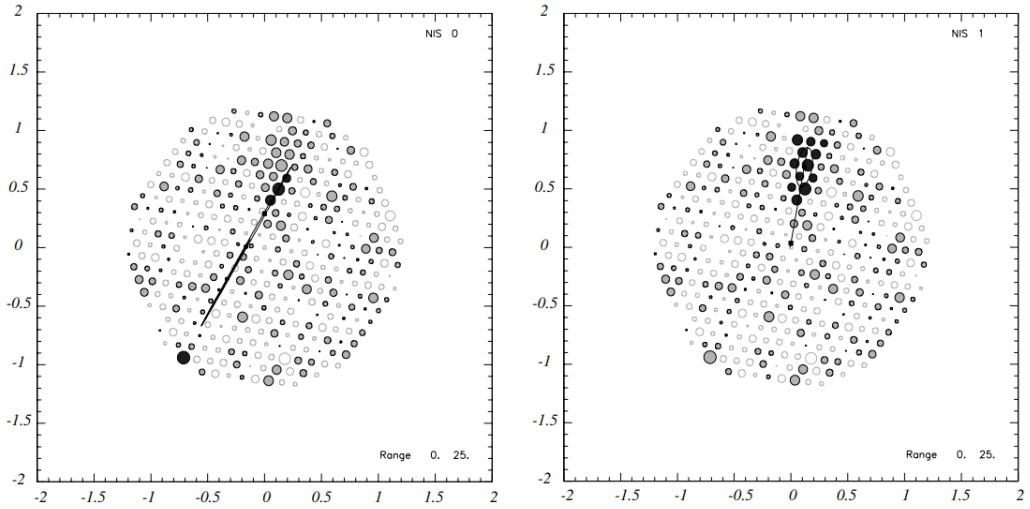

Figure 2.17: Comparison of normal (left) and island (right) cleaning of the same event registered by the Whipple telescope, pixels passing the SNR thresholds and contributing to the reconstruction in each method are shown in black, Figure from [59]

To solve this problem a new island method was developed, with a empty pixels separating the islands of bright or boundary pixels [59]. Excluding entire islands below a new "island" threshold removed spurious pixels and allowed a halving of the necessary bright and boundary thresholds, increasing the significance over all energies and increasing the number of pixels considered in a low energy event, which in turn increases the number of considered events.

2.8 Event Reconstruction

IACTs do not measure the primary particle directly but reconstruct its properties such as kind of primary particle, energy and direction. Originally the reconstruction involved approximating the image as an ellipse and obtain several parameters as shown in Figure 2.18. The so-called Hillas parameters are the image size (amplitude), length (L) and width (W), the orientation angle (α), as well as the polar coordinates of the centre of gravity of the ellipse called nominal distance (d) and azimuthal angle (ϕ). It is possible to obtain the original direction of a shower from the

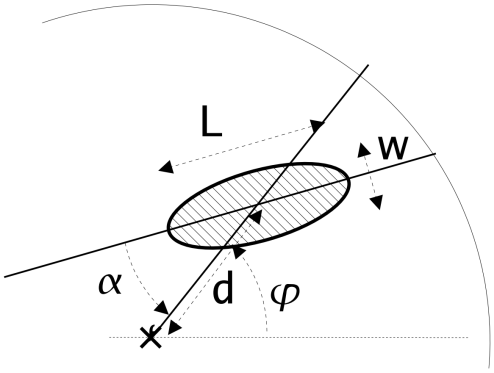

Figure 2.18: Simple geometrical definition of the Hillas Parameters, Figure from [61]

length and size from a single telescope, but not easily: usually lookup tables are required to associate them properly with a source. Similarly the energy can be estimated using the image size and nominal distance. Using multiple telescopes a stereoscopic reconstruction of the source direction is possible by intersecting the major axes of the shower images, and the energy can then be determined by a weighted average of the single telescope energies [61].
The Hillas Parameter can further be used to distinguish γ-ray shower from the background. Figure 2.19 shows the previously mentioned larger lateral spread of hadronic showers compared to the γ-showers. But also other particles like muons, which leave a (partial) ring on the image, or electrons or positrons, which produce subshowers already at higher altitudes, can be distinguished by applying proper cuts on the Hillas parameters, rejecting all non-γ events.

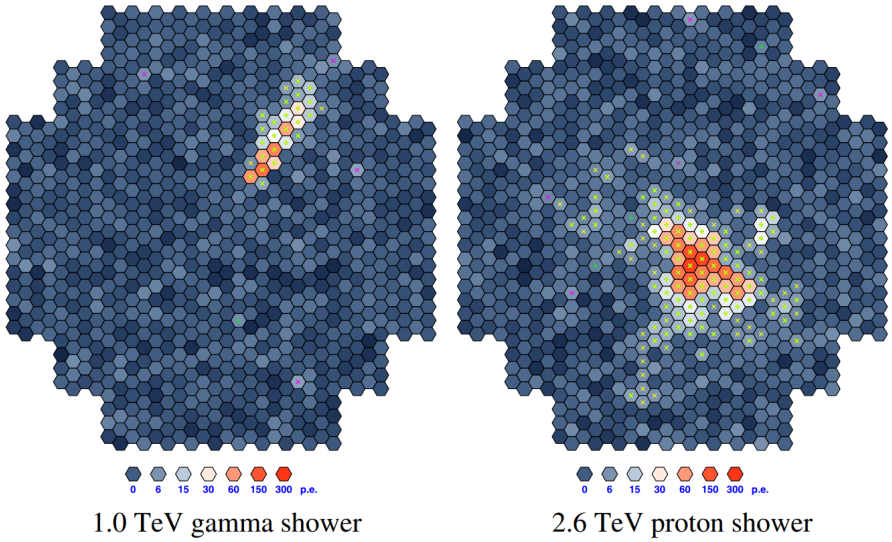

Figure 2.19: Comparison of a leptonic and a hadronic shower image, gamma-like events are much more contained and can be approximated much easier by an ellipse than hadronic showers, Figure from [33]

2.8.1 Boosted Decision Tree

Another classification method improving on the Hillas parameter based approach in terms of sensitivity is the use of *Boosted Decision Trees* (BTDs). Here, a set of parameters M_i based on the Hillas parameters is used to build a decision tree.
The concept illustrated in Figure 2.20 is based on comparing one of those event parameters at each node of a binary tree against a criterion, and assigning the ends of the tree, called *leaves* to

be signal-like or background-like.

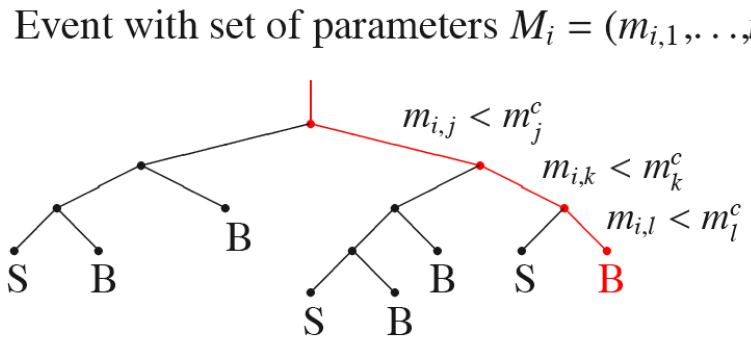

Figure 2.20: Example of a decision tree, marking the *leaves* as signal (S) or background (B), Figure from [62]

Starting at the root of the tree and iteratively for each following node the parameter M_i and its splitting value are determined such that they separate the remaining sub-sample the best into signal and background events. This is repeated until a predetermined number of events remains in the sub-sample or no further separation is possible. The leaves are then denoted as being signal or background, depending on the majority of the remaining events.
Ohm et al. [62] used six parameters that are based on the Hillas parameters to distinguish between γ-ray and hadron events to train their BDT. Four of those parameters are the *mean reduced scaled width* (MRSW), *mean reduced scaled width* (MRSL), *mean reduced scaled width off* (MRSWO) and *mean reduced scaled length off* (MRSLO). Exemplary for all these four parameters the MRSW is calculated by first obtaining the *scaled width* $\mathrm{SCW}_i = (W_i - \langle W_i \rangle)/\sigma_i$ of each telescope i that measured the event, with σ_i being the spread of the expected mean width. Taking the average SCW and introducing a weighting factor $\omega_i = \langle W_i \rangle^2 / \sigma_i^2$ gives the equation

$$\mathrm{MRSW} = \frac{1}{\sum_{i \in N_{\mathrm{tel}}} \omega_i} \cdot \sum_{i \in N_{\mathrm{tel}}} (\mathrm{SCW}_i \cdot \omega_i) \,. \tag{2.4}$$

The former two are comparisons of the measured width and length to their mean expected values in case of a γ-ray as the primary particle, whereas the latter two are those for the case of hadron event. The fifth parameter used is the weighted mean of the reconstructed shower maximum depth X_{max} and the sixth one is the average spread of the energy reconstruction of each triggered telescope $\Delta E/E$.
Since the last two parameters are dependent on the energy and the zenith angle, the training needs to be performed in energy- and zenith angle bands to produce a stable γ-hadron separation. It can be shown that for all events, except for those with energies below 100 GeV, the MRSW is the most important parameter, otherwise it is X_{max} [62].

2.8.2 ImPACT

A more recent technique to reconstruct events is the Image Pixel-wise fit for Atmospheric Cherenkov Telescopes (ImPACT) and is is based on maximum likelihood fitting to Monte Carlo

simulated templates [60]. This method, compared to the Hillas-style reconstruction, shows improvements upon the angular resolution by 50% at 500 GeV to 15% at 100 TeV. Also the energy resolution could be lowered significantly at all energies, especially at low energies, where an improvement of ∼50% was found, while reconstructing the shower maximum $X_{\max}$ accurately and reducing the necessary observation time by a factor of approximately 2.
Although in this work the impact of satellites on the event reconstruction is only analysed for the traditional Hillas parameter based approach, they still could end up affecting the ImPACT method. The background rejection is still performed using BDTs with parameters based on Hillas parameters, and so is the seeding to the fit to the Monte-Carlo simulations.

Chapter 3

Identifying Satellite Trails

This section focuses on the methods employed to obtain the NSB datasets, as well as the used cuts on the data. For comparisons' sake the camera images shown in each step are from the run number 180154, unless stated otherwise The properties of all example runs used in this chapter are displayed in Table 3.1. The script to extract and save the used Hillas parameter files was written by Dr. Samuel Spencer.

Run Number	158838	168632	179687	180154
Observation Target	ToO PKS 0903-57	Kepler SNR	4FGL J0022.0+0006	4FGL J0622.3-2605
Zenith Angle	34.5787°	6.8326°	33.9933°	35.3528°
Sun Elevation Angle	−17.996°	−49.216°	−21.426°	−16.003°
Run Duration	1681 s	1682 s	1692 s	1692 s

Table 3.1: Run numbers and properties of the presented runs in this section. The sun elevation and zenith angle shown here are the values at the beginning of each run

3.1 Analysis Pipeline

3.1.1 Run Selection

A list of runs needs to be found for which the trail detection will be applied. To simplify following analyses only runs of observation type with all five telescopes working that fulfill the HESS II spectral criteria are taken into consideration. These criteria are shown in Table 3.2. For every run in the run selection observational properties from haptools' `Monitor_Run_Trigger` are saved in a separate file called `hessall_Monitor_Run_Trigger.h5`. The first run for which both of these conditions are true occurred on the 28th of October 2019, while the last date of analysed data was the 2nd of February 2023 . Further a run needs to be longer than 10 minutes and have a quality flag of "Good". Runs being flagged as "Bad" can have a variety of reasons, among them are bad weather or atmospheric conditions. Runs that are taken within a 5° radius around the Large Magellanic Cloud (LMC) and η Carinae are also excluded due to those sky regions being particularly bright and being known to cause false triggers [63]. This last cut particularly affects the month of February 2020, as only two runs survive the previous cuts.

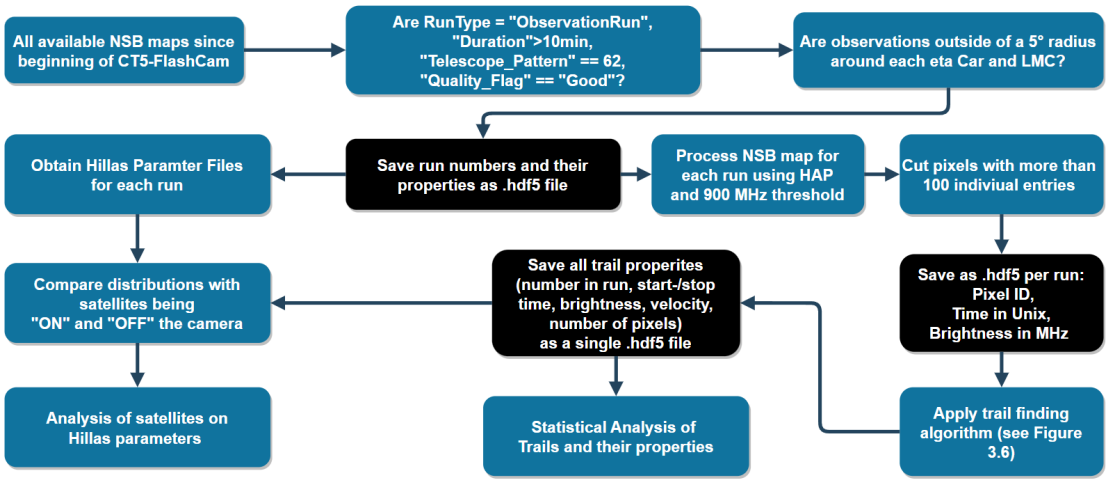

Figure 3.1: General flowchart of the analysis pipeline. A separate saving of data occurs during the steps of the black boxes. The trail finding algorithm will be described in Figure 3.6

Parameter	Cut
Run Duration	>10 minutes
Telescope Trigger Participation Fraction	CT1-4 > 0.4 (w/o CT5), CT1-4>0.04 (w CT5) CT5>0.5
Telescope Tracking	Mean Deviation <1', Deviation RMS >10"
Broken Pixels	CT1-4: "Hardware" <120, "HV Off" <50, CT5: "Hardware" <150, "HV Off" <80
Trigger Rate	CT5>1200Hz
Transparency Coefficient	CT1-4 in range 0.8 to 1.2
System Trigger Rate Stability	$\delta 1$ in range -30% to 30% w.r.t. Mean Value, $\delta 2$<10% w.r.t. Mean Value

Table 3.2: *HAP* run selection criteria. The participation fraction of CT1-4 needs to be adjusted when operating together with CT5 to account for its higher trigger rate [64]. Broken pixels are differentiated between pixels without a high voltage supply (HV Off) and pixels with other,hardware related problems [65]

3.1.2 NSB Value Extraction

Light from satellite reflections is part of the NSB, hence it is logical to search for trails of increased brightness in the NSB database to find them. As the NSB rate is measuring the background illumination of the PMTs, measuring the NSB rate is a measurement of the NSB brightness and the two terms are used interchangeably from now on. Each of the 1764 pixels has a defined position in x- and y-coordinates on the camera, which have been saved once in a separate file called `flashcam_geometry.txt`. Therefore only the pixel-ID is needed for a defined camera position. Together with the UTC timestamp and the NSB rate in MHz they are extracted from the NSB files and saved temporarily in a `.txt`-file.
Satellites operating at LEO make up the majority of satellites and they cross the cameras' FOVs in a matter of seconds (see section 4.1). Therefore, as described earlier, only CT5-FlashCam has a high enough rate of $10\,\mathrm{s}^{-1}$ measuring the NSB to discern satellite trails as such and can even

resolve the much faster travelling meteorites.
The end goal of this analysis is not necessarily going to be to find every satellite trail present in the NSB files, but rather to understand the impact satellite brightness can have on the ability to properly reconstruct γ-ray events. For this reason, as well as for computational costs a cut on the NSB rate of 900 MHz is done. This value was chosen to discriminate against low brightness stars and allow detection of trails independent of observational conditions by considering less bright boundary pixels in the trail reconstruction as well.

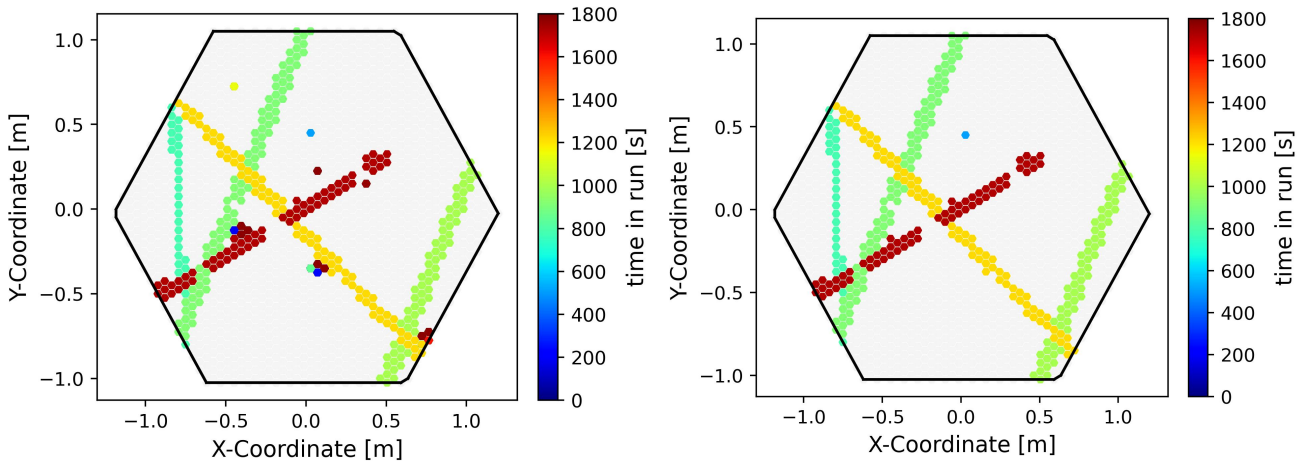

(a) (b)

Figure 3.2: Run number 180154: (a) Last timing of each pixel with a registered brightness corresponding to more than 900 MHz. (b) Image after rejecting every pixel with more than 100 entries, which includes moving stars.

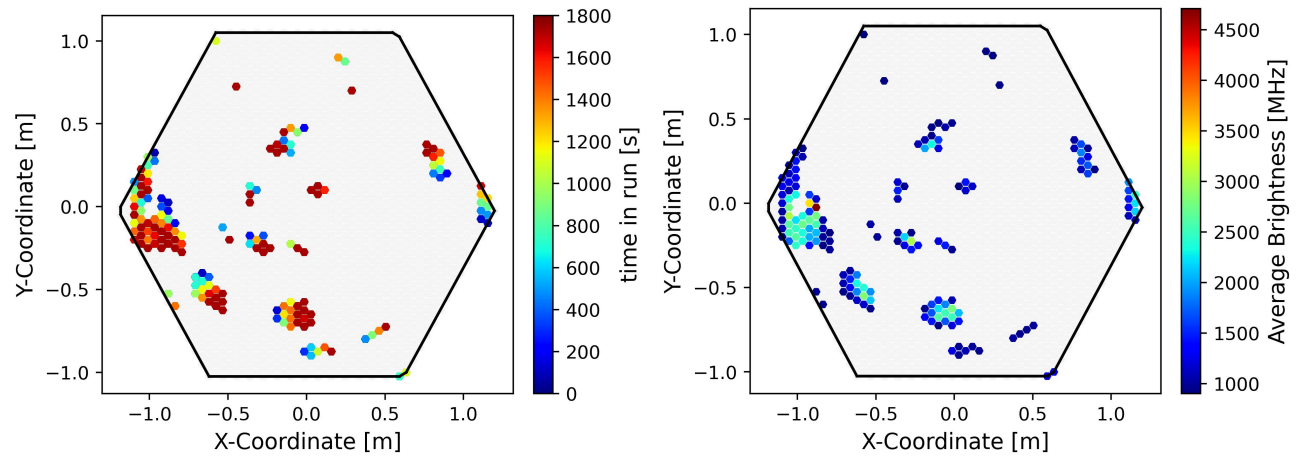

(a) (b)

Figure 3.3: Star positions on the camera will rotate around the centre. Displayed here is run number 158838 with a large number of stars: (a) the last timing of each pixel and (b) the average brightness of those pixels over the cut dataset of one run. For better visibility of the star movement the trails in these images were removed in these images.

Figure 3.2 (a) displays the last timing of each pixel in the dataset for an example run with a large number of trails. Already the five trails can be seen quite clearly, together with stars moving very slowly over the whole duration of the run and other, random, bright pixels. Satellites illuminate an individual pixel only for a comparatively short time, hence by limiting the number of unique entries per pixel to 100, which is 10 s, most non-satellite pixels can be removed. At the same time the UTC times of the remaining pixel entries are converted into Unix time, using the `astropy`

package. A major reduction of the number of data entries is achieved in this way, saving on disk space and accelerating the track finding algorithm. The remaining dataset of the example run can be seen in 3.2 (b), showing that most stray bright pixels are eliminated by this cut while preserving the trails. In this particular run with a relatively high number of tracks a reduction from 161721 to only 660 entries is achieved, but in runs with no detectable satellite trails a reduction to zero entries that pass this cut is possible. In that case a value of -1 is saved for the three parameters and no trail detection is possible for that run, but it still will be taken into account by the statistical analysis. A dataset is obtained in this way for every run in the run selection list and saved as `.hdf5`-files [66].
This cut creates some limitations though. Pixels that at some point during the run were illuminated by a star for more than 10 s are removed entirely and create gaps in any potential satellite trail reconstruction. Due to the camera's movement during a run stars show an apparent rotational movement on the camera image, which further increases the number of pixels removed by that cut. For this reason the LMC and η Carinae regions were excluded in the run selection. Figure 3.3 shows the timing of the NSB rates during a run with a large, but manageable number of bright stars. The following section 3.2 will describe, how this problem is handled in the trail reconstruction.

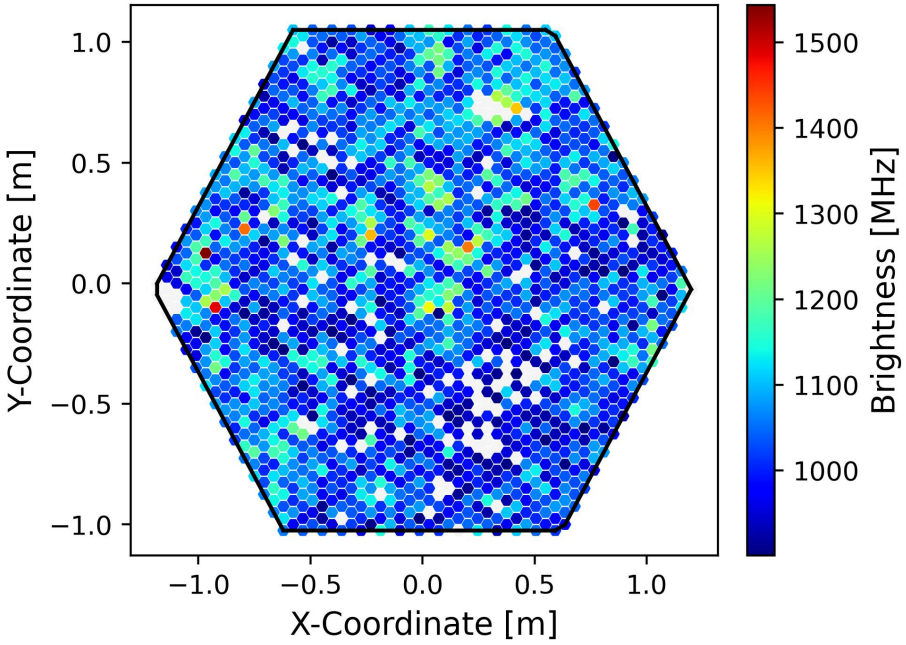

Figure 3.4: Flare-up of almost the entire camera during the same 0.1 s time window seen in run number 179687, with the nearest time to any entry in the remaining dataset being approximately 10 s. This seems to occur randomly in several instances, the origin for that effect is unknown.

It turns out that there are several runs in which a large fraction of the pixels pass both cuts. In those it appears that sections from a few tens to almost all pixels are illuminated at the same time for only 0.1 s, occurring multiple times during a run. Figure 3.4 shows the brightness distribution of one such occurrence affecting a large portion of the camera during a run. If these "camera flare-ups" happen often enough they can also contribute to the removal of some to all pixels from the dataset, effectively reducing the number of detectable satellite trails.

3.2 Neighbourhood Finder

The track sorting algorithm explained in the following section 3.3 utilizes a definition of a spatial neighbourhood, that will be explained briefly here.

For other purposes in the event analysis processes the neighbours and next-neighbours are already defined for every pixel. However in order to reconstruct trails with gaps larger than one pixel a new neighbourhood definition was needed. For this a relatively simple approach was used, in which the neighbourhood of each pixel is defined by a $0.5 \cdot 0.5\,\mathrm{m}^2$ box around it.

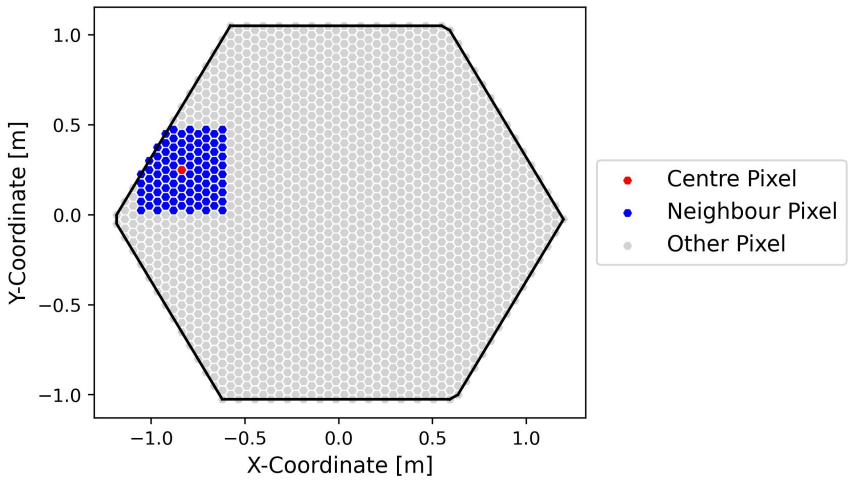

Figure 3.5: Image showing all pixels considered as neighbours (blue) to a pixel

Figure 3.5 illustrates this for a pixel at the edge of the camera. A `numba.List` of `numba.Lists` called `typed_nn_pix` gives the neighbourhood pixels for all pixel IDs.

3.3 Track Sorting Algorithm

3.3.1 Parallelization and Just-In-Time Compilation with Numba

To circumvent the comparatively slow single threading issue of Python, the analysis pipeline is written in a way, that multiple runs can be evaluated in parallel. To achieve this the code is written that from the NSB file extraction to the trail finding algorithm a per run evaluation is possible.
Secondly to optimize numerical computations the Just-in-Time (JIT) Python compiler Numba is used. It translates Numba decorated functions directly into machine code at runtime by analyzing variable types beforehand, increasing the performance of Python especially in cases where many loops are present. The most important Numba decorator and the only one used in this work is the `@jit` decorator, which mainly will increase the speed of the track sorting algorithm.
Numba has some limitations in implementing all features Python and NumPy. One particular issue was the limitation on the use of nested lists. For this Numba provides the `numba.typed.List` data type. In typed lists all elements need to be of the same type, which in this case will be `float`. They are also more limited in terms of available operations and methods, which was accounted for. It needs to be mentioned that the typed list is an experimental feature of Numba, but so far no issues have been recorded.

3.3.2 Algorithm

Figure 3.6 shows a flowchart of the track sorting algorithm. The dataset of the pixel IDs, time stamps and brightnesses of one run is read into the three lists called `pix`, `time` and `brightness` and those are read as elements of the variable `data`.
At the beginning of the track sorting algorithm a temporary variable `tracks` is declared as an empty `numba.typed.List`, which at the end will contain all detected satellite tracks in that run.

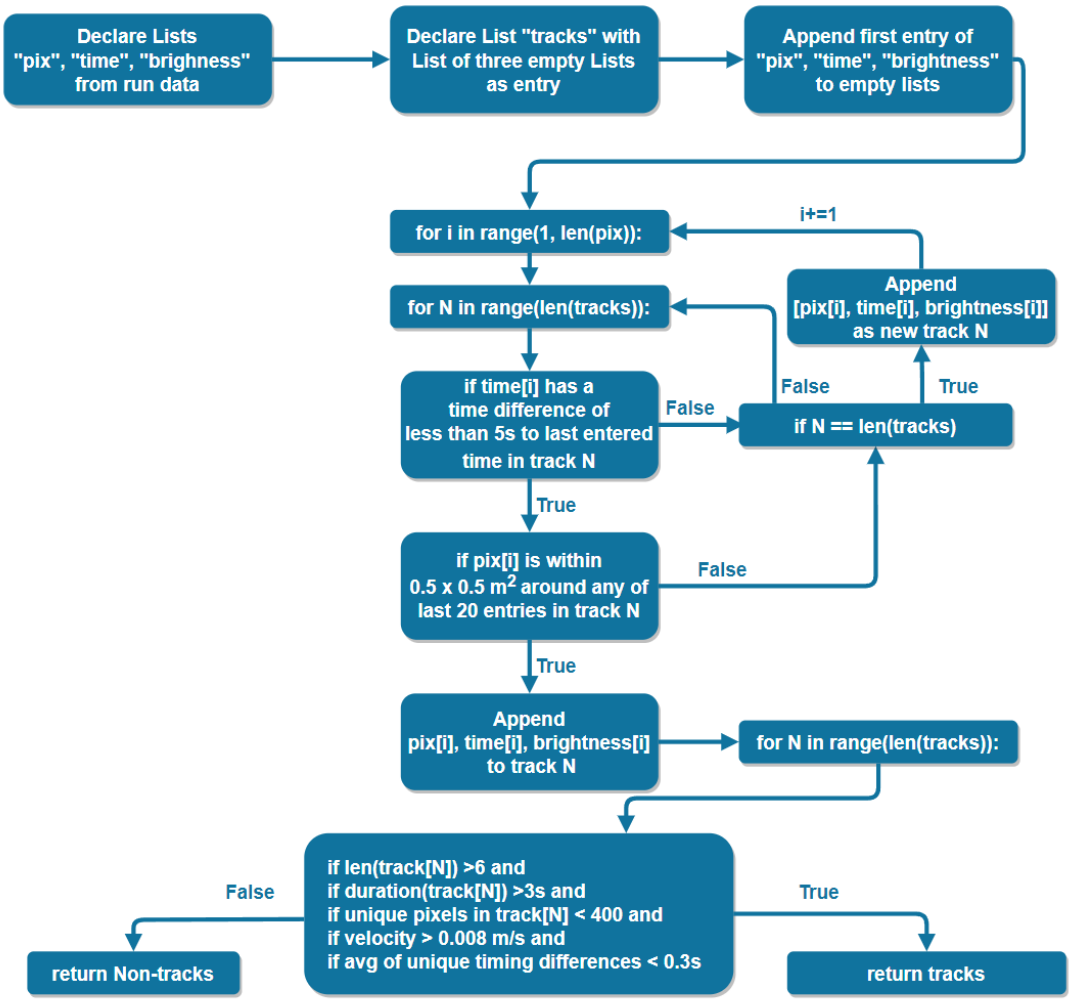

Figure 3.6: Flowchart of the pseudo code written in Python of the track sorting algorithm

The use of this experimental feature of Numba allowed nested lists to work with the compiler. A limitation of Numba is the restriction to a single datatype in a list, which here is simply solved by converting `pix` into a list of `float` elements. Another `numba.typed.List` with three empty `numba.typed.List` as elements is then appended to *tracks*, before the first entry of each `pix`, `time` and `brightness` is appended to one of the empty lists. The idea behind the algorithm is to first sort every single data point of the remaining NSB dataset into a track, regardless if it actually belongs to a satellite. The code loops over the remaining entries of `pix` and over all tracks in `tracks` to decide to which track the data entry is appended.
Precisely for this loop of a loop Numba was used, as it speeds up those operations. First it is checked, if the `time` of last entry of the track has a difference of less than 5 s and secondly if the currently checked pixel is within the neighbourhood as defined in section 3.2 of the last 20 entries of the track.
If a suitable track has been found the loop over `tracks` breaks and is continued for the next entry in `pix`. In case of no matching tracks a new one is created and appended to `tracks`.
`tracks` now contains the satellite trails, but also those of meteorites and other, randomly bright pixels not associated with a trail.
Using this method reconstructs trails, but also creates connections between the remaining, randomly bright data entries. To discriminate for satellite trails each track must pass a number of conditions. Each track that is found to be not satellite-like is removed from `tracks` and added to a new `numba.typed.list` called `non-tracks`. The first cut excludes tracks with less than 6

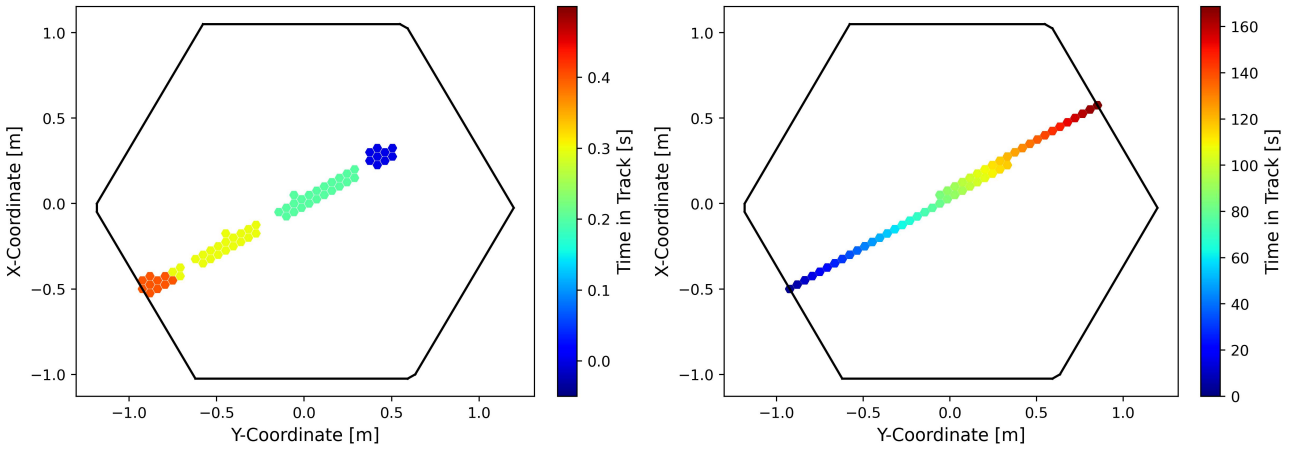

Figure 3.7: (a) Example of the very fast trail present in run number 180154, thought to be caused by a meteorite, (b) longest duration trail that was detected using the 900 MHz brightness threshold.

and more than 400 unique pixels. The lower boundary removes most of the remaining, randomly bright noise, as often times only a single pixel is inside a track. The upper boundary was set to still include extremely wide trails that travel through the camera centre.

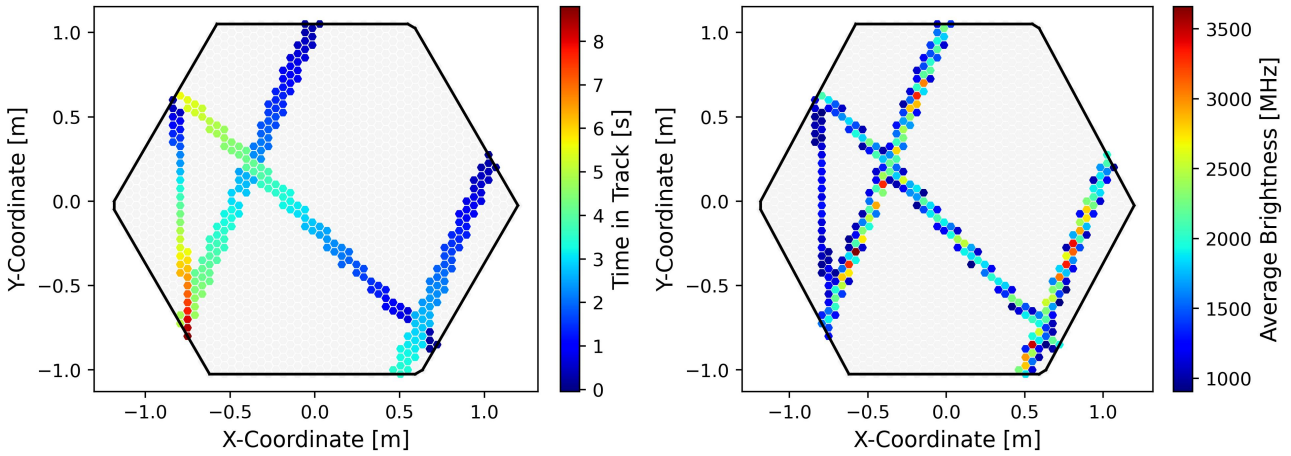

Figure 3.8: Four satellite trails detected in the run 180154. Z-axis here denotes (a) the time from the last triggering pixel in each trail and (b) the average brightness in a pixel.

Next a cut on the trail duration is done due to the expected crossing times of satellites (see section 4.1). To factor in the possibility of a trail not crossing the full FOV of 3.4°, incomplete trails or a crossing at the edge of the camera the minimum time was set to be 3 s. This also removes the fast travelling meteorites, like the one in Figure 3.7 (a), which crosses the camera's FOV in about half a second. No other phenomenon on the night sky creates trails of similar duration and brightness. In comparison to this is the trail with the longest duration, as seen in Figure 3.7 (b) It was visible at the required brightness for 168.6 s crossing the camera at an average velocity of 0.0196°/s. The velocity of a trail here is calculated by determining the length in degrees of the vector from the average pixel position of the first timing to the average of the last timing and dividing that length by the trail duration.
The relatively loose time proximity condition allows close pixels with randomly high values to create a trail, with a more or less random distribution of positions. To remove those the last two cuts are used. If the first and last entry of a suspected track are not at the beginning and end of

it, the calculated velocity is lower. By setting the minimum velocity to 0.008°/s it is theoretically possible to detect even the slowest non-elliptical MEO satellites [2]. The second one is based on the fact that in a continuous trail the difference between unique timings is always 0.1 s. A cut removes the tracks with an average of the differences of unique pixel timings exceeding 0.3 s.
The return values of the track sorter are the two Numba typed lists `tracks` and `non-tracks`. In case of an empty list the return value will be the same nested list structure with values of -1 for `pix`, `time` and `brightness`.
Finally the tracks can be displayed in a single plot as is done in Figure 3.8. The run used is the same one as the one as in Figure 3.2, the fifth trail has been determined to be a meteorite trail, which was displayed in Figure 3.7 (a). Also visible now is that the two parallel tracks move at a similar velocity in the same direction, indicating that they belong to a satellite train.
For each trail several properties are calculated and saved to a separate `.txt` file. These are

- Run number and its starting time in unix
- Number and duration of the track in the run
- Average and maximum brightness
- Start and stop time in Unix time
- Time in seconds after UTC midnight
- Number of unique pixels
- Velocity in °/s

If a run has no detected trails, then all values except for the run number and the run start time are set to -1.

3.4 Broken Pixel Fraction

The performance for each pixel over the course of a run is impacted by the fraction of time it actually operated. For this H.E.S.S. measures the time fraction a pixel was turned off during a run, which is called *Broken Pixel Fraction*. It helps in assessing the quality of the data, accounting for any potential biases or limitations in the observations.
Obviously, the already mentioned "HV-Off" and "Hardware" pixels of Table 3.2 will be included too. Aside from hardware-related issues, a pixel can also be turned off in order to preserve the PMTs. The pixels have an in-build safety mechanism, that briefly turns them off if the brightness becomes too high. It needs to be noted, that the pixels turned off by this safety feature are not considered as broken for the purposes of the run selection [65]. To turn off a pixel in CT5-FlashCam the brightness additionally needs to be registered for a sufficient amount of time. Typically that brightness is caused by the movement of stars through the pixel's FOV, but trails created by satellites or meteorites have the potential to be bright enough, too.
Therefore the Broken Pixel Fraction could be used to find very bright satellite trails. By using the times at which the pixels were turned off it should in principle be possible to determine most of the trail's properties, too. An advantage over the presented method using the NSB data of CT5-FlashCam is that this would allow for an investigation of all telescopes over a larger time period. Indeed, in the example run 180154 from above a trail can be seen in the Broken Pixel Fractions of CT1-4, which is displayed in Figure 3.9. However this trail belongs to the one meteorite detected in that run, while the four satellites found are below the necessary brightness threshold. This shows, that using this method would severely undercount the total number of detectable satellites that could potentially influence astronomical observations.

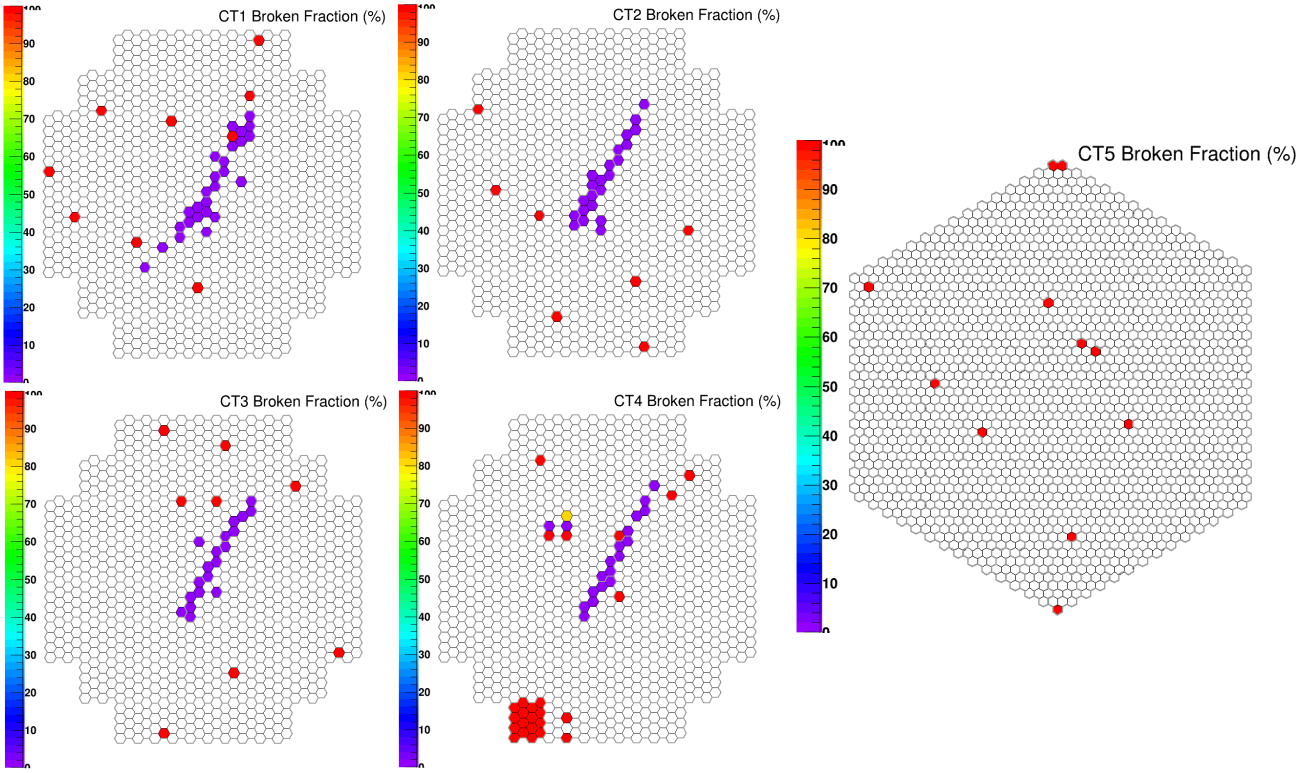

Figure 3.9: Example of the Broken Pixel Fraction defined as the fraction of the run a pixel was turned off. A trail belonging to a meteorite can be seen in CT1-4, but not in CT5, as the camera can tolerate significantly higher NSB rates before the safety precautions take effect.

3.5 ATOM Camera

Figure 3.10: Allsky image taken by the ATOM camera at the H.E.S.S. location that shows a rare airplane crossing the cameras FOV. Due to the blinking of various colors their trails can easily be distinguished from those left behind by satellites or meteorites, image from [67]

The Automatic Telescope for Optical Monitoring (ATOM) is an 80 cm telescope located less than one kilometer away from the H.E.S.S. observation site [68]. Its all-sky measurements of the optical wavelength range are made fully robotically and can be used as triggers for so called "Target of Opportunity" (ToO) observations. These triggers can occur whenever a flare of one of the γ-ray sources monitored by ATOM is detected. Further it records changes in the atmosphere, like the emergence of light clouds. If possible, the H.E.S.S. telescope can then be pointed towards unobscured sky regions.
ATOM regularly sees single colored, usually white trails of satellites and meteorites, and in principle it could be used to find out, if they cross the H.E.S.S.' FOV. However this method would only work as sort of an indicator for which runs contain satellite trails, and they would still have to be found in the NSB data to determine their brightness and exact camera timings as detected by H.E.S.S.
Figure 3.10 shows an image taken by ATOM, that prominently shows the characteristic multi-colored blinking trail of an airplane. They are rarely detected by ATOM and it is assumed, that no airplane trails contaminate the collected trail data, with Section 4.1 mentioning in more detail how this assumption is validated.

Chapter 4

Statistical Analysis of Trails

This chapter will focus on the characteristics of the trails found by the approach outlined in the preceding Section 3.

4.1 Duration

In this section the trail durations will be discussed. First the logarithmic duration histogram displayed in Figure 4.1. Poissionian statistics for the counting of the trails is assumed.

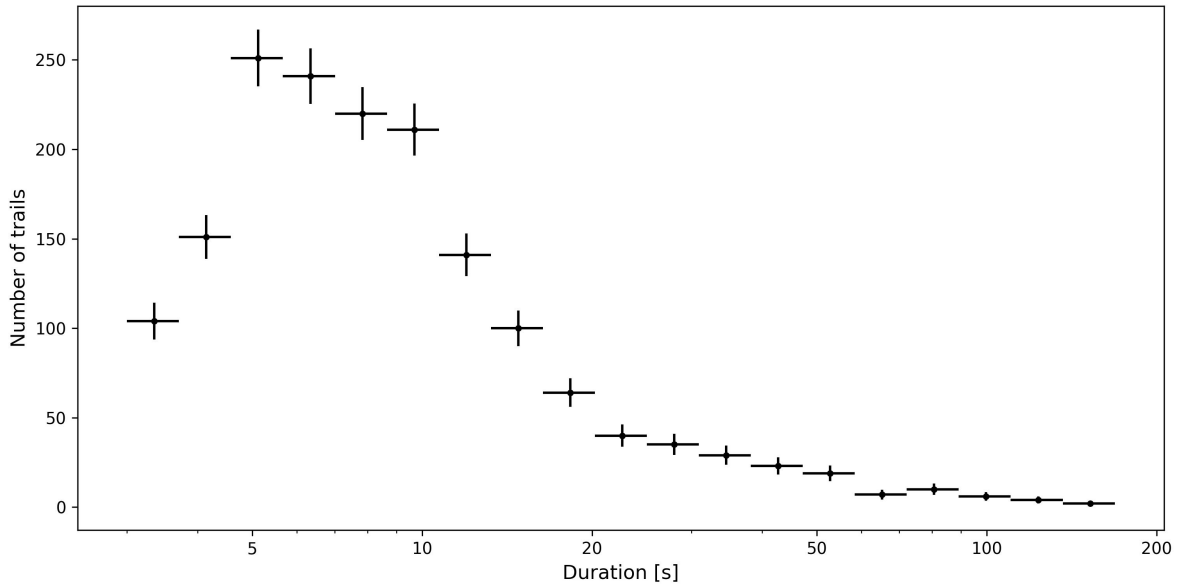

Figure 4.1: Histogram of duration of tracks

89.7% of all detected trails have a duration of less than 20 s. As will become clear in the following explanations those shorter trails contain all detected trails from Starlink and OneWeb. Therefore it is expected that with the increasing number of LEO satellites that fraction is going to increase. The duration was also a major factor in the rejection of non-satellite trails, hence it is useful to discuss why the chosen value of 3 s is appropriate. For this the time a satellite takes to cross the full camera FOV depending on its orbital altitude and the zenith angle of the observation is determined. In the following calculations only non-elliptic satellite orbits are taken into account, since the vast majority of current and planned future satellites are in LEO. For circular orbits at altitude h the velocity is calculated as

$$v = \sqrt{\frac{G \cdot M}{R + h}} \tag{4.1}$$

with the gravitational constant $G = 6.67 \cdot 10^{-11}\,\mathrm{m^3\,kg^{-1}s^{-2}}$ and Earth's mass $M = 5.97 \cdot 10^{24}\,\mathrm{kg}$ and radius $R = 6731\,\mathrm{km}$.
The shortest distance travelled across the camera occurs for measurements with a zenith angle of zero. It can be approximated by simplifying the travelled distance d to be the base of an isosceles triangle with the FOV as the opening angle, therefore $d = 2 \cdot h \cdot \tan(\mathrm{FOV}/2)$. For a typical altitude of the current Starlink satellites of 550 km the shortest possible crossing times $t = d/v$ are then 6.3 s and 4.3 s for CT1-4 and CT5-FlashCam respectively. As a comparison a commercial airplane with a velocity of 900km/h and a cruising altitude of 10 km takes only 1.9 s. This also means that all trails with a length longer than 2.3° will pass the 3 s cut, as the time a satellites takes to cross the camera's FOV is expected to increase with higher zenith angles.
The following considerations in Figure 4.2 do not take Earth's rotation into account and are only viable for satellites with an eccentricity of close to zero. Since this is used to only get an estimate for the possible duration times those deviations are negligible for the vast majority of satellites.

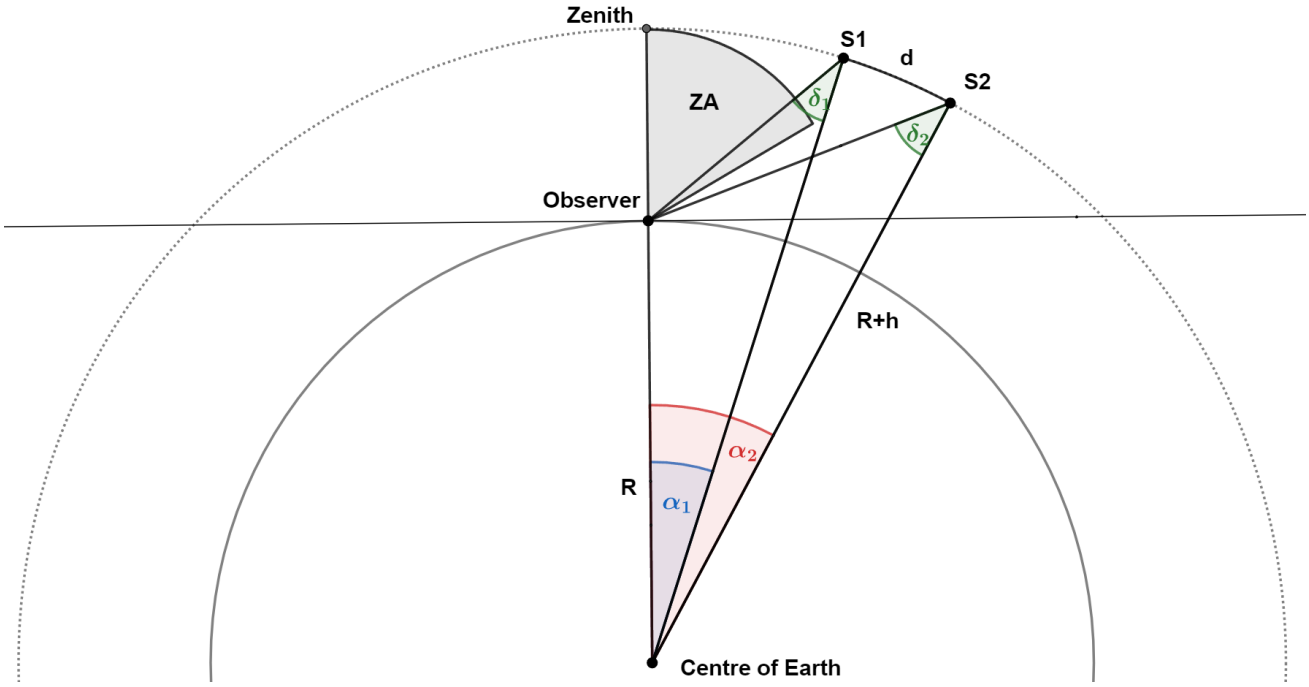

Figure 4.2: Geometry to determine the maximum duration of a satellite crossing

At a non-zero zenith angle the travelled distance in the FOV of the camera is dependent on the satellite's travel direction w.r.t. the horizon, with a movement parallel to the horizon being the shortest and perpendicular being the longest distance. An approximation using the intercept theorem for the former can be obtained be multiplying the distance calculated at the zenith angle with the factor $\overline{\mathrm{OS}}/h$, with $\overline{\mathrm{OS}}$ being the distance from the observer to the satellite. However, giving a lower limit for the possible duration times for a given altitude is not really feasible, since tracks shorter than the FOV are possible too.
The geometry for calculating the upper limit for a given altitude h is shown in Figure 4.2. The points S1 and S2 are defined as the edges of the camera, hence the individual zenith angles are $z \pm \mathrm{FOV}/2$. First the angles in the triangle of the observer, the centre of the earth and the edges of the camera S1 and S2 are determined. The angles at the observer are

$$\beta_{1/2} = 180° - \left(Z \mp \frac{\mathrm{FOV}}{2}\right) \tag{4.2}$$

Using the law of sines the angles at at S1 and S2 are calculated as

$$\delta_{1/2} = \sin^{-1}\left(\frac{R}{R+h} \cdot \sin\left(Z \pm \frac{\mathrm{FOV}}{2}\right)\right) \tag{4.3}$$

It follows that the zenith angles in relation to the centre of the Earth are

$$\alpha_{1/2} = 180° - \beta_{1/2} - \delta_{1/2} \tag{4.4}$$

$$= \left(Z \mp \frac{\mathrm{FOV}}{2}\right) - \delta_{1/2}, \tag{4.5}$$

Their difference is used to determine the circle sector distance

$$d = \frac{\alpha_2 - \alpha_1}{360°} \cdot 2\pi \cdot (R+h). \tag{4.6}$$

Together with the orbital velocities the upper limit for the duration of the visibility of a satellite on the camera can be derived to be

$$t_{\max}(h, Z) = \Delta\alpha(Z) \cdot \frac{2\pi}{360°} \cdot \sqrt{\frac{(R+h)^3}{G \cdot M}} \tag{4.7}$$

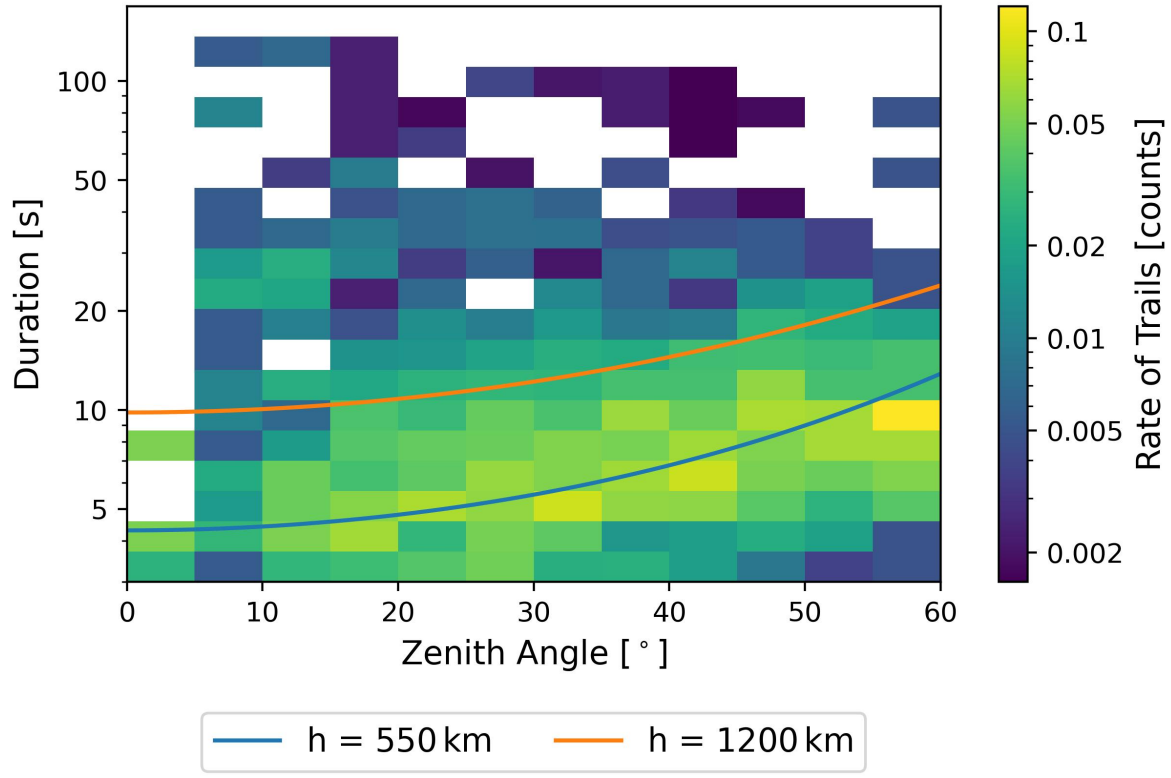

Figure 4.3: 2D-histogram of zenith and duration of tracks with the maximum duration for typical Starlink (550 km) and OneWeb (1200 km) satellite cruising altitudes as a function of zenith angle.

As a short aside: this geometry can also be used to determine aircraft crossing durations. With the above airplane properties the minimum zenith angle for which the 3 s criterion is met is 28°. It needs to be stressed that this zenith angle necessitates that the airplane travels directly over the observatory. Furthermore it follows that the maximum possible duration at 60° zenith angle is 7.4 s, making it impossible that slower trails could be misidentified as airplanes. Considering that airplanes in the night sky over the H.E.S.S. site are still quite rare it is reasonable to assume

that no detected trail belongs to an airplane.
Figure 4.3 shows a 2D-histogram of the detected rate of trail durations and zenith angles. The rate is determined by dividing the true number of trails in a bin by the total number of runs in that zenith angle range. Over the rate the Equation 4.7 is plotted for the altitudes 550 km and 1500 km, which correspond to the altitude populated by Starlink satellites and the border of LEO satellites respectively, showing that the measurements are in agreement with the theory. The trails above that line can therefore be attributed to satellites outside the major satellite constellations. Figure 4.3 also indicates that non-LEO satellites will be detected more frequently at lower zenith angles. This might be an inherent bias though, as the satellites are closer towards the observer, appearing brighter and passing the 900 MHz NSB rate threshold more easily.
The longest duration trail detected with its 168.6 s was presented already in Figure 3.7 (b). Using the zenith angle of 6.83° in equation 4.7 would result in an altitude of ∼12900 km. According to the UCS database [2] only satellites with elliptical orbits operate at that altitude. However this was not the slowest trail detected, mainly due to the fact that the slower trails in the dataset left a shorter track on the camera.

4.1.1 Trail Length

Due to the chosen cuts on the data the constructed trails will inadvertently be cut short in some cases. In this work the trail length is calculated by drawing a vector between the average position of the first and last time stamp and multiplying the value by the pixel size 0.08°/0.05 m= 1.6°/m. This method inadvertently results in slightly shorter trails, as the the distance is calculated not from the edges of an averaged pixel position, but rather from the pixel centre. Luckily this can be resolved in future iterations of the analysis by simply adding 0.08°, the length of a pixel, to the result.

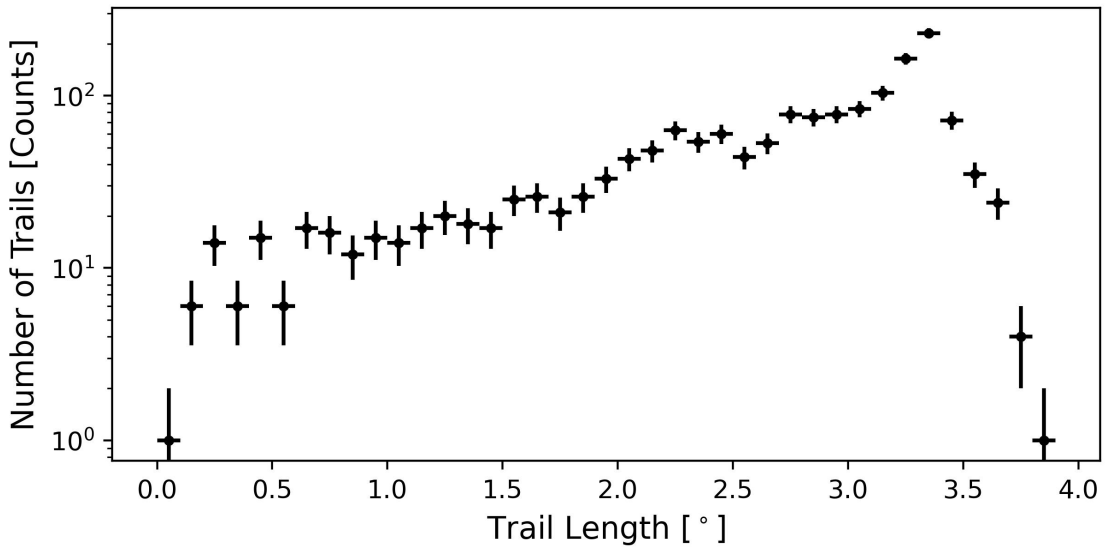

Figure 4.4: Distribution of the trail lengths

The first thing that is noticed in Figure 4.4 is that there is a non-negligible amount of trails with a length larger than the previously given 3.4° of the camera. That value is equivalent to the short diagonal, i.e. the distance from opposing sides. The large diagonal of a regular hexagon is 1.15 times larger than the short one, meaning that the theoretical upper limit of possible trail lengths is 3.91°, which nicely aligns with the longest measured trail length of 3.80°.
The trail length is also used in the determination of a satellite's velocity on the camera by simply dividing it by the duration. Figure 4.5 shows absolute number of trails as a 2D histogram of the

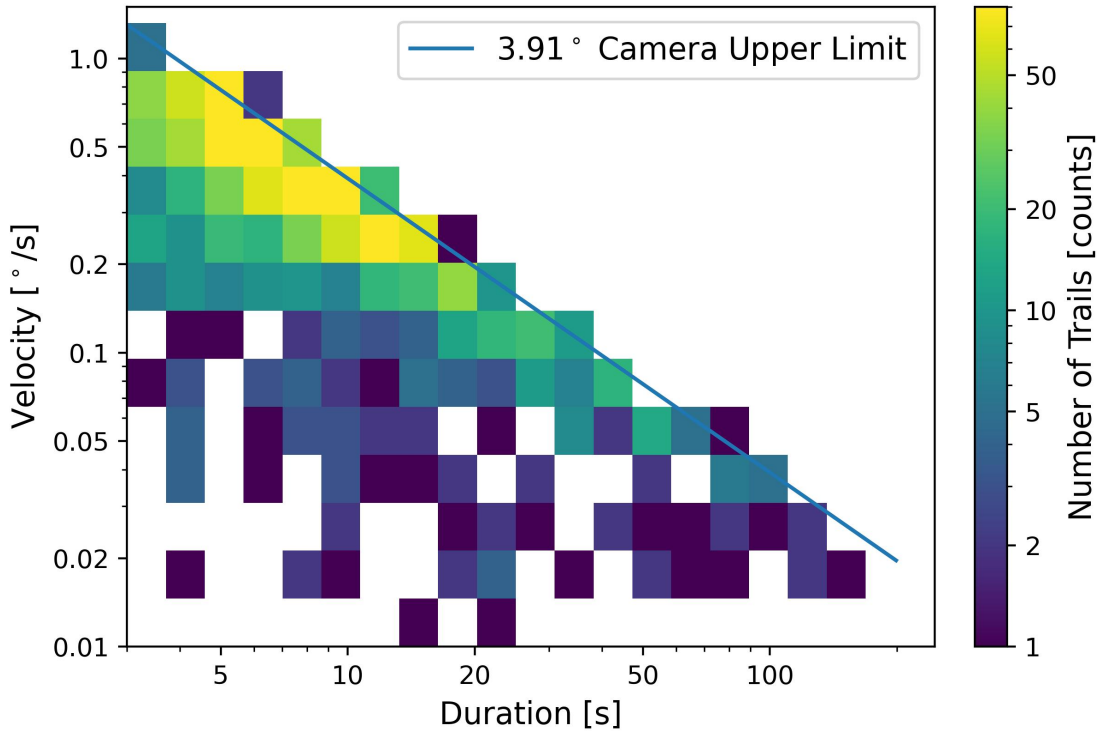

Figure 4.5: 2D-histogram duration and velocity

duration and the trail velocity. Since their product gives the trail length it is to be expected that all trail velocities should fall below the function $3.91°/t$.

4.2 Dependence on Zenith and Sun Elevation

According to Hainaut and Williams [17] an approximation for the fraction of satellites of a constellation with $N_{\text{Const.}}$ satellites at an altitude h above a certain zenith angle Z can be calculated as the fraction between the area of the sphere with radius $R_{\text{sat}} = R + h$ and a spherical cap with a height h_z. The latter is calculated as the difference between h and the height of the satellite above the horizon and can be obtained using a similar geometry as in 4.2, such that $h_z = (1 - \cos(\alpha) R_{\text{sat}})$. Hence the number of satellites in that cap is calculated to be

$$N = N_{\text{Const}} \frac{A_{\text{cap}}}{A_{\text{total}}} \tag{4.8}$$

$$= N_{\text{Const}} \frac{2\pi R_{\text{sat}} \cdot h_z}{4\pi R_{\text{sat}}^2} = N_{\text{Const}} \frac{h_z}{2R_{\text{sat}}} \tag{4.9}$$

$$= \frac{N_{\text{Const}}}{2} \left(1 - \cos\left(Z - \sin^{-1}\left(\frac{R}{R_{\text{sat}}} \sin(Z)\right)\right)\right) \tag{4.10}$$

For simplicity this approach deliberately neglected the dependence of the satellite distributions on the latitude, the effects of which were explained in more detail by Bassa et al. [69], which is not considered here. Furthermore this number ignores whether a satellite actually is illuminated or not. To determine the area of a satellite in a zenith angle range from Z_i to $Z_{\text{i+1}}$ the difference of the spherical of the two zenith angles can be used. It follows that the fraction of satellites

potentially visible in a zenith angle bin can be determined by

$$f = \frac{A_{\text{cap}}(Z_{i+1}, R_{\text{sat}}) - A_{\text{cap}}((Z_i, R_{\text{sat}})))}{A_{\text{total}}}, \tag{4.11}$$

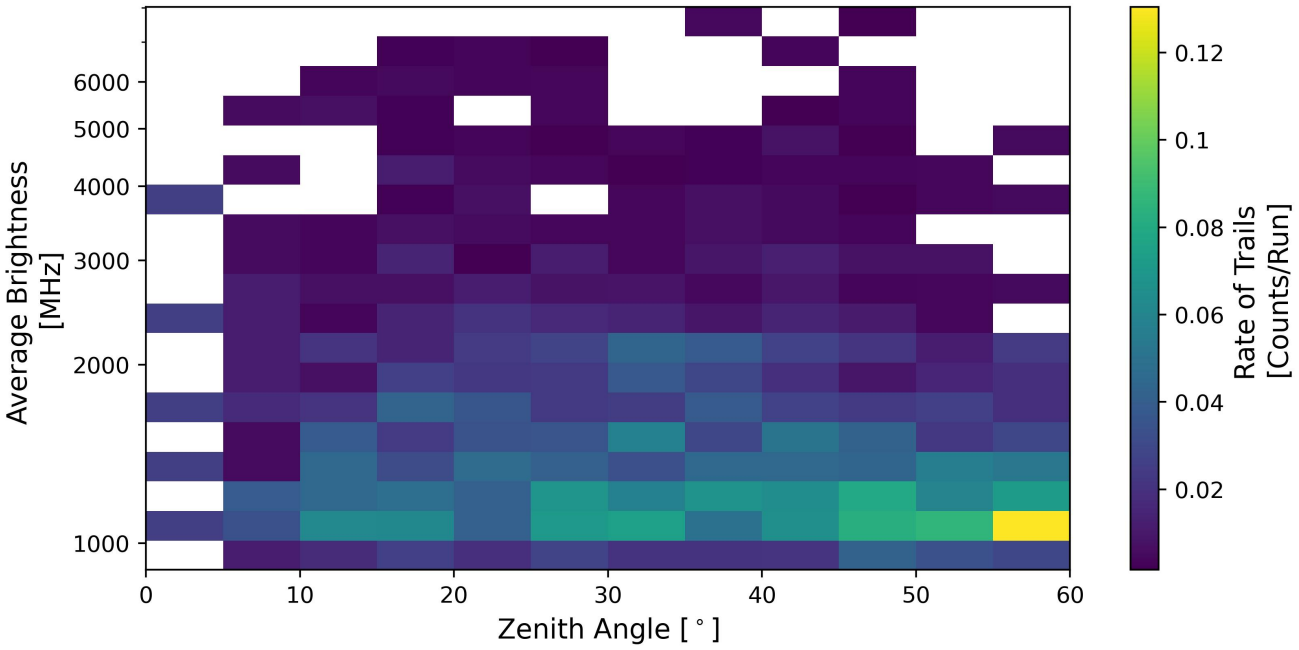

Figure 4.6: Trail rate as a function of zenith angle and brightness

This would yield an ever increasing fraction of potentially visible satellites. However Hainaut and Williams [17] have shown, that the apparent satellite magnitude for LEO satellites starts to drop noticeably for zenith angles $\gtrapprox 20°$. This is due to the increasing distance to the satellite and larger traversed air mass volume, which increases the extinction. Figure 4.6 shows the increasing rate of trails with the zenith angle while their brightness is reduced. Averaging over all brightnesses in Figure 4.7 an increase in the rate is visible up until the above mentioned drop in magnitude after which the rate plateaus.

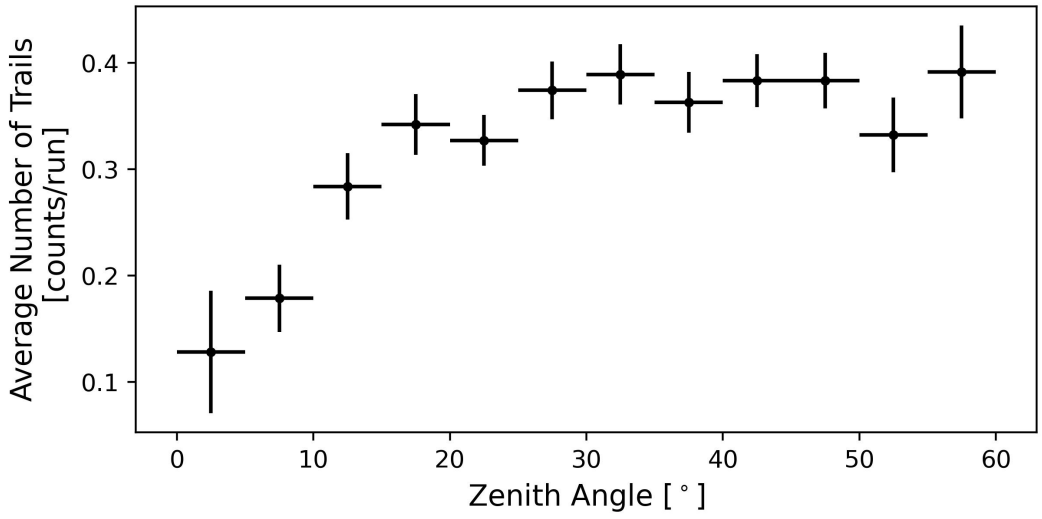

Figure 4.7: Average number of trails per run per 5° bin. Error on the number of trails is due to the random distribution of satellites estimated to be Poissonian.

Since a satellite is only visible in the observed wavelength range due to reflection it will be bright enough only when illuminated by the sun. Figure 4.8 shows that the vast majority of trails are detected at low sun elevation, meaning close to the beginning and end of the night, with the observation cutoff for H.E.S.S. at -16°.

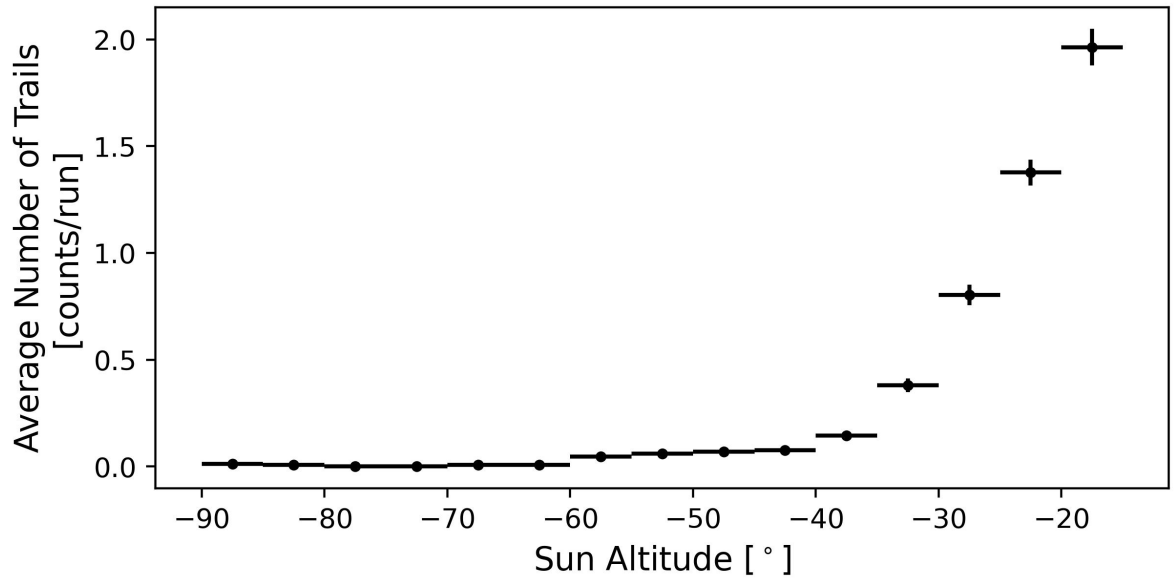

Figure 4.8: Trail detection rate as a function of the sun elevation

Once again the simplified approach by Hainaut and Williams [17] that will be discussed here is expanded upon by Bassa et al. [69]. Because of the geometry of Sun, Earth and the LEO satellites as seen in Figure 4.9 the satellite will reflect the sunlight until the sun has set for the satellite too. For this the sun elevation at the satellite's sunset needs to be calculated as a function of the h and Z. The solar phase angle can be ignored for LEO satellites, as is only affects satellites at altitudes larger than $h = R(\sqrt{2} - 1) = 2640\,\mathrm{km}$.

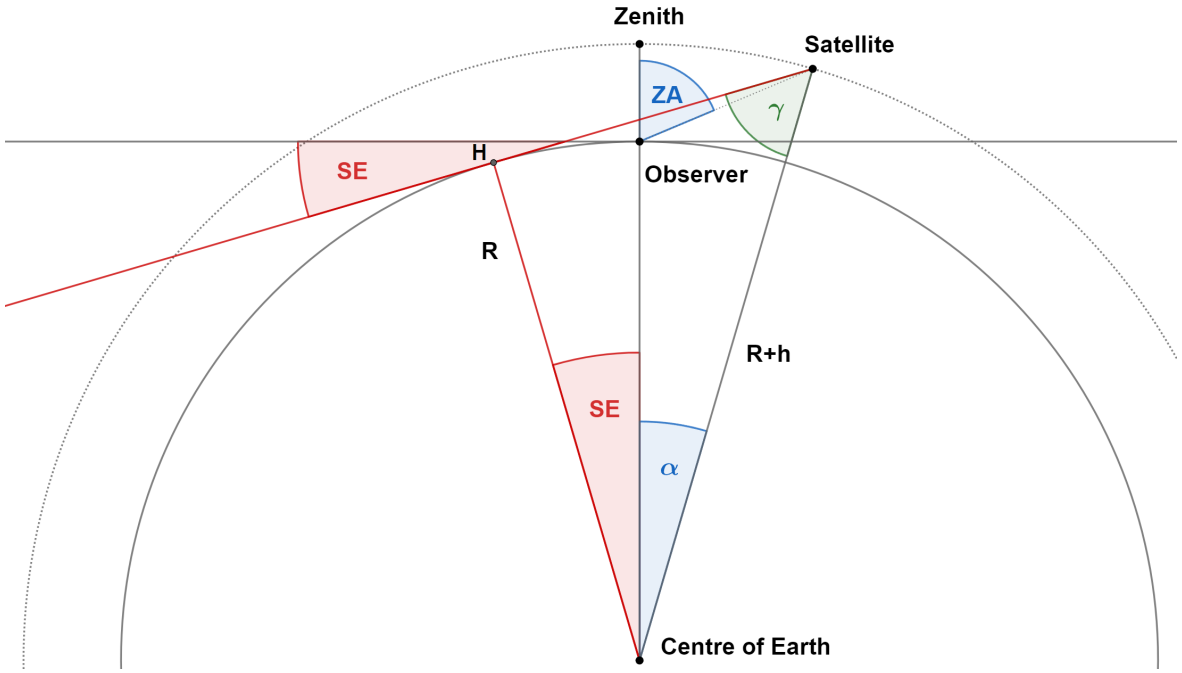

Figure 4.9: Geometry of the sunset for the satellite

In the limit the angle to the sun at the observatory is the same as the one at the satellite.

The point H is defined such that the satellite and the sun are on opposite sides of its horizon. Hence its position on the circle and its horizon can be achieved by a rotation of the observers position and horizon by the sun elevation angle, explaining, why $\sphericalangle ZCH = SE$. Together with the satellite and the Centre of the Earth H forms a right triangle, hence $\cos(\alpha + SE) = R/(R+h)$. The angle α at the centre of the earth has already been calculated in equation 4.6, therefore it follows that

$$\mathrm{SE} = \cos^{-1}\left(\frac{R}{R+h}\right) - Z + \sin^{-1}\left(\frac{R}{R+h} \cdot \sin(Z)\right). \tag{4.12}$$

It is important to note, that in the zenith angle in Equation 4.12 needs to be seen w.r.t. the direction of the sun setting. For instance as Z is depicted in Figure 4.9 is would need to be inserted as a negative value.

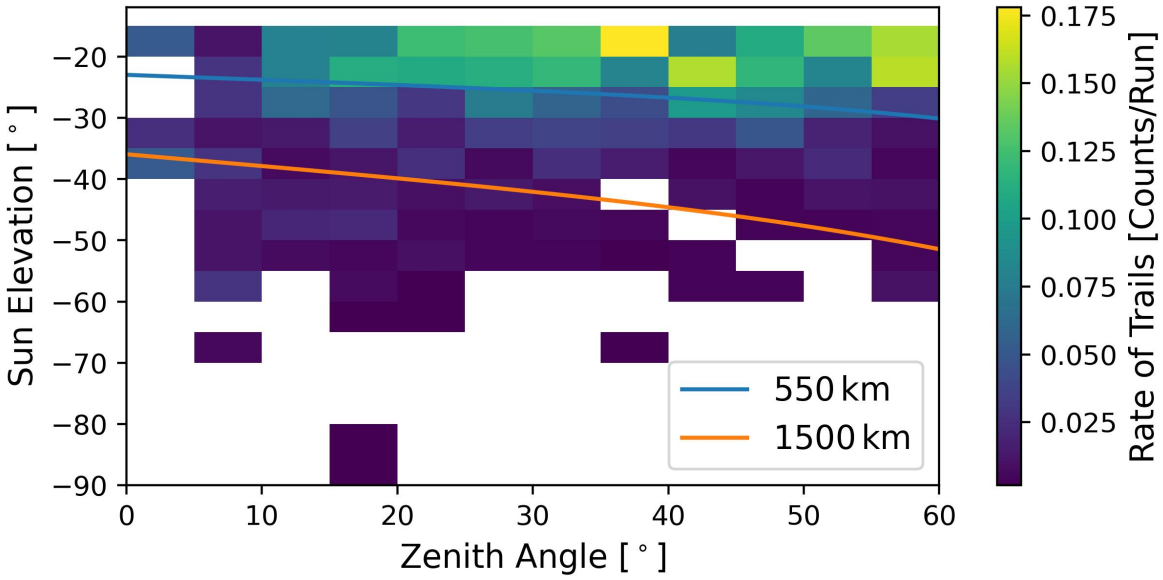

Figure 4.10: 2D-histogram of zenith and sun elevation angles

Figure 4.10 depicts the measured trail rates as a function of zenith angle and sun elevation together with the limits calculated for Starlink satellites as well as LEO satellites in general. The largest absolute sun elevation angle at which a LEO satellite would be illuminated by sunlight is -51°. Every entry below the 1500 km curve would therefore according to this geometrical approximation belong to non-LEO satellites. This also means that it is expected that those times and directional regions will not detect more satellites with the increasing number of LEO satellites. Figure 4.11 (a) and (b) show that both the velocity and the brightness of a trail are expected to decrease with the sun elevation. Some entries stand out as unusually bright or fast for the corresponding sun elevation, which is an indicator for a wrongly reconstructed trail.
The more precise analysis by Bassa et al. [69] includes the latitude effects and differences in expected trail numbers with the observational direction. A possibly necessary future mitigation for the still affected regions could then be mitigated by scheduling the observations to minimize the effect at the beginning and end of the nights.

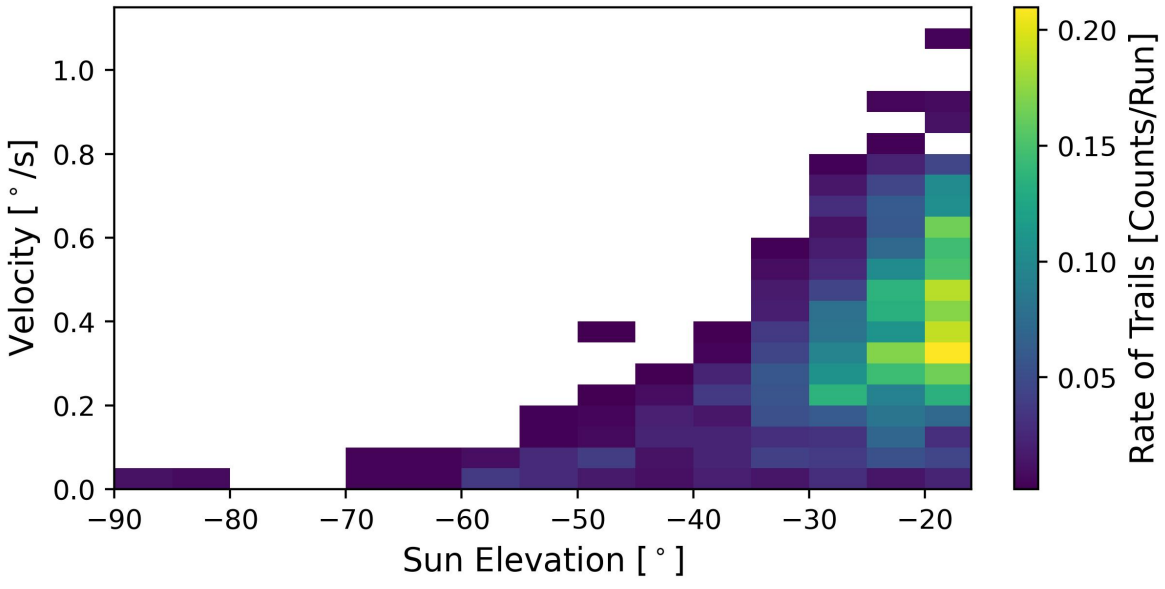

(a)

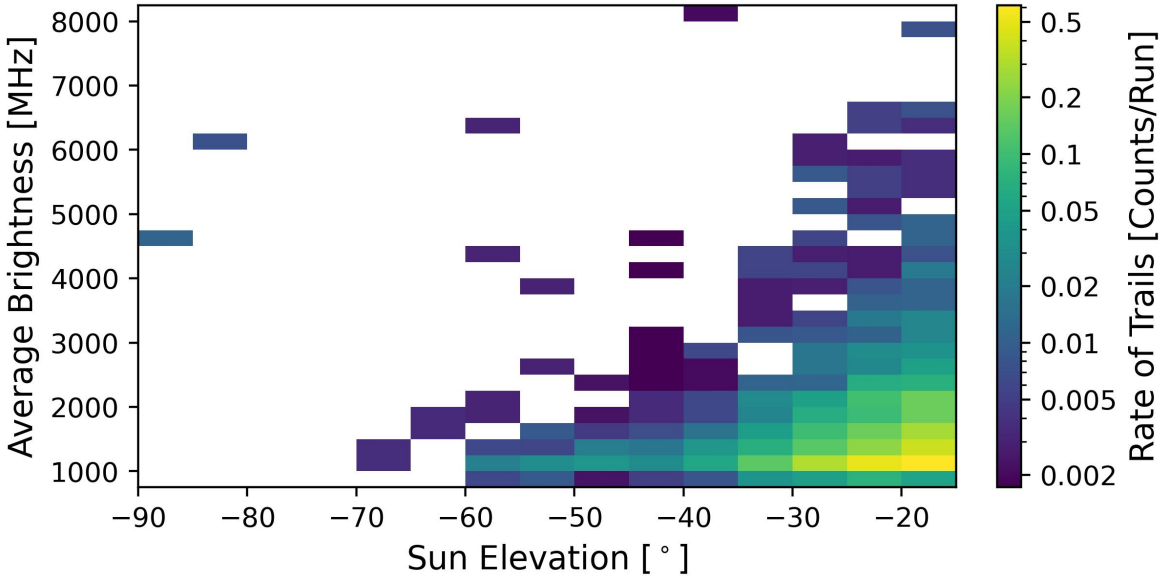

(b)

Figure 4.11: Trail velocities (a) and their average brightness (b) as a function of sun elevation

4.3 Detected Trail Rates

One major goal of this work was to find a correlation of the detected trails with the number of launched satellites. As a consequence predictions for future launches of satellites for H.E.S.S. and other IACTs like CTA could be inferred. The run selection has given 4715 suitable runs in time period from the 28th of October 2019 to the 2nd of February 2023. In that time a total of 1640 trails were produced by the trail finding algorithm, therefore giving an average of 0.35 trails per run over the entire three years and three months.
To get the time evolution of the average of trails per run that value is computed for every month in the investigated time period. A satellite detection is here assumed to be random, independent and constant over the time bin, hence the uncertainty of the number of detected trails estimated to be poissonian. With the known number of runs the error on the rate in a month then is given as $\sqrt{N_{\text{trails}}}/N_{\text{runs}}$. Precisely for the dependence on the number of runs the months of February 2020 and 2023 are excluded in the following analysis, since they would lead to unreasonably

high uncertainties. As previously mentioned the former only produced two runs, since most observed targets were on either η Car or the LMC. The latter has been excluded due to only two contributing observation days.

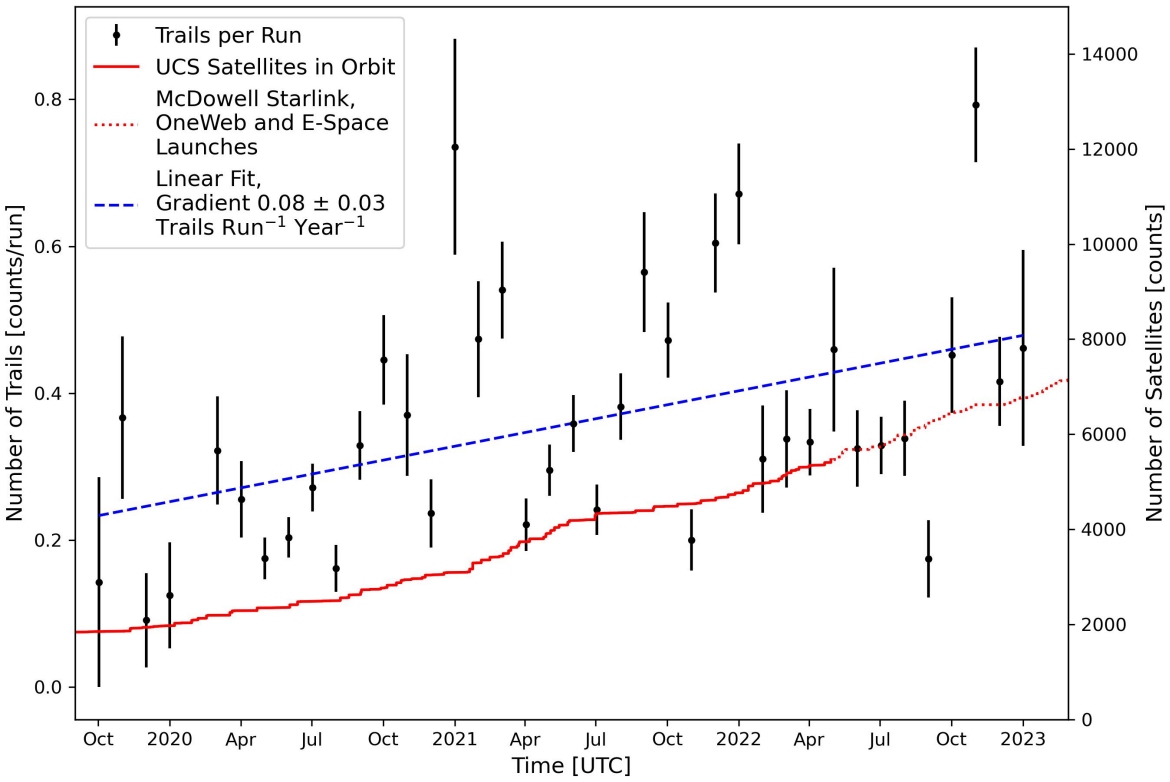

Figure 4.12: Average number of trails detected per month, with the errors assumed as Poissonian, Figure from [70]

Displayed in Figure 4.12 are the average trails per run per month and the number of satellites in orbit at each time. A linear fit to the trail data gives a increase of the trail rate of 0.08 ± 0.03 trails per run per year, equating to an approximate doubling of the trail rates over the investigated time period. The list by the UCS [2] used contains only launches up until the 1st of May 2022. For the remaining time period only the launches of the largest planned satellite constellations Starlink, OneWeb and E-Space as provided by Jonathan McDowell [3] were added, serving as a lower boundary for the total number of launched satellites. In the considered time period the number of satellites has almost quadrupled, which is why only a small correlation coefficient of 0.41 with the detected trails can be determined. A statistically significant increase in the trail rate in time periods following launches with a large number of satellite could not be seen. During the orbital increase period satellites from a single launch are closely together, forming especially bright appearing trains [17]. However the probability of seeing these events limited to only a small portion of the sky with the relatively small FOV of H.E.S.S. is low. Furthermore a noticeable decrease during the seasonal burning periods in Africa in the months from August to October [71] can not be registered.
Since the average trail duration of $\sim 11.5\,\mathrm{s}$ is small compared to the standard run duration of 28 min the fraction of observing time affected has been small, with the median over the observed time period being $\sim 0.2\,\%$ [70]. Figure 4.13 shows the fractions for each month with a linear fit to the data, which results in a small positive gradient of $0.062 \pm 0.019\,\%$ per year.
The increase of the satellite population has mostly occurred at LEO heights, therefore it is expected that the gradient of the trail rate and hence the correlation coefficient increases with lower absolute values of the sun elevation angle, as a satellites illuminated by the sun are sufficiently bright enough to be visible [69].

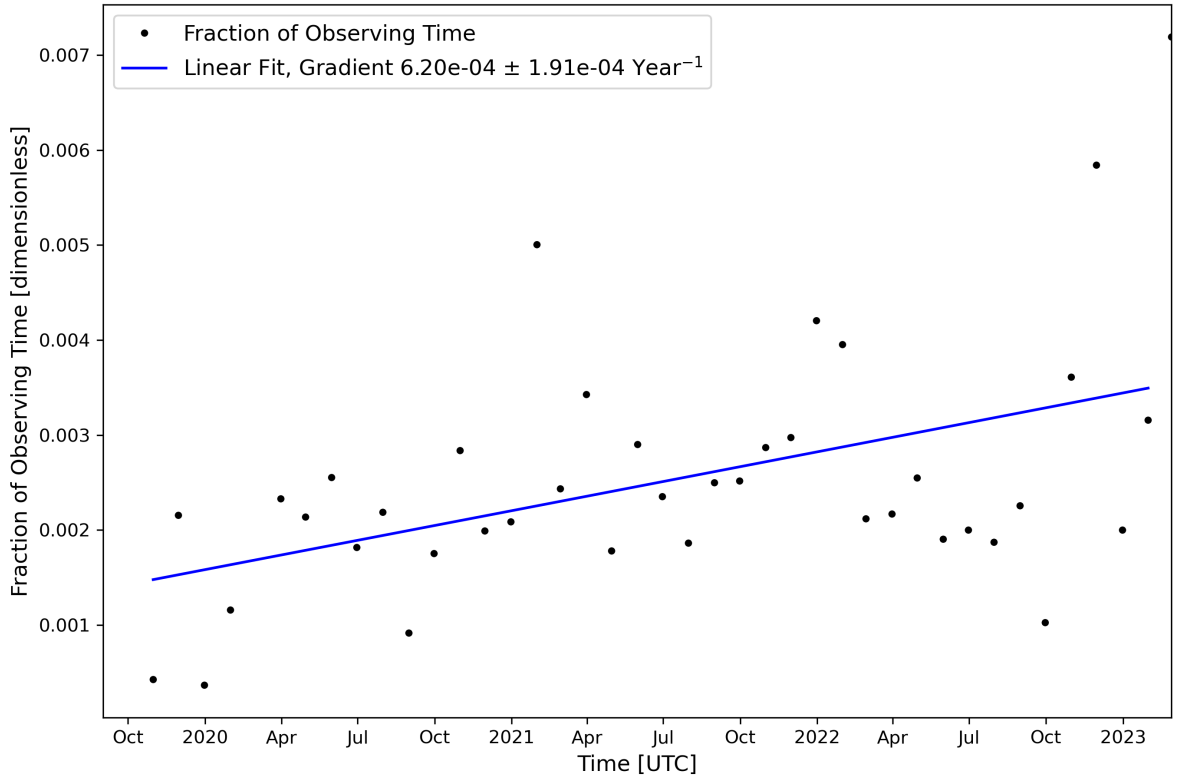

Figure 4.13: Linear fit to the fraction of observing time containing a satellite trail found by the trail detection algorithm used, figure by Dr. Samuel Spencer from [70]

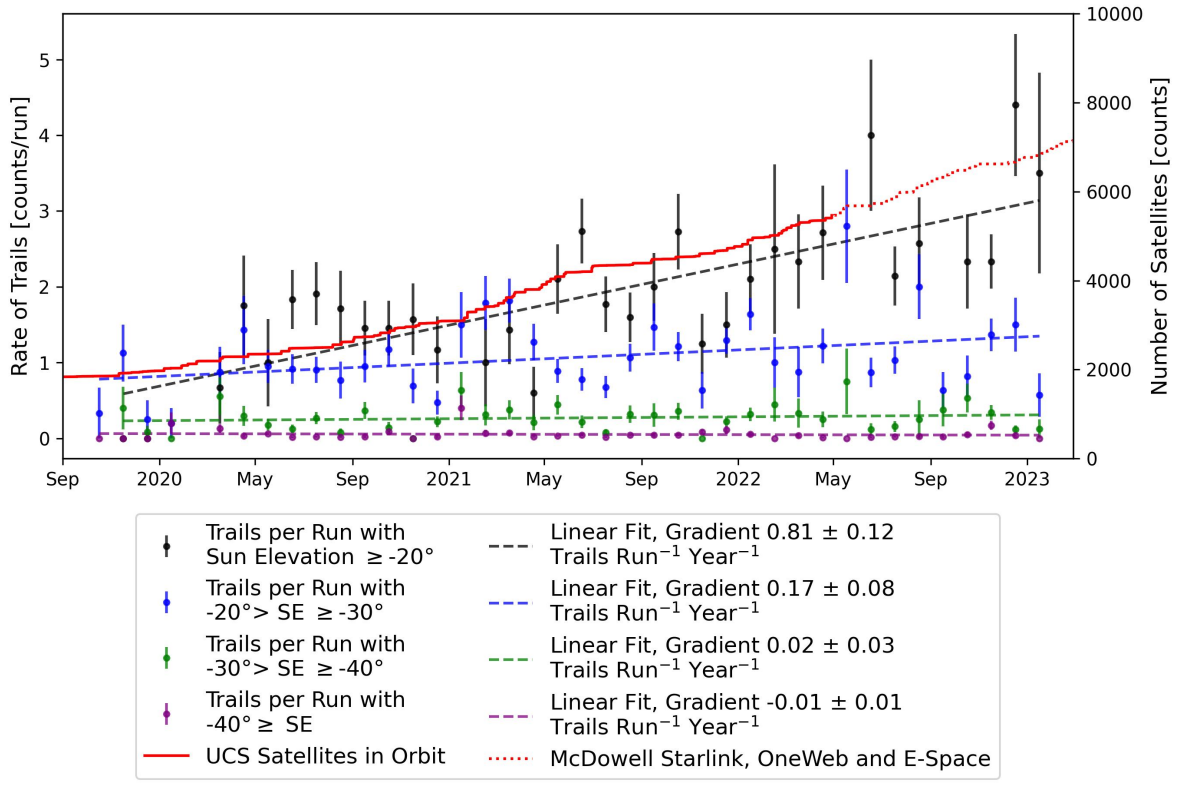

Figure 4.14: Comparison of the trail rate increase for different sun elevation angle ranges

Figure 4.14 displays the development of the registered trail rates for different sun elevation angle bins. The strongest correlation with the satellite launches with a coefficient of 0.76 is seen for $SE > -20°$. The relative slope in the range from $-30°$ to $-20°$ is lower than the

one shown in Figure 4.12, which results in a lower correlation coefficient of 0.29. It also shows that for $SE < -30°$ no increase in the trail rate over the inspected time period can be found. Consequently the conclusion can be drawn that the largest fraction of the night is unaffected by the recent increase in satellite launches.

4.4 Verification of Trail Detection Algorithm

A quick analysis of the observational properties of the runs in the run selection with respect to the detected trails will be discussed here, determining whether the trail detection shows biases.

4.4.1 Observational Properties

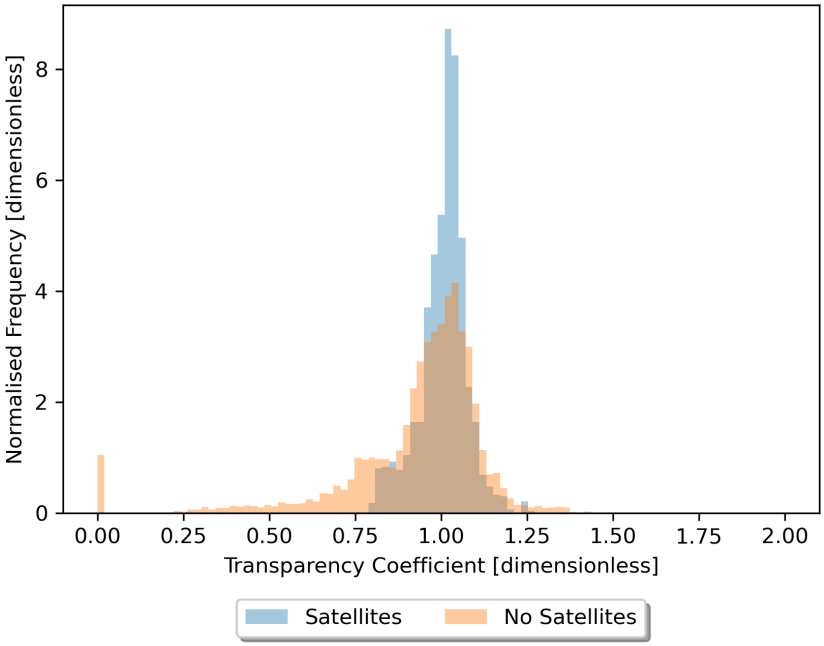

Figure 4.15: Effect of satellite trails on the reconstruction of the transparency coefficient, Figure provided by Dr. Samuel Spencer

The atmosphere will inevitably absorb a fraction of the produced Cherenkov photons before they can hit the PMTs. This absorption depends on the traversed air mass, as well as its transparency. The former is dependent on the zenith angle of the observation and can easily be corrected for. The latter is described by the Cherenkov transparency coefficient (see [71]). It assumes a stable rate of CRs and explains the zenith corrected variations in the trigger rates by different atmospheric conditions like clouds or aerosol concentrations. Finally the coefficient is scaled with a factor such that the distribution over the dataset of runs peaks at a value of one.
Figure 4.15 displays the normalized distributions both for runs containing at least one satellite and for runs without satellites. As shown by Hahn et al. [71] the second peak at ~ 0.75 can be explained by seasonal biomass burning in the months from August to October. At least in scale that peak is missing from the satellite distribution, with a possible explanation being that the higher absorption lets satellite trails appear dimmer than the 900 MHz cut. However a seasonal variation could not be inferred from Figure 4.12 as the statistical fluctuations due to the relatively small number of trails per month are to large.

Since bright satellite trails increase the NSB level it is expected that the pedestal NSB value is also increased in runs containing a satellite trail. Indeed this can be seen in Figure 4.16 (a), however compared to the "No Satellite" distribution a notable lack of runs with a pedestal value >600 MHz is visible. The higher overall NSB level in those runs has most likely led to an excessive number of pixels remaining above the 900 MHz threshold for an extended duration, making a reconstruction of potential trails in the dataset impossible.

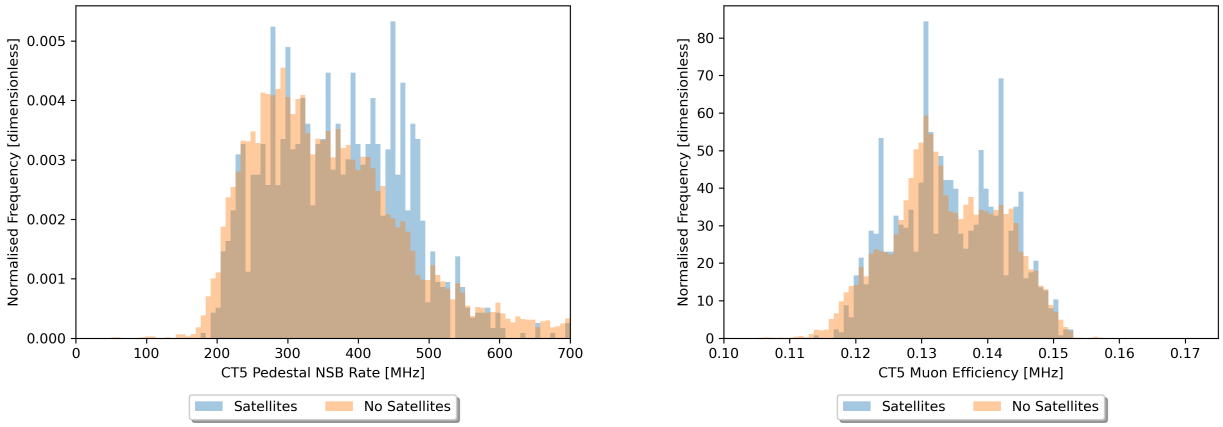

(a) (b)

Figure 4.16: Comparisons of pedestal rates (a) and muon efficiencies (b) for satellite and no satellite trail containing runs, Figures provided by Dr. Samuel Spencer.

It should be mentioned that variations in the trigger rate and consequently the Cherenkov transparency coefficient are also dependent on the so called "muon efficiency". Calculated by the fraction of measured to theoretical number of photons in muon rings the photon detection rate can be determined [72]. It is an important observational property for IACTs and is determined for each run and telescope, but since it goes beyond the scope of this work it is just mentioned briefly here. As can be seen in Figure 4.16 (b) no correlation between the muon efficiency and the detection of a satellite trail has been found.

4.4.2 Affected Night Sky regions

Figure 4.17 shows the distribution of the trail detection rates across the night sky in a Mollweide projection with a 5° binning. For this the mean Right Ascension and Declination for each run in the run selection were obtained from the database and converted into galactic coordinates. The registered rates >1.2 counts/run in a bin occur due to the low number of runs ($\lessapprox 10$) in that bin. No observational directions can be determined, that show a particular area of high or low trail rates, hence it can be reasonably concluded that the galactic and extra galactic regions are affected similarly by satellite trails.

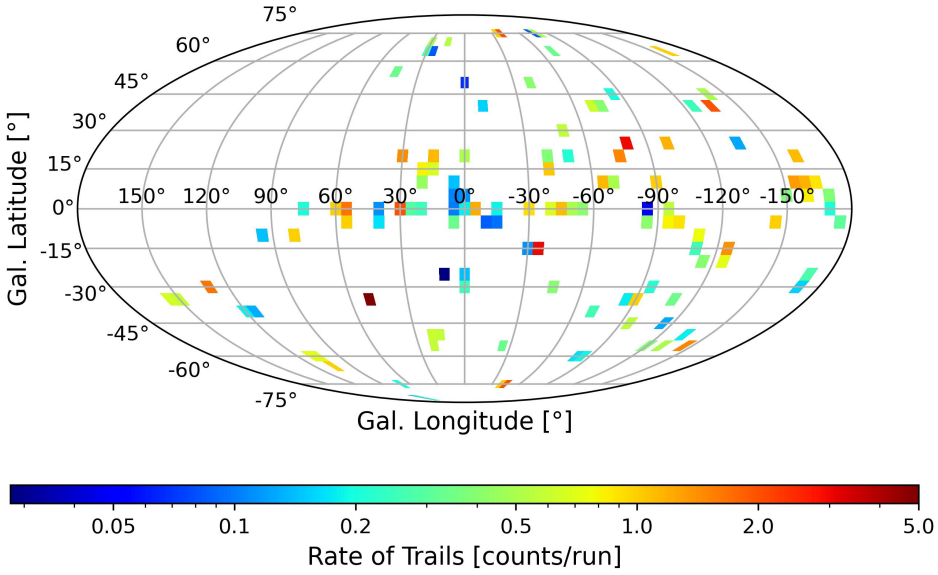

Figure 4.17: Rate of detected trails for galactic longitude and latitude

4.5 Misreconstructed Trails

A quick analysis of the quality of the produced trails will be discussed here. Checking every single of the 1640 trails manually is not a viable solution, therefore by analysing the various saved trail properties deviations from the trend might indicate a misreconstructed trail. This however does not invalidate the findings presented in this work, as those trails make up less than 2 % of all trails. Misconstruction typically affects the length, width, velocityies and total duration of a trail, only a fraction of those are actually not caused by a satellite.

4.5.1 Trail Width and Brightness

The plot in Figure 4.20 shows that correlation as well as the number of unique pixels affected as the color scaling.
Here the average width W is defined as the average number of pixels per pixel length and is therefore calculated as:

$$W = \frac{N_{\text{pix}}}{L} \cdot \frac{1}{0.08°}, \tag{4.13}$$

with the number of unique pixels affected by the satellite trail N_{pix} and the trail length L in degrees. The angular sizes of satellites are smaller than the FOV a single Flashcam pixel, hence the assumption that only a single pixel is affected at any given time [19] seems to be reasonable at first. However it has been found that the trail width of the detected trails can be several pixels wide.
Exemplary shown in Figure 4.18 (a) and (b) are the brightness of the thinnest and widest legitimate trails, with calculated widths of 0.4 and 7.0 pixels respectively. From this it becomes clear that satellites affect the NSB of several pixels at the same time and keeping the 900 MHz brightness threshold in mind the affected area is likely larger, even for the dimmer trails. Hence the determined trail width only gives a lower limit estimate on the pixel diameter of the area contaminated. The broadening of the theoretical point-like satellite reflection is likely caused by

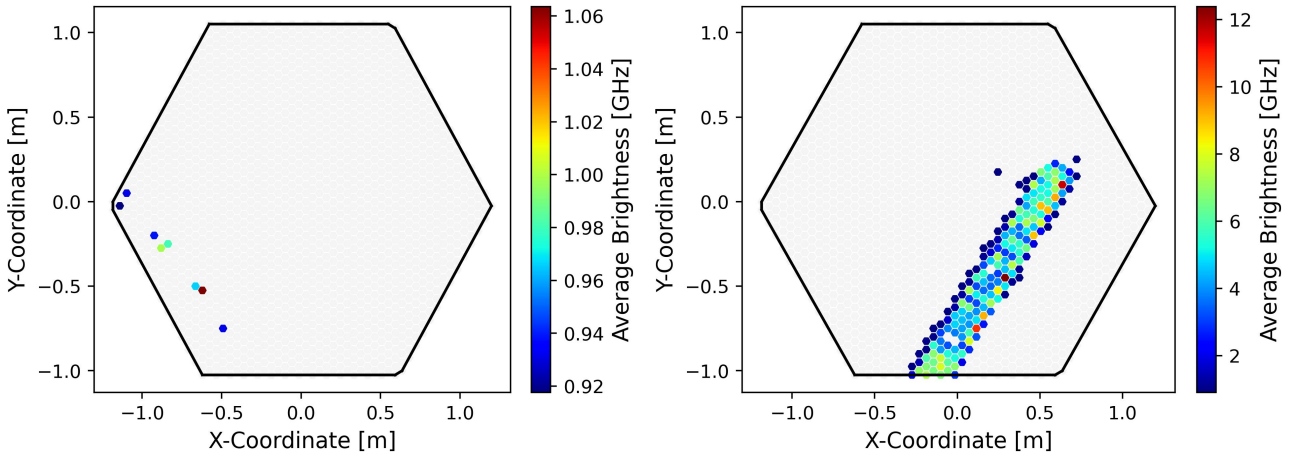

(a) (b)

Figure 4.18: The average brightness of the (a) thinnest and (b) widest legitimate trails, registered in run numbers 172440 and 175965 respectively.

atmospheric scattering.

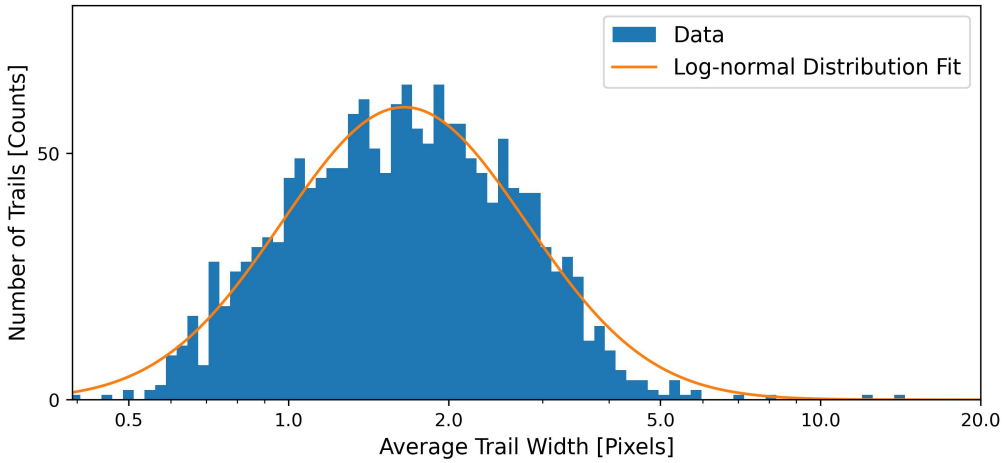

Figure 4.19: Average trail width distribution with a log-normal distribution fit with a mode of 1.65 ± 0.07. The fit parameters are displayed in Table 4.1

Parameter	A	μ	σ	Mode
Fit value	149.3 ± 0.03	0.779 ± 0.029	0.529 ± 0.029	1.65 ± 0.07

Table 4.1: Fit parameter to the log-normal width distribution

The trail width distribution displayed in Figure 4.19 roughly follows a log-normal distribution centered around 1.65 ± 0.12 pixels. This is notably much larger than the optical PSF of $\sim 0.022°$ for CT5 [70]. All but the shown wider trail with a width larger than 6 pixels are misreconstructed in some way (see section 4.5.2).
It is expected that the average and maximum trail brightness are correlated. Figure 4.20 shows that correlation, together with the trail width as a color scaling. The maximum brightness in a trail hits a cap of ~ 17000 MHz due to the maximum of the detectable NSB level in a single event. Since the saved NSB value is averaged over a 0.1 s time window that maximum shows a slight

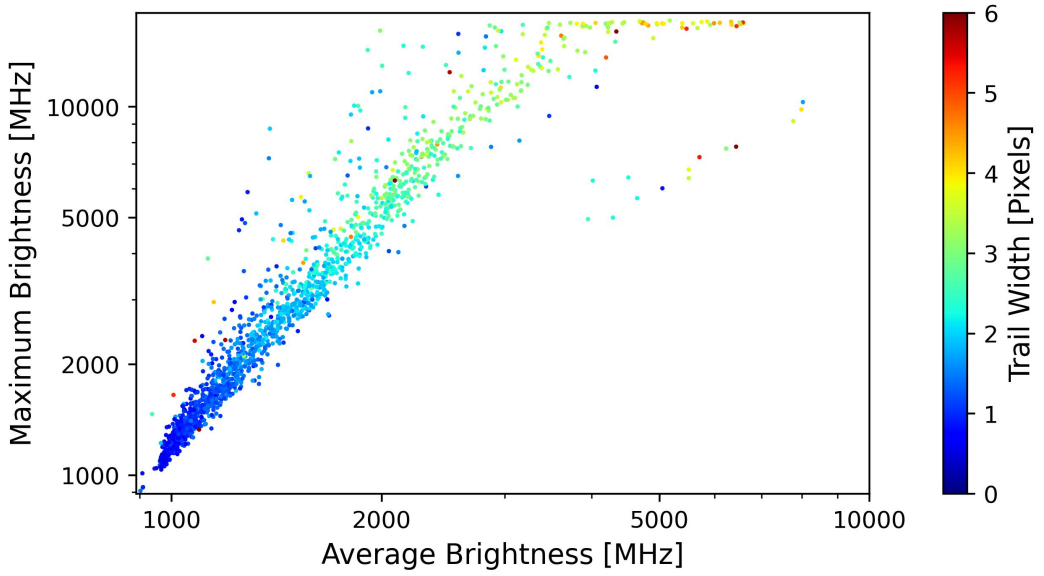

Figure 4.20: Correlation of average and maximum brightness with the trail width as the color scaling

variability. Most notable however are the entries with a large average brightness that deviate strongly from the remaining data. Those 14 trails are actually just a bunching of randomly bright pixels, two examples of those are shown in Figure 4.23. A future evaluation should reject those false trails by introducing further cuts on the trail brightness and replacing the currently used unique pixel cut by a width cut.

4.5.2 Misreconstruction Types

This section focuses on the different possibilities of wrongly reconstructed trails and a brief mention of how a future analysis might remove them.

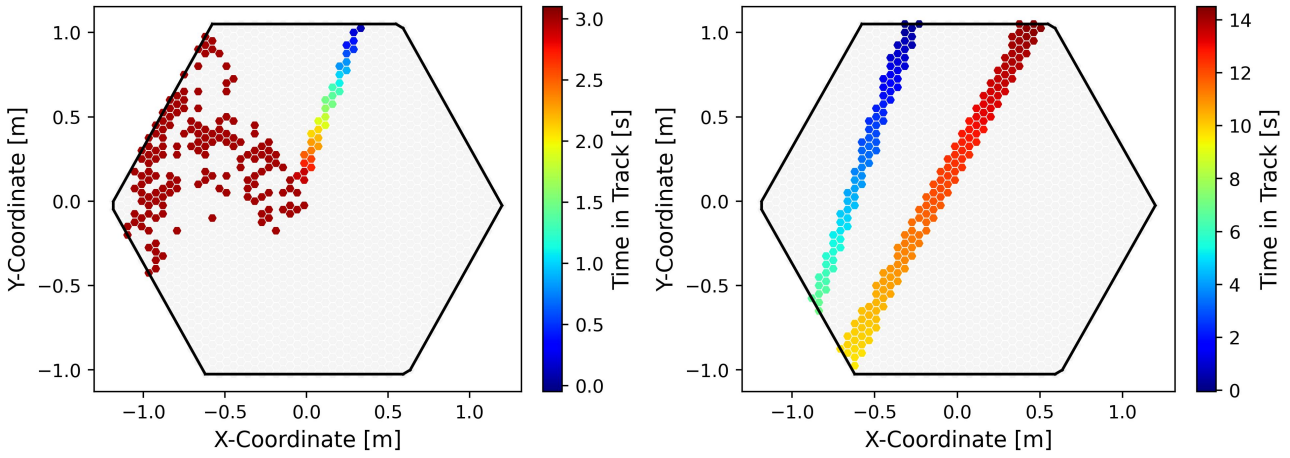

(a) (b)

Figure 4.21: (a): Camera flares occurring at the same time as satellite crossing interrupts the trail. This one was barely registered in run number 166073 as a trail and has an impact on the calculation of the velocity and number of affected pixels. Impact could theoretically be reduced, if it is checked, whether the last entry in a trail has way too many entries for a single timestamp (b): One instance of two trails being added together, found in run number 179366 due to its extremely large calculated width

Figure 4.21 (a) shows a potential hardware issue with the CT5 camera, in which a large section of the camera briefly flares up at the same time. The trail sorting algorithm mistakes those

flares as continuations of the satellite trails, often leading to an interruption of the trail, as the continuation of the actual satellite trail is outside the neighbourhood of the last entries of the camera flare. This leads to a distortion of the various trail properties The trail shown barely passes the 3 s threshold to be considered as one, this indicates that the number of tracks in the dataset is likely under counted. Wide trails are more susceptible to additions of these flares or randomly bright pixels in general, as the number of pixels, whose neighbourhoods are considered, is larger In a further iteration of the track finding algorithm flares can be excluded by adding a further cut on the NSB dataset. By eliminating timings which have a number of unique pixels exceeding a threshold that needs to be determined those camera flares can be accounted for.
Figure 4.21 (b) displays a case, in which two bright satellites are crossing directly over each other in opposite directions in the near vicinity of the FOV of CT5, so that the track sorting algorithm assumes the second trail is the continuation of the first one. The conditions necessary for that case are very unlikely, only being registered a single time during the investigated time period, hence this misreconstruction type is not affecting the general trends found in this work. The probability of it will increase with the number of satellites in orbit, and measures to find and prevent these will be necessary. This track has been found as it is the one with the by far largest calculated width. A future work can further reduce the probability of this event occurring by reducing the size of the neighbourhood region of each pixel.

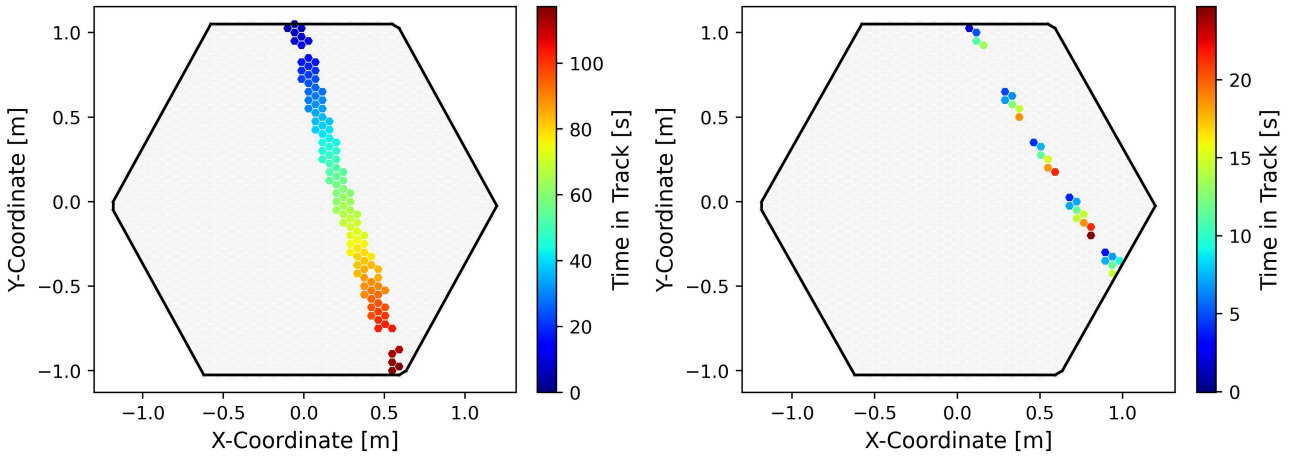

(a) (b)

Figure 4.22: Comparison of a properly (a) and a fragmented (b) reconstruction of a slow trail, both registered during the same run number 159552. First part of (b) was rejected as a potential trail, since it did not meet the six pixel minimum.

Another potential issue can be seen in Figure 4.22, which compares two slow trails of the same run, where the average brightness of (a) is ∼1800 MHz and the one of (b) is ∼1150 MHz. shows the slowest detected satellite trail. The dimmer satellite was registered as five separate potential trails with an average velocity of 0.018°/ s. The first one was rejected as a trail as it does not pass the minimum of six unique pixels condition, while the remaining four were counted as individual trails. At this velocity a satellite takes ~ 4.5 s to cross the FOV of 0.08° of a single pixel, meaning that a two pixel gap caused by bright stars or insufficiently illuminated pixels is enough to interrupt the proper trail construction. In order to not over count a single trail velocities above $N \cdot 0.016\,°/\mathrm{s}$ are needed to cross gaps of N pixels within the 5 s time proximity condition of the track sorter.
A briefly explored but yet to be implemented solution for this problem has been the addition of tracks if certain angular and temporal conditions are met. Since this problem practically occurs only for the slowest trails with brightnesses close to the 900 MHz threshold, the impact of this

over counting is estimated to be very small.

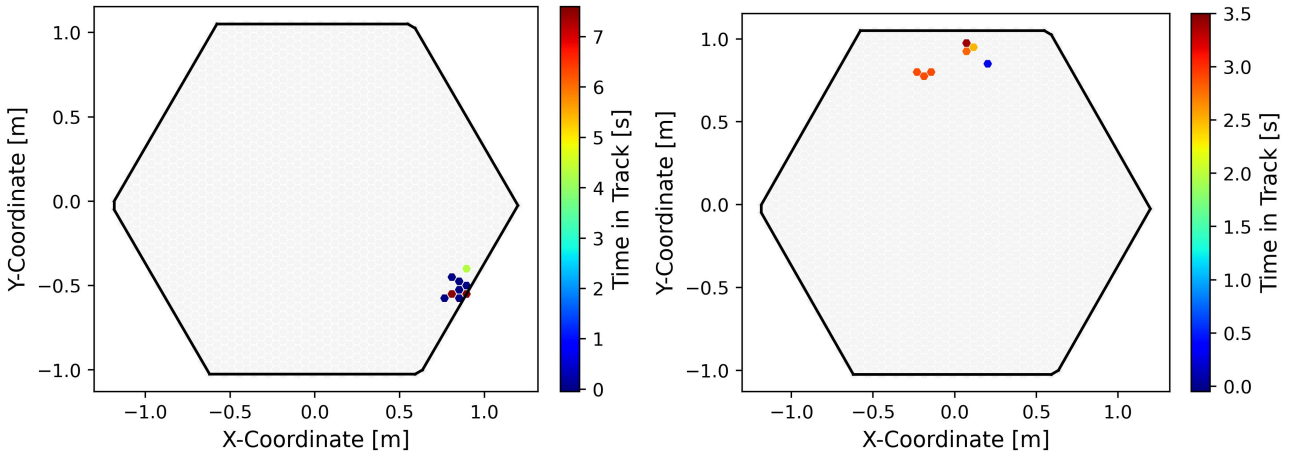

Figure 4.23: Two examples of false trails, found in run numbers 167485 and 172629 due to their length being too small.

The length of a trail can be an indicator for it being a faulty one, particularly if it is too short. Limiting the trails to six affected unique pixels and above inherently gives a minimum length for a legitimate trail, which considering that a real trail is never a cluster is a length of at least 3 pixel widths. This corresponds to the calculated pixel length of 0.16°, as the length is calculated by taking the centre position of a pixel as opposed to the pixel edges. Figure 4.23 shows two examples of these false trails: The right one is caused by the already discussed camera flare occurring close to a single pixel, which is bright ($> 3000\,\mathrm{MHz}$) for an extended period of time ($10\,\mathrm{s} > t > 1\,\mathrm{s}$). These can be prevented by the already mentioned camera flare removal. The second one is an accumulation of single pixels independently being just above the brightness threshold for a short time. Larger clusters of these random pixels mistaken as trails are prevented by the average timing difference of 0.3 s.
The number of spurious trails composed entirely of non-trail pixels is < 10, but with the removal of the camera flares and cuts on the minimum possible length as well as the above described width and brightness cuts can prevent them in a future iteration of the algorithm.

Chapter 5

Impact on Event Reconstruction

In this chapter the focus shifts from the trail properties towards their impact on Hillas parameters which historically were used to reconstruct events. The method to compare the events registered during regular measurements and those contaminated by satellites will be presented.

5.1 ON-OFF Regions

In order to quantify the effect a satellite transit has on the reconstruction parameters a reference needs to be taken. This is done here by a method similar to the on-off observation mode of IACTs to discriminate for the background: The ON time region is defined by the first and last time entry of each satellite. The OFF time has the same total duration as the ON time to allow for a proper comparison, but in the standard case is split into two parts of equal duration. To account for the larger FOV of CT1-4 and to retain similar observation conditions a time difference of 60 s to the trail start and stop times was chosen in order to not be potentially contaminated by trail events.

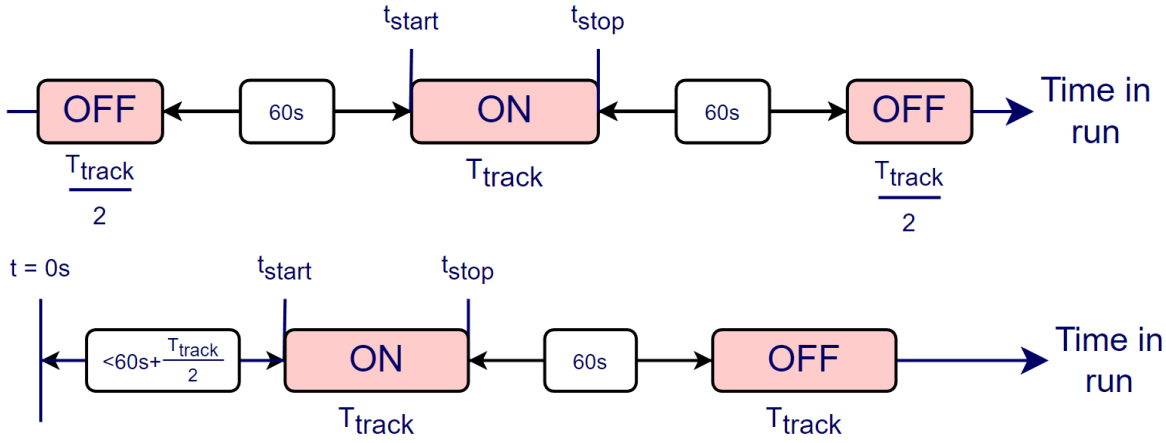

Figure 5.1: Illustration of the "On" and "Off" timings for satellites being on or off the camera. A separation in time by 60 s was chosen to account for any possible interference, as well as the larger FOV of CT1-CT4. Whenever possible, the "Off" timing consists of two time windows as illustrated above, each taking half the duration of T_{track}.

Figure 5.1 shows a schematic for this standard case as well as the case for a trail being detected close to the beginning of the run. If the time difference between the start of the trail and the start of the run was too small to ensure that the first OFF part can be taken in its entirety, the OFF part consists of only one part of equal duration to the ON part. Not illustrated here, but also accounted for, is the case of trails being too close to the end of the run. The method

described here is used to produce the "Satellite" and "No Satellite" histograms in the following section.

5.2 Impact on Hillas Parameters

In this work only the effect on the Hillas parameters is investigated. The Image Pixel-wise fit for Atmospheric Cherenkov Telescopes (ImPACT) method used by *HAP* is seeded by values obtained by Hillas reconstructions [60]. Therefore it is likely that Hillas parameters influenced by false triggers are affecting the ImPACT analysis as well. The analysed Hillas parameter datasets, provided by Dr. Samuel Spencer, were obtained using the *Hillas0510* tailcut cleaning, meaning the "boundary" and "bright" thresholds are set to be at 5 p.e. and 10 p.e. respectively. Since the hardware of CT1-4 is identical only the distribution of the Hillas parameters of CT1 will be shown as an example for the four telescopes.
Further a differentiation is made between bright and dim average trail brightnesses. 3000 MHz was chosen as a threshold, since the majority of effects become noticeable above that value. 99 of the 1640 trails make up the distributions of the bright trails. The ON and OFF events are each taken over a time period of 5.16 h and 0.21 h for the dim and bright trails respectively.

Parameter	Cut Values
CT1-4 Hillas Amplitude	(60, 1000000) p.e
CT5 Hillas Amplitude	(80, 1000000) p.e.
CT1-4 Local Distance	(0,0.525) m
CT5 Local Distance	(0,0.72) m

Table 5.1: Cuts employed by the high level *HAP* hybrid standard analysis

5.2.1 Hillas Amplitude

The most important parameter to determine the energy of the primary particle is the Hillas amplitude. Figures 5.2 and 5.3 show the different distributions for the telescopes for the dim and bright trails.

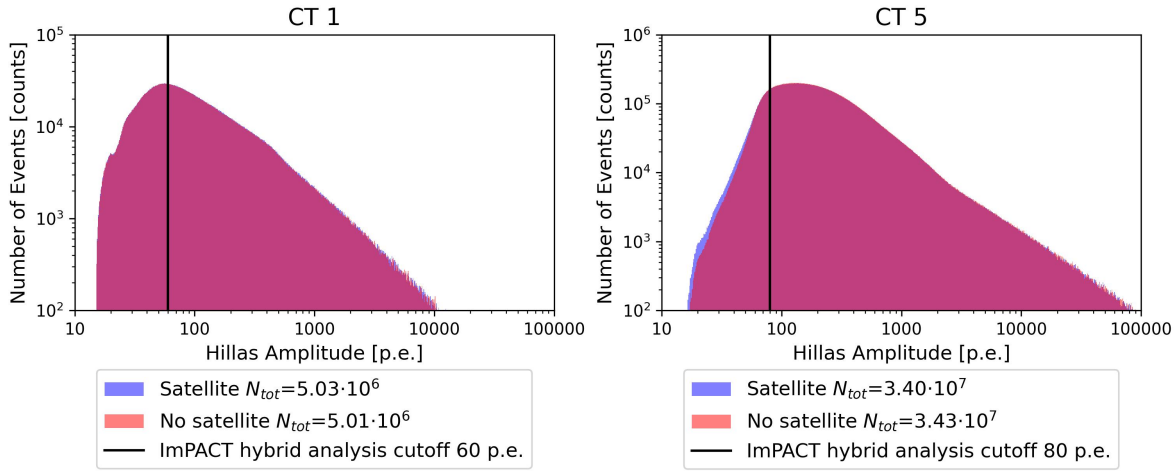

Figure 5.2: Hillas Amplitude Average trail brightness under 3000 MHz

The total number of events for the "Satellite" and "No Satellite" distributions are comparable in both telescope types for the dim trails, however a small increase in low amplitude events for CT5

can be registered. Bright satellites produce distributions with an overall reduction in the number of registered events by 16.8% for CT1 and by 28.9% for CT5. Furthermore the fraction of low amplitude events in CT5 is increased forming a noticeable second peak at ~ 50 p.e. Those events are likely false triggers induced solely by the trail brightness. But the vast majority of them fall below the high level *HAP* hybrid standard analysis cutoff (see Table 5.1). The main impact a satellite trail has on the Hillas amplitude distribution for standard astronomical observations is a reduction of the event rate. Observations like those of GRBs [73] that use looser cut on the other hand likely contain false trigger events in their analyses. The percentage of contaminated data will be small, as only $\sim 5\%$ of detected trails are bright enough to produce false triggers in the first place and the fraction of observing time containing a satellite (see Figure 4.13) has been low as well.

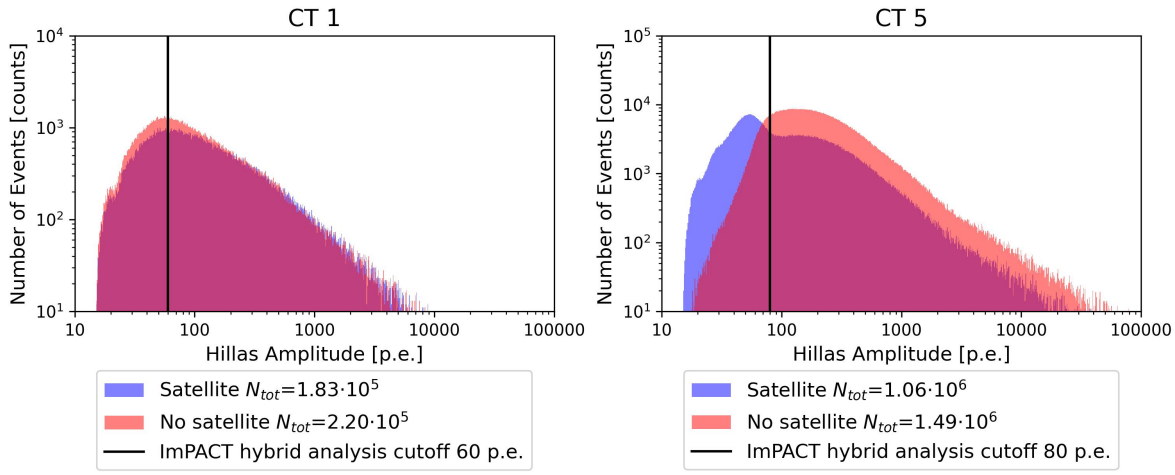

Figure 5.3: Hillas Amplitude Average trail brightness over 3000 MHz

5.2.2 Hillas Length and Width

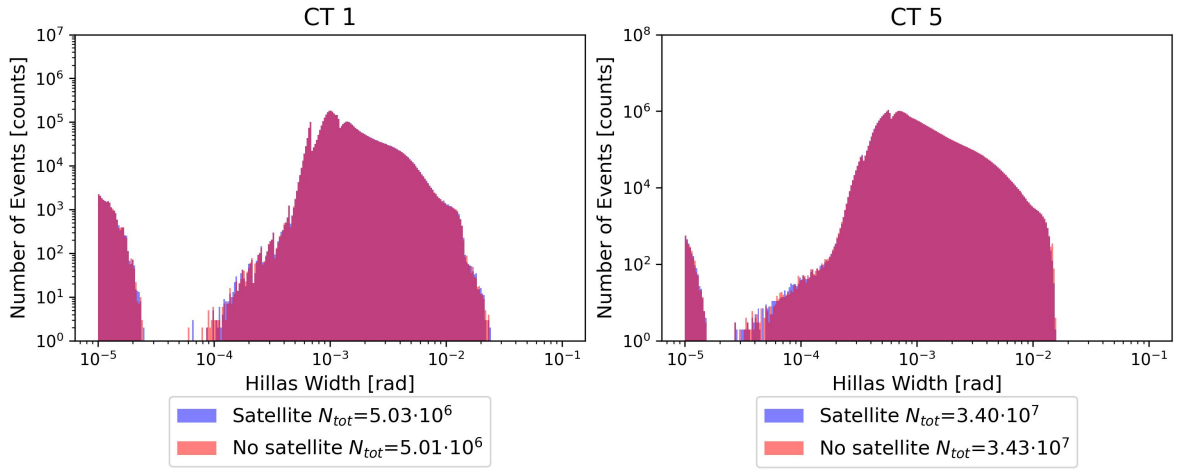

Figure 5.4: Hillas Widths for average trail brightness under 3000 MHz

The Hillas length and width describe the major and minor axis of the elliptical shower image on the camera. Both their distributions for both telescope types for the transit of dim satellite trails, shown in Figures 5.4 and 5.5, are almost unaffected.
The Hillas width distributions notably have a non-negligible fraction of events with very low values. These events are registered at the camera edges and hence are truncated, leading to the

too small Hillas widths. They can be removed in higher level analyses by the use of a Local Distance cut like the ones presented in Table 5.1.

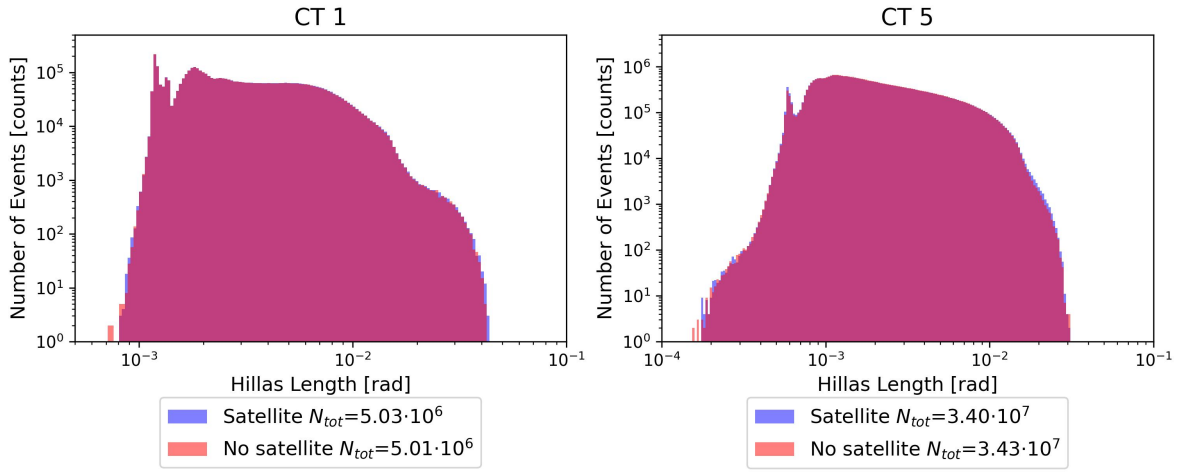

Figure 5.5: Hillas Length for average trail brightnesses under 3000 MHz

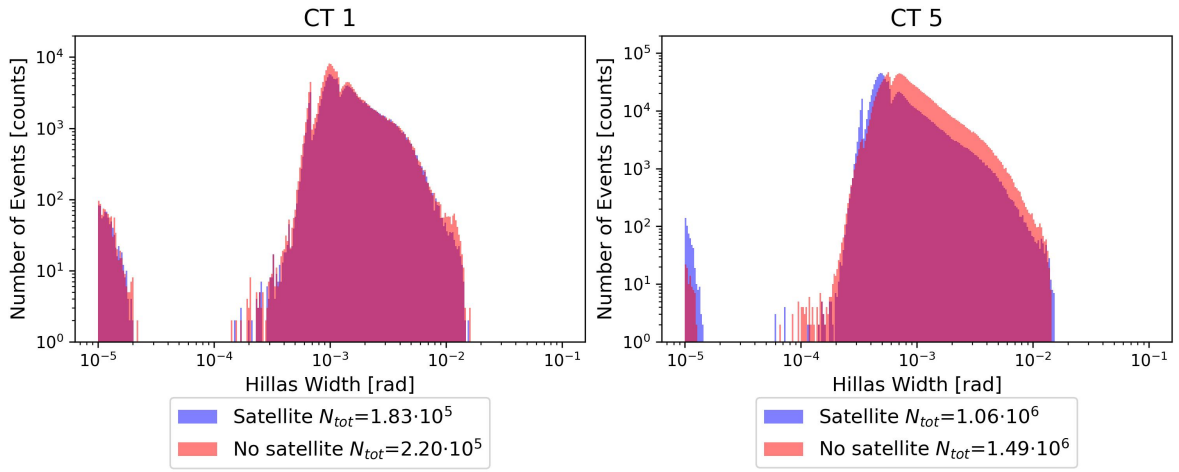

Figure 5.6: Hillas Width for average trail brightnesses over 3000 MHz

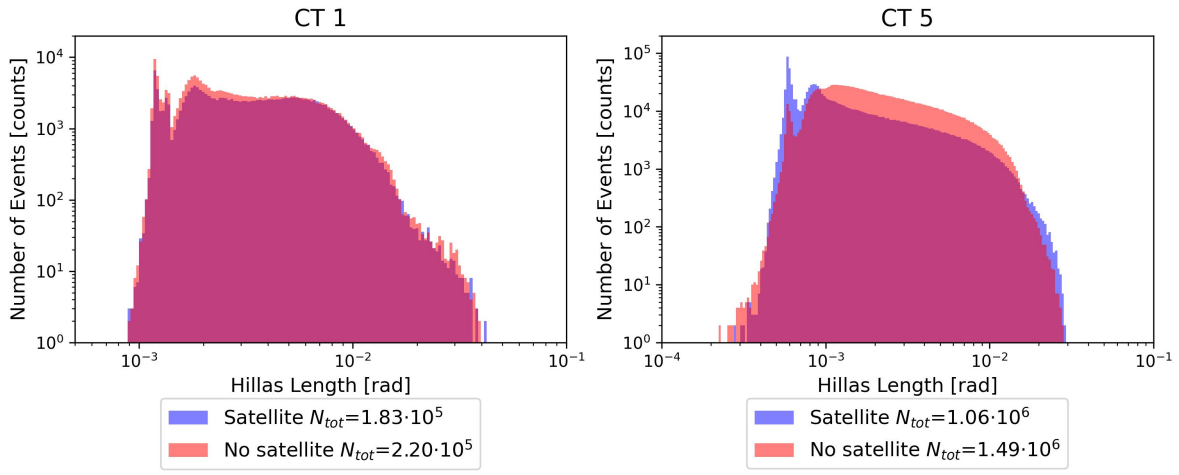

Figure 5.7: Hillas Length for average trail brightnesses under 3000 MHz

Figures 5.6 and 5.7 show the effect of bright satellites on the Hillas width and length respectively, and the effect is different between CT1-4 and CT5. The reduction of the event rate in CT1

appears to be confined to the upper and lower ends of the distributions of both parameters. Meanwhile, looking at the Hillas width distribution of CT5 in Figure 5.6, it seems like the fraction of truncated events increases significantly and the three small peaks of the distribution get accentuated. Similarly, the two peaks in the CT5 Hillas length distribution in Figure 5.7 are much more pronounced. It also appears like the probability of an event being particularly long is increased.

5.2.3 Hillas Alphas and Phis

The Hillas alpha and phi parameters are used for the directional reconstruction of the primary particle. For both parameters and all telescopes the distributions of the dim satellite trails are virtually indistinguishable from the ones with no satellites, which is why they are not presented here.

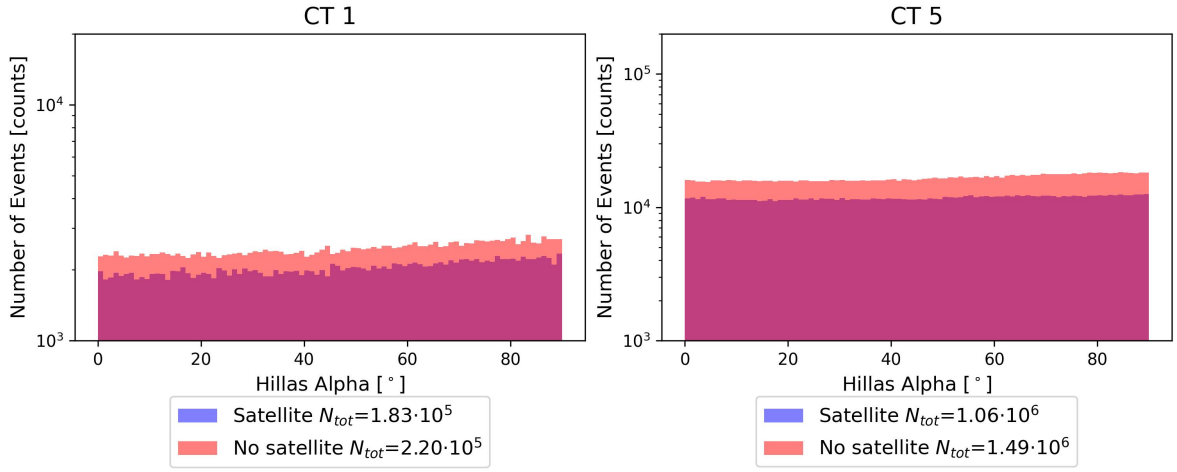

Figure 5.8: Hillas alpha distribution for average trail brightnesses over 3000 MHz

For the bright distributions of the Hillas alphas in Figure 5.8 only the reduction in the event rates can be seen.

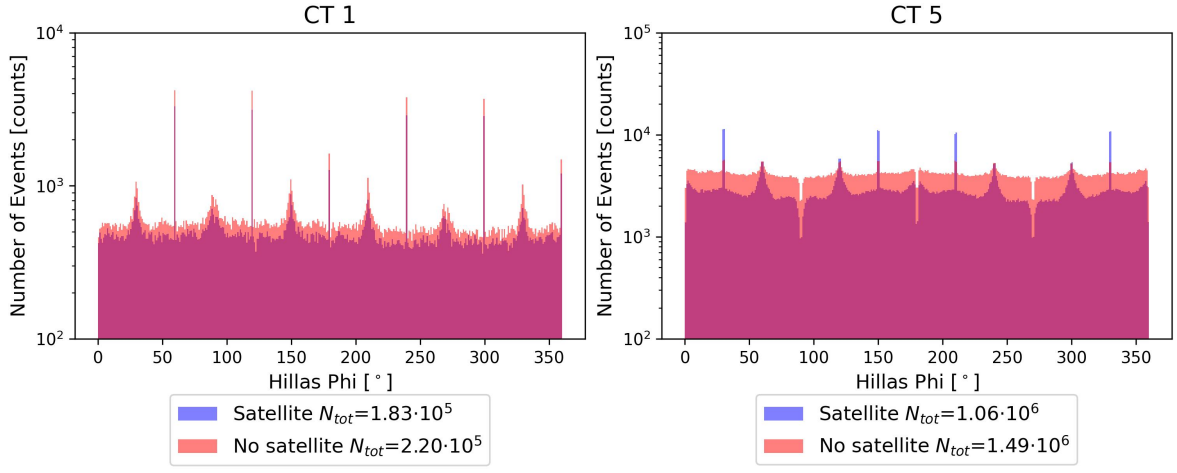

Figure 5.9: Hillas Phi average trail brightness over 3000 MHz

For CT5 the distribution of the Hillas phis exhibits a sharp excess for the angles 30, 150, 210 and 330 degrees, a broader increase around 0, 60, 120, 240 and 300 degrees and a sharp deficit for 90, 180 and 270 degrees. This is explained by the hexagonal camera geometry favouring or disfavouring certain phi angles over others. These deviations are accentuated for the satellite

distributions. Interestingly this is not seen for CT1-4, even though their camera geometry favours the same angles.

5.2.4 Hillas Skewness and Kurtosis

The Hillas skewness and Hillas kurtosis are two additional Hillas parameters that have not been mentioned before. They are the third and fourth statistical moments of the shower intensity distribution respectively and can be used to further discriminate EAS images. The skewness characterizes the asymmetry of the intensity distribution, while the kurtosis characterizes the "tailedness". A higher kurtosis means that the values are clustered around the mean with more extreme values in the dataset, while a lower kurtosis has fewer extreme values and a less pronounced peak. Here the excess kurtosis will be displayed to show the deviation from a normal distribution, which has a Kurtosis value of 3. γ-ray events tend to produce contained, symmetrical images, i.e. a low skewness with high kurtosis while CR events are more extended over the camera.

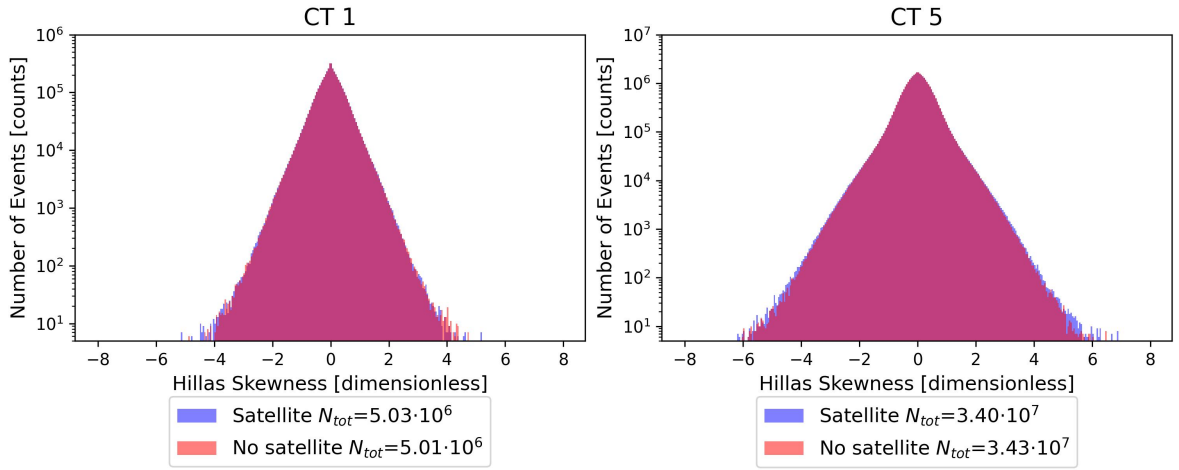

(a)

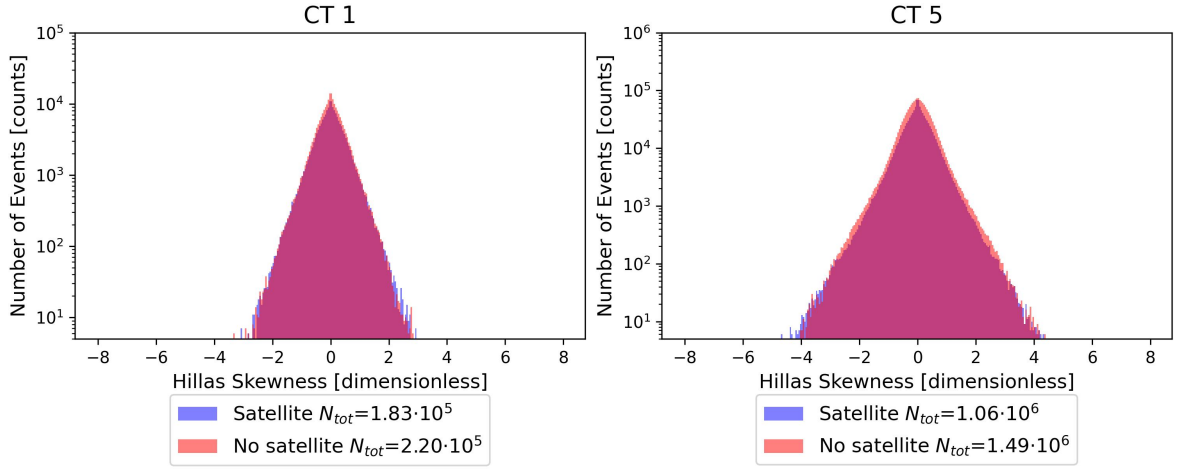

(b)

Figure 5.10: Hillas skewness for trails with an average brightness under (a) and over (b) 3000 MHz

The skewness distributions of dim satellite trails shown in Figure 5.10 (a) exhibit a marginal excess for large absolute values for both telescope types, with CT5 events being slightly more affected. Considering the reduced event rate, that effect is more pronounced for the bright satellite distributions in Figure 5.10 (b). Also an excess for a skewness of zero can be seen as well. The former excess indicates that pixels affected by satellite brightness are included in a

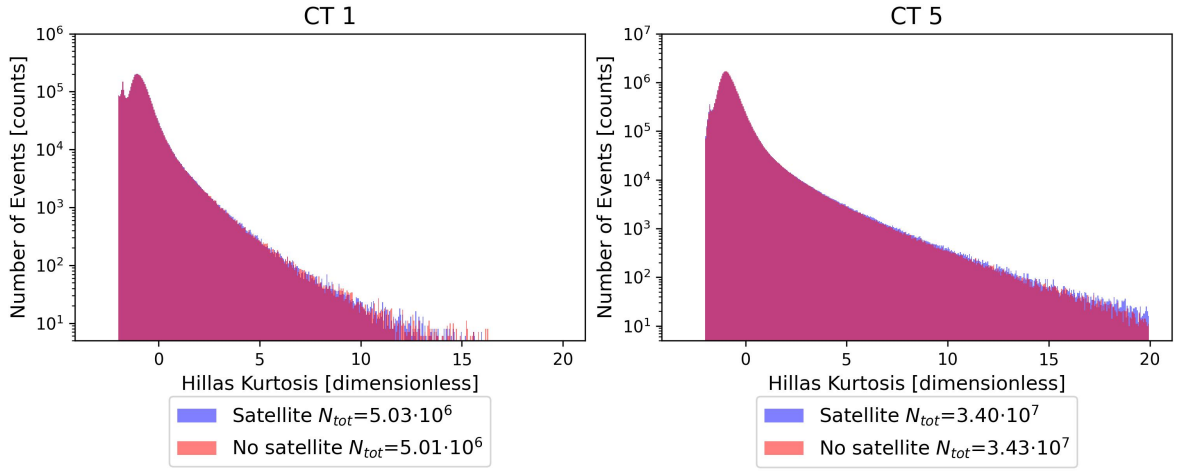

(a)

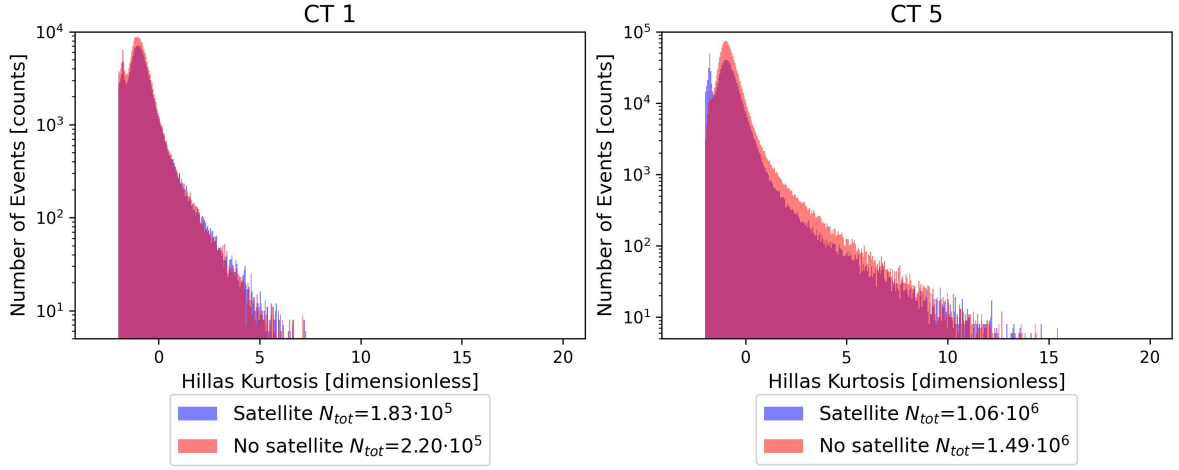

(b)

Figure 5.11: Hillas kurtosis for trails with an average brightness under (a) and over (b) 3000 MHz

proper γ-event, while the latter one is likely comprised solely of triggerings on the satellite.
The kurtosis distributions of dim satellite trails in Figure 5.11 (a) like the dim skewness ones show a marginal excess for larger values. The distribution of bright trails in Figure 5.11 (b) Bright trails create a very noticeable increase of events with close to minimal kurtosis in CT5 images. For Hillas kurtosis the minimum value of -2 occurs when the intensity distribution of the air shower image is perfectly flat.
From the dim distributions it can be concluded that the additional brightness in the pixels detecting the trail affects the event reconstruction in a negligibly small fraction of all events.

5.3 Trigger Rate

The system's trigger rate, and in particular its stability, are quality criteria for the HAP run selection, which is why they are discussed here. At this stage the trigger rate includes both γ- and non-γ events and is therefore different from the event rate presented in the preceding sections. While the γ-ray event rate during a bright satellite transit is considerably reduced, the total event rate is increasing. Figure 5.12 shows the telescopes' single trigger rates of the run number 175965, in which five satellite trails have been detected. Once more, CT1 is used here as a representative example for CT1-4. Two strong increases in the trigger rate can be seen that coincide with the two bright trails found in the run, with an additional small increase coinciding with a trail with an average brightness of $\sim$ 2070 MHz. This would indicate that the threshold at

which a satellite could be considered as "bright" might be adjusted in a future iteration of this analysis pipeline.

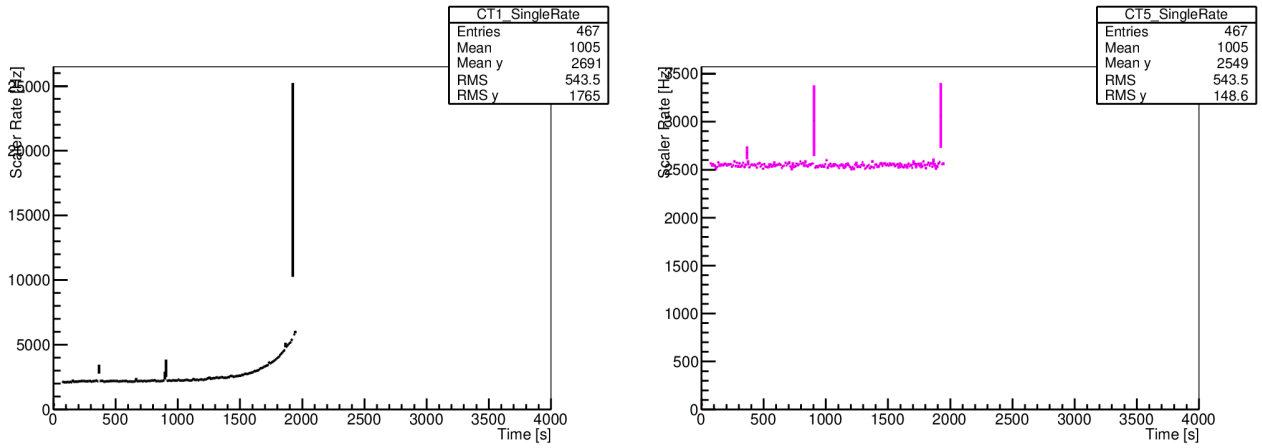

(a) CT1 Trigger Rate

(b) CT5 Trigger Rate

Figure 5.12: Trigger rates of CT1 and CT5 of run number 175965, Figures obtained from the H.E.S.S. websummary [56]. A noticeable increase in the trigger rate is detectable only for three of the five trails found.

One might assume that a decrease in the trigger rates of CT1-4 should be seen for the very bright trails, since the safety mechanism of those telescopes turns the affected pixels off. That however is not the case, as the last trail of the shown run, which was bright enough to trigger that feature, exemplifies. In fact, the increase seems to be even stronger than in CT5, although a more rigorous study of the trigger rates would be in order.

Chapter 6

Outlook and Conclusions

6.1 Predictions for CTA

Making predictions on the impact satellite trails will have on the taking of data with any of the three different CTA telescopes based on the results obtained in this work is difficult due to the varying telescope instrumentation. Even though it has been shown that the number of detectable trails scales linearly with the FOV [69], it is more appropriate to assume a scaling with the covered area for the impact on the very short Cherenkov events. Together with a continued increase of satellite trails as calculated by the linear model in section 4.3 the number of detected trails per hour in the year 2030 can be obtained.

Telescope Class	FoV Size [°]	Average Trails Per Hour [counts]	Observing Time Affected [%]
Small	9.0	15	5
Medium	8.0	12	4
Large	4.3	3	2

Table 6.1: Extrapolation of the number of detected satellites to 2030 for the three CTA telescope sizes, Table from [70]

The values for the three CTA telescope sizes shown in Table 6.1 assume, that the distribution of satellite altitudes and orbital inclinations are the same as for the investigated time period. As only trails above a certain threshold ($\sim 5 - 10\%$) will have a noticeable impact on the Hillas parameter distributions, the fraction of observing time noticeably affected by the satellites is even lower. Deep learning approaches for event classification however will likely be more affected than the Hillas based approach, as they take the entire image into consideration [74].
Predicting these fractions for other IACTs with different instrumentation, in particular with different sensitivities, is difficult, as the presented calculation is rather crude. Therefore it is recommended that an analysis similar to this work is done for the other IACTs currently in operation, verifying the findings presented here.

6.2 Meteorite trails

The approach of the satellite trail finding algorithm could in theory be extended to search for meteorite trails as well. So far the "Non-trail" trails are composed of both meteorite data and random, bright pixels. Also stemming from the way the current neighbourhood criterion is checked, the meteorite trails are too fast to be properly reconstructed. The example trail shown back in Figure 3.7 (a) was manually added together to from a cohesive trail. As a result a meteorite trail finder would need to be able to find out which "trails" are part of another one and

which ones are uncorrelated. Another problem would occur if a meteorite were to be detected during a camera flare, making it extremely difficult to separate one from the other. The suggested removal of camera flare time bins for future iterations of the satellite trail detection pipeline in that case would eliminate a large section of the meteorite trail as well.
The impact of meteorites on the overall taking of data has not been discussed in this work, as it can reasonably be assumed that the affected fraction of data is much lower than the one by satellites. For one the on-camera duration of any meteorite is much shorter than for even the fastest satellite trails. Furthermore by investigating the NSB data set prior to the application of the trail finder for a number of runs during the development of the trail finder it can be safely said that the majority of trails are produced by satellites.

6.3 Next Generation Satellites

The future v2.0 satellites have been tested by a launches of a similar model called v2.0 mini, with the first 21 being launched on the 27th of February 2023. They are larger than their predecessors, having two instead of one solar panel and additionally using additional radio frequencies in the E band [75].
With the finishing of Starlink's first generation satellite constellations approaching a short outlook at the planned second generation is warranted. The next generation Starlink v2.0 satellites are planned to orbit at an altitude of around 340 km, which will further improves on the latency. Consequently a single satellite covers a smaller area than the previous generation, leading to a need for a much larger satellite fleet to allow for continuous service.

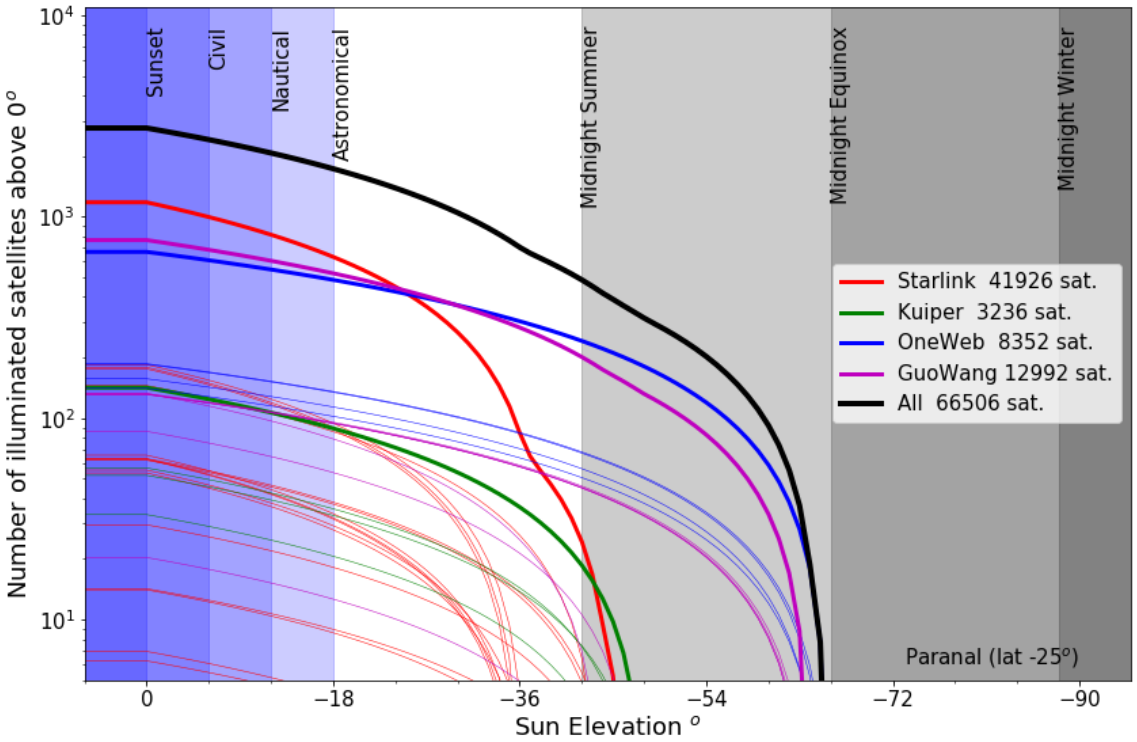

Figure 6.1: Prediction for the number satellites illuminated by the sun above the horizon as a function of the sun elevation for the full realisation of the planned mega constellations, Figure from [69]

However a lower satellite altitude means that the lowest sun elevation angle that allows for illumination by the sun is higher, reducing the affected fraction of the night. This is shown nicely in Figure 6.1, which displays the number of illuminated satellites above the horizon for the full

realization of the largest satellite mega-constellations as a function of the sun elevation angle, with the thin lines representing the different orbital shells within a constellation. The calculations made to arrive at these graphs were performed for the CTA south site latitude of -24.6°, hence very similar results for the H.E.S.S. site are to be expected as well. The actual minimum sun elevation angle is further reduced due to the typical maximum zenith angles of 60° during IACT measurements, which also reduces the number of potentially observable illuminated satellites by a factor of ~ 10 [69].
Since the new satellites will have a surface area more than eight times larger than the v1.x models [76], the angular size of a satellite will be increased. However this will not be as problematic for IACTs as for other ground based observations, since the angular size will remain well below the pixel resolution of any IACT telescope. The width of a satellite trail will still be primarily affected by the atmospheric scattering of the satellite's brightness.
To address that issue SpaceX is committed to implement several brightness mitigation strategies. Apart from coating any possible reflective surface with black paint an upgraded dielectric mirror film coating on the bottom side of the v2.0 satellites will be used to reduce the reflectiveness by a factor of 10 with respect to the first generation. Furthermore when crossing the night and day terminator line the solar arrays will be oriented away from earth [77].

6.4 Mitigation Strategy

There have been several strategies proposed to minimize the impact satellites have on astronomical observations. The easiest but most radical approach would be to remove all data during which a satellite was detected. However taking the predictions for 2030 this would result in a loss of data of up to 5%.
Another method would be to take satellite transits into account during the scheduling of observation targets. For those runs it should be possible to implement such a system, albeit at a large computational cost which only will increase with the number of LEO objects [69]. Unforeseen observations of transient objects, so called Target of Opportunity (ToO) observations however, still would be susceptible to satellite contamination.
A much simpler, but less thorough approach would be to avoid measurements close to sunset or sunrise in the corresponding directions to avoid the most illuminated satellites [69]. While an increase in detected satellite trails has been found, an implementation of any of the above mitigation strategies for H.E.S.S. or CTA in the near futuere seems likely not worth the effort, considering the low fraction of greatly affected observation time.

6.5 Summary

The utilization of satellites has brought significant revolutions in various aspects of modern life, ranging from communication and navigation to scientific research and environmental surveillance The widespread deployment of satellites has facilitated real-time data transmission and connected people across the globe like never before. With the advent of mega-constellations like Starlink or OneWeb a satellite-based internet connection has become feasible. This has the potential to bring about transformative changes for underserved and remote areas, enabling access to information, education and healthcare and providing economic opportunities to previously isolated communities.
With all the benefits satellites provide their effect on the night sky needs to be considered as well. Aside from the impact on astronomical observations the cultural implications, especially for peoples of developing nations, need to be taken into account [78]. To address all these concerns, the International Astronomical Union (IAU) Commission B7 – Protection of Existing

and Potential Observatory Sites advocates for the preservation of the night sky and a reduction in artificial glow.

In this work a new method has been presented to find satellite trails in the NSB data of H.E.S.S. This pipeline has been applied to the available CT5-FlashCam dataset until February 2023. An increase in the trail detection rate over that time period has been found. It has been verified that the most affected observations are the ones at the beginning and end of the night and those at large zenith angles.

The effect of satellites on the Hillas parameters has been quantified. Apart from the brightest satellites the impact on the event reconstruction parameters ranges from very small to non-existent. For bright trails, which make up less than 10% of all trails found, a reduction in the event rate can be seen, with additional false, low amplitude γ-like events occurring. Therefore standard scintific result using the *HAP* hybrid standard analysis cutoffs are likely not affected, while a tiny fraction of the observing time used in loose cut analyses is contaminated.

Estimations for the extent of the satellite contamion of IACT results, in particular for CTA have been made, however it is greatly advised that this experiment is repeated for other IACT observatories.

Bibliography

[1] Primož Rome. Every Satellite Orbiting Earth and Who Owns Them, January 2022.

[2] Union of Concerned Scientists. Satellite Database. https://www.ucsusa.org/resources/satellite-database. Accessed: 2023-03-28.

[3] Jonathan McDowell. Jonathan's Space Report, Enormous ('Mega') Satellite Constellations. https://planet4589.org/space/con/conlist.html. Accessed: 2023-03-28.

[4] A. Lawrence et al. The case for space environmentalism. *Nature Astronomy*, 6(4):428–435, apr 2022.

[5] BBC. ISS crew take to escape capsules in space junk alert. https://www.bbc.com/news/science-environment-17497766.

[6] Starlink website. https://www.starlink.com/technology.

[7] Gunter D. Krebs. MicroSat 2a, 2b (Tintin A, B), Retrieved May 19, 2023. https://space.skyrocket.de/doc_sdat/microsat-2.htm.

[8] Gunter D. Krebs. Starlink Block v1.0, Retrieved May 15, 2023. https://space.skyrocket.de/doc_sdat/starlink-v1-0.htm.

[9] Satellite visibility and DarkSat test, accessed on 17 of May, 2023. https://aas.org/sites/default/files/2020-06/SpaceX%20for%20SIA%20AAS%20Astronomy%20Webinar%205.26.20.pdf.

[10] Alexandra Witze. 'Unsustainable': how satellite swarms pose a rising threat to astronomy. https://www.nature.com/articles/d41586-022-01420-9, May 2022.

[11] Anthony Mallama and Jay Respler. Visual Brightness Characteristics of Starlink Generation 1 Satellites, 2022.

[12] Arndt Garrity, John; Husar. Digital Connectivity and Low Earth Orbit Satellite Constellations: Opportunities for Asia and the Pacific. https://think-asia.org/handle/11540/13626, 2021.

[13] Elon Musk. https://twitter.com/elonmusk/status/1127388838362378241.

[14] Official SpaceX Photos. https://www.flickr.com/photos/spacex/47926144123/.

[15] John Koetsier. Starlink Hits 250,000 Customers, Elon Musk Hints: SpaceX Booking Over $300 Million/Year. https://www.forbes.com/sites/johnkoetsier/2022/02/14/starlink-hits-250000-customers-elon-musk-hints-spacex-booking-over-300-millionyear/, February 2022.

[16] Victoria Girgis. Trails made by Starlink satellites. https://www.iau.org/news/announcements/detail/ann19035/, June 2019.

[17] Hainaut, Olivier R. and Williams, Andrew P. Impact of satellite constellations on astronomical observations with eso telescopes in the visible and infrared domains. *A&A*, 636:A121, 2020.

[18] Przemek Mróz et al. Impact of the SpaceX Starlink Satellites on the Zwicky Transient Facility Survey Observations. *The Astrophysical Journal Letters*, 924(2):L30, jan 2022.

[19] Stefano Gallozzi, Diego Paris, Marco Scardia, and David Dubois. Concerns about ground based astronomical observations: quantifying satellites' constellations damages, 2020.

[20] Cassandra Cavallaro. SKAO needs corrective measures from satellite 'mega-constellation' operators to minimise impact on its telescopes. https://www.skao.int/en/news/198/skao-needs-corrective-measures-satellite-mega-constellation-operators-minimise-impact-its, 2020.

[21] G. Pühlhofer et al. FlashCam: a fully-digital camera for the medium-sized telescopes of the Cherenkov Telescope Array, 2015.

[22] Malcolm S. Longair. *The acceleration of high energy particles*, page 561–582. Cambridge University Press, 3 edition, 2011.

[23] T Vieu, S Gabici, V Tatischeff, and S Ravikularaman. Cosmic ray production in superbubbles. *Monthly Notices of the Royal Astronomical Society*, 512(1):1275–1293, 02 2022.

[24] Bryan M. Gaensler and Patrick O. Slane. The Evolution and Structure of Pulsar Wind Nebulae. *Annual Review of Astronomy and Astrophysics*, 44(1):17–47, 2006.

[25] *Science with the Cherenkov Telescope Array*. WORLD SCIENTIFIC, Feb 2018.

[26] C. Megan Urry and Paolo Padovani. UNIFIED SCHEMES FOR RADIO-LOUD ACTIVE GALACTIC NUCLEI. *Publications of the Astronomical Society of the Pacific*, 107(715):803, Sep 1995.

[27] Chryssa Kouveliotou, Charles A. Meegan, Gerald J. Fishman, Narayana P. Bhat, Michael S. Briggs, Thomas M. Koshut, William S. Paciesas, and Geoffrey N. Pendleton. Identification of Two Classes of Gamma-Ray Bursts. , 413:L101, August 1993.

[28] Teraelectronvolt emission from the γ-ray burst GRB 190114C. *Nature*, 575(7783):455–458, nov 2019.

[29] Wikimedia Commons. File:H.E.S.S. II Telescope Array.jpg — Wikimedia Commons, the free media repository. https://commons.wikimedia.org/w/index.php?, 2020. [Online; accessed 24-August-2023].

[30] H.E.S.S. Collaboration. H.E.S.S. phase-I observations of the plane of the Milky Way, April 2018.

[31] High Energy Stereoscopic System. https://www.mpi-hd.mpg.de/HESS/pages/about/.

[32] Largest ever Cherenkov telescope sees first light. https://www.mpi-hd.mpg.de/hfm/HESS/pages/press/2012/HESS_II_first_light/.

[33] Konrad Bernlöhr Heinrich J. Völk. Imaging very high energy gamma-ray telescopes, 2009.

[34] Gianluca Giavitto et al. The upgrade of the H.E.S.S. cameras. *Nuclear Instruments and Methods in Physics Research Section A: Accelerators, Spectrometers, Detectors and Associated Equipment*, 876:35–38, 2017. The 9th international workshop on Ring Imaging Cherenkov Detectors (RICH2016).

[35] F. Werner et al. Performance verification of the FlashCam prototype camera for the Cherenkov Telescope Array. *Nuclear Instruments and Methods in Physics Research Section A: Accelerators, Spectrometers, Detectors and Associated Equipment*, 876:31–34, Dec 2017.

[36] Pühlhofer et al. Science verification of the new FlashCam-based camera in the 28 m telescope of H.E.S.S., August 2021.

[37] G.P. Diaz. Grünes Licht für den Bau des weltweit größten Gammastrahlen-Observatoriums. `https://www.desy.de/aktuelles/news_suche/index_ger.html?openDirectAnchor=1529`.

[38] Patrizia Caraveo. The golden age of high-energy gamma-ray astronomy: the Cherenkov Telescope Array in the multimessenger era. *La Rivista del Nuovo Cimento*, 43, 04 2020.

[39] The technology behind the next generation very-high energy gamma-ray detector. `https://www.cta-observatory.org/project/technology/`.

[40] (CTA-LST Project). Multiwavelength study of the galactic PeVatron candidate LHAASO J2108+5157. *A&A*, 673:A75, 2023.

[41] A. Donini et al. The Cherenkov Telescope Array Performance in Divergent Mode, 2019.

[42] S. Mollerach and E. Roulet. Progress in high-energy cosmic ray physics. *Progress in Particle and Nuclear Physics*, 98:85–118, jan 2018.

[43] J. Matthews. A Heitler model of extensive air showers. *Astroparticle Physics*, 22(5):387–397, 2005.

[44] Julian et al. Sitarek. Estimation of the height of the first interaction in gamma-ray showers observed by Cherenkov telescopes. *Astropart. Phys.*, 103:108–114, 2018.

[45] Stefan Funk. Ground- and Space-Based Gamma-Ray Astronomy. *Annual Review of Nuclear and Particle Science*, 65(1):245–277, 2015.

[46] Wikimedia Commons. File:Cherenkov2.svg — Wikimedia Commons, the free media repository. `https://commons.wikimedia.org/w/index.php?title=File:Cherenkov2.svg&oldid=555287211`, 2021. Online; accessed 17-May-2023.

[47] The H.E.S.S. Telescopes. `https://www.mpi-hd.mpg.de/HESS/pages/about/telescopes/#cherenkov`.

[48] U.F. Katz. Cherenkov light imaging in astroparticle physics. *Nuclear Instruments and Methods in Physics Research Section A: Accelerators, Spectrometers, Detectors and Associated Equipment*, 952:161654, feb 2020.

[49] Daniel et al. Guberman. Light-Trap: A SiPM Upgrade for Very High Energy Astronomy and Beyond. *Nuclear Instruments and Methods in Physics Research Section A: Accelerators, Spectrometers, Detectors and Associated Equipment*, 912, 09 2017.

[50] Samuel Spencer. Advanced analysis methods for Imaging Atmospheric Cherenkov Telescope data with SSTCAM and VERITAS [PhD thesis]. University of Oxford, 2021.

[51] C.R Benn and S.L Ellison. Brightness of the night sky over La Palma. *New Astronomy Reviews*, 42(6-8):503–507, nov 1998.

[52] S. Preuß, G. Hermann, W. Hofmann, and A. Kohnle. Study of the photon flux from the night sky at La Palma and Namibia, in the wavelength region relevant for imaging atmospheric Cherenkov telescopes. *Nuclear Instruments and Methods in Physics Research Section A: Accelerators, Spectrometers, Detectors and Associated Equipment*, 481(1-3):229–240, apr 2002.

[53] Kevin Krisciunas and Bradley E. Schaefer. A MODEL OF THE BRIGHTNESS OF MOONLIGHT. *Publications of the Astronomical Society of the Pacific*, 103(667):1033, sep 1991.

[54] Lenka et al. Tomankova. *Gain settings for the upgraded H.E.S.S. CT1-4 cameras under moonlight observations*, December 2022.

[55] F. Aharonian et al. Calibration of cameras of the H.E.S.S. detector. *Astroparticle Physics*, 22(2):109–125, 2004.

[56] Internal H.E.S.S. Web Summary.

[57] Vincent Marandon. HD NSB, internal H.E.S.S. confluence.

[58] S. Lombardi et al. Advanced stereoscopic gamma-ray shower analysis with the MAGIC telescopes, Sep 2011.

[59] I.H Bond, A.M Hillas, and S.M Bradbury. An island method of image cleaning for near threshold events from atmospheric Čerenkov telescopes. *Astroparticle Physics*, 20(3):311–321, 2003.

[60] R. D. Parsons and J. A. Hinton. A Monte Carlo template based analysis for air-Cherenkov arrays. *Astroparticle Physics*, 56:26–34, Apr 2014.

[61] Mathieu de Naurois. Analysis methods for Atmospheric Cerenkov Telescopes, 2006.

[62] S. Ohm, C. van Eldik, and K. Egberts. γ/hadron separation in very-high-energy γ-ray astronomy using a multivariate analysis method. *Astroparticle Physics*, 31(5):383–391, 2009.

[63] H.E.S.S. Collaboration. Detection of very-high-energy emission from the colliding wind binary with H.E.S.S. *A&A*, 635:A167, 2020.

[64] Maximilian Schandri. Investigation of Observation Quality Parameters for H.E.S.S.-II. `https://ecap.nat.fau.de/wp-content/uploads/2018/04/2018_Schandri_Master.pdf`.

[65] J. Hahn et al. Heidelberg Data Quality Selection, Feb 2013. HESS Internal report.

[66] HDF5 for Python. `https://docs.h5py.org/en/stable/`.

[67] H.E.S.S. Source of the Month. `https://www.mpi-hd.mpg.de/HESS/pages/home/som/2023/06/`.

[68] ATOM: A trailer, a trigger and a tug for H.E.S.S. `https://www.mpi-hd.mpg.de/HESS/pages/home/som/2020/05/`, May 2020. Accessed: 2023-06-11.

[69] C. G. Bassa, O. R. Hainaut, and D. Galadí -Enríquez. Analytical simulations of the effect of satellite constellations on optical and near-infrared observations. *Astronomy &amp Astrophysics*, 657:A75, jan 2022.

[70] Thomas Lang, Samuel T. Spencer, and Alison M. W. Mitchell. The Impact of Satellite Trails on H.E.S.S. Astronomical Observations, 2023.

[71] J. Hahn et al. Impact of aerosols and adverse atmospheric conditions on the data quality for spectral analysis of the H.E.S.S. telescopes. *Astroparticle Physics*, 54:25–32, feb 2014.

[72] M. Gaug, S. Fegan, A. M. W. Mitchell, M. C. Maccarone, T. Mineo, and A. Okumura. Using Muon Rings for the Calibration of the Cherenkov Telescope Array: A Systematic Review of the Method and Its Potential Accuracy. , 243(1):11, July 2019.

[73] H.E.S.S. Collaboration. H.E.S.S. Follow-up Observations of GRB 221009A. *The Astrophysical Journal Letters*, 946(1):L27, Mar 2023.

[74] I. Shilon et al. Application of deep learning methods to analysis of imaging atmospheric Cherenkov telescopes data. *Astroparticle Physics*, 105:44–53, feb 2019.

[75] Eric Ralph. SpaceX might launch first Starlink Gen2 satellites next week. `https://www.teslarati.com/spacex-first-starlink-gen2-satellite-launch-2022/`.

[76] Stephen Clark. SpaceX unveils first batch of larger upgraded Starlink satellites. `https://spaceflightnow.com/2023/02/26/spacex-unveils-first-batch-of-larger-upgraded-starlink-satellites/`, Feb 2023.

[77] SpaceX. BRIGHTNESS MITIGATION BEST PRACTICES FOR SATELLITE OPERATORS. `https://api.starlink.com/public-files/BrightnessMitigationBestPracticesSatelliteOperators.pdf`.

[78] H. et al. Dalgleish. How Can Astrotourism Serve the Sustainable Development Goals? The Namibian Example. In G. Schultz, J. Barnes, A. Fraknoi, and L. Shore, editors, *ASP2020: Embracing the Future: Astronomy Teaching and Public Engagement*, volume 531 of *Astronomical Society of the Pacific Conference Series*, page 17, November 2021.

Acknowledgements

Firstly I want to thank Dr. Alison Mitchell for introducing me to this interesting topic and providing me with the opportunity to gain insight into the H.E.S.S. collaboration. Furthermore I want to express my gratitude to Dr. Samuel Spencer, not only for addressing my technical inquiries, but also for providing various tools utilized in this work, as well as the invaluable critiques of my work. I also want to thank my family and friends who on many occasions had to patiently endure me trying to explain my work to them.
I am particularly grateful for my fiancée, Alina, whose love, understanding, and care have been unwavering during even the most challenging moments.

Statutory Declaration

I hereby declare that I wrote this thesis entirely by myself and did not use any sources or tools other than the ones referenced. This work has been supported by the Deutsche Forschungsgemeinschaft (DFG, German Research Foundation) – Project Number 452934793

Erlangen, 24.08.2023
Thomas Lang